Chemo-mechanical Modeling of Stress Corrosion Cracking of High Density Polyethylene in Bleach Solutions

A DISSERTATION
SUBMITTED TO THE FACULTY OF THE GRADUATE SCHOOL
OF THE UNIVERSITY OF MINNESOTA
BY

Anu Tripathi

IN PARTIAL FULFILLMENT OF THE REQUIREMENTS
FOR THE DEGREE OF
DOCTOR OF PHILOSOPHY

Jia-Liang Le, Advisor
Susan Mantell, Co-Advisor

October, 2020

Acknowledgements

I would like to express my gratitude to my advisors, Professors Jialiang Le and Susan Mantell, for providing their invaluable insight and guiding me through this journey in the past five years. I am also thankful to Prof. Mrinal Bhattacharya, Prof. Henryk Stolarski and Prof. Lauren Linermann for serving on my doctoral committee.

I gratefully acknowledge the sources that funded my doctoral research. I am thankful for the Department of Civil, Environmental, and Geo- Engineering for providing the Sommerfeld Fellowship for my first year and the Departmental Rescue Fellowship in the summer of 2019. I am also grateful to the National Science Foundation for funding the second, third, and fourth years of my studies.

I would also like to thank the group members who worked in Prof. Le's and Prof. Mantell's group during the last five years for their helpful discussions and support. I would especially like to thank Evan Cosgriff, Kelly Majewski, Andrew Hagen, and David McLernon without whom the very essential experimental part of the study could not have been successful. I would also like to thank Teng Man, Anna Gorgogianni, and Zhifeng Xu for their useful discussions, support, and friendship. I am also grateful to for his useful discussions and for his input to this project. Lastly, I would like to thank my family for all their love, support, and encouragement.

Dedication

To my family

Abstract

High density polyethylene (HDPE) is increasingly being used in infrastructure applications with a design service lifetime of several decades. In many cases, the member is exposed to a corrosive environment, such as in pipes carrying potable water, where the dissolved bleach selectively attacks the loosely packed amorphous phase of the polymer. The failure mode of HDPE transitions from a ductile to a brittle mode as the corrosion level increases. This leads to subcritical crack propagation that deteriorates the load capacity and long-term behavior of HDPE structure exposed to a chlorinated environment. In this study, we develop a coupled chemo-mechanical model to simulate stress corrosion cracking (SCC) of HDPE members in a bleach solution.

The mechanical response of the polymer is described by a constitutive model to considers the individual deformation and damage mechanisms of the amorphous and the crystalline phases. The model accounts for the intermolecular deformation and homogeneous void growth in the crystalline and amorphous phases, along with entangled network resistance and craze damage in the amorphous phase. The embrittlement due to corrosion is captured by relating the amorphous phase parameters to the polymer molecular weight which decreases with corrosion level. The proposed model is calibrated using uniaxial tensile tests at different deformation rates, crystallinities, and corrosion levels. The model is used to simulate the double-edge notched (DEN) tension specimens at different corrosion levels. The constitutive model can capture the rate dependent elasto-viscoplastic behavior of HDPE under the unexposed condition as well as the brittle failure behavior after exposure to a highly corrosive environment.

The decrease in the molecular weight of HDPE due to exposure to bleach environment is captured by a reduced order corrosion kinetics model. The selective

diffusion and chemical reaction of bleach into the amorphous phase leads to polymer chain scission that reduces the molecular weight. The corrosion kinetics model describes this diffusion-chemical reaction of bleach and expresses the extent of chain scission as a function of the bleach concentration.

The proposed material constitutive model and the diffusion-reaction model are combined in a single finite element (FE) code to investigate the SCC behavior of double edge notched HDPE specimens. The simulation yields the stress-life curves which qualitatively match the measured stress-life data of polymer pipes. The stress-life curve is shown to exhibit different regimes corresponding to distinct failure mechanisms, as indicated by the stress and strain distributions in the specimen. The simulations also provide the fracture kinetics under different environments, which can be used to predict the service life of an HDPE specimen with any geometry and applied load.

Contents

List of Tables

List of Figures

Chapter 1

Introduction

1.1 Motivation

Since the past few decades, there has been an ever increasing demand of plastics in many infrastructure applications owing to their low cost, ease of installation, and low weight-to-strength ratio. High density polyethylene (HDPE) is a popular low-cost thermoplastic, which has been extensively used for geo-membranes, pipes for drinking water and natural gas delivery, drainage, and cooling circuits in nuclear power plant. In many of these engineering applications, HDPE members are exposed to corrosive environments, such as potable water, where the chlorine disinfectants can diffuse into the amorphous phase and oxidize the polymer. These chemical reactions alter the material micro-structure, which leads to the properties degradation and subsequently change the failure mode. The combination of mechanical loading and chemical corrosion accelerates subcritical crack propagation. When a subcritical crack grows to a critical length, the load capacity of the specimen drops below the applied load level, and consequently the specimen experiences ultimate failure. Understanding this time-dependent failure behavior is essential for the

design of HDPE structures for long-term applications.

Owing to its critical role in structural design, subcritical crack growth has been studied through field studies, laboratory experiments, and numerical simulations. Field investigations of subcritical crack growth in HDPE pipes and geo-membranes revealed that, in a chlorinated environment, the HDPE exhibits a ductile failure mode at high stresses and a brittle failure mode at low stresses applied over a long duration [1, 2]. These field data were extracted from structure members that are subjected to creep loading over several decades, but the range of the loading parameters is quite limited. Laboratory experiments have been performed to investigate the long-term behavior of HDPE and other pipe materials through different accelerated testing techniques. Brown et al. [3] investigated the failure behavior of polyethylene under constant loading, and showed a transition from ductile to brittle failure modes when the applied load decreases. A similar transition in the failure mode has also been observed in static fatigue tests in corrosive environments [4, 5]. It was shown that, under chemical corrosion, the stress-life curve (the relation between the applied load and the structural lifetime) exhibits three distinct regimes: in the high stress regime the specimen shows a ductile mode with a gentle slope of the stress-life curve; in the intermediate stress regime the slope of the stress-life curve is steeper and the failure mode transitions from ductile to brittle; and in the low stress regime, the slope of the stress-life curve becomes steeper and the specimen undergoes brittle failure primarily governed by chemical corrosion. In addition to chemical corrosion, the effects of temperature, molecular weight, side-chain branching, and crystallinity on the crack growth behavior of polymers have been investigated [6, 7, 8, 9, 10, 11].

While experimental studies provided insight into the static fatigue behavior of HDPE in corrosive environments, most studies were performed on specimens with a simple geometry. Direct extrapolation of these experimental results to engineering design is not straightforward. This challenge can be addressed by computational models

of damage and failure. In the last decade, several constitutive models have been developed for semicrystalline polymers. Early works focused on phenomenological modeling, which does not explicitly account for the different phases of the material [12, 13, 14, 15]. Recently, more attention has been focused on developing mechanism-based constitutive models, which incorporate different deformation mechanisms of different phases of semicrystalline polymers. For instance, the constitutive response of amorphous phases was characterized by viscoplastic deformation coupled with void growth and craze damage [16, 17, 18, 19, 20], while the behavior of the crystalline phase was governed by viscoplasticity and void growth [21, 22, 23]. Motivated by this mechanism-based modeling approach, a morphology-based constitutive model was recently developed for HDPE [24]. The model is featured by an explicit relation between the constitutive properties and the molecular weight.

Besides constitutive modeling of HDPE, corrosion chemistry of HDPE is also required to understand the phenomenon of stress corrosion cracking (SCC). Several studies have investigated the corrosion mechanisms in HDPE exposed to chemicals, such as dissolved oxygen [25], bleach solution [26], and chlorine dioxide [27]. The corrosion process in HDPE starts with the diffusion of oxidizing agents into the amorphous phase [28]. These oxidizing agents dissociate into radicals in the polymer, which induce a series of radical oxidation reactions leading to the formation of several oxidation products along with chain scission and cross-linking of the polyethylene chains. These scission and cross-linking events change the underlying morphology of HDPE and therefore alter its mechanical behavior. In early studies, the rate constants in various chemical reactions were obtained by isolating each elementary reaction and experimentally measuring the concentration of the products and morphology, such as crystallinity and molecular weight [29, 30, 25]. With advances in modeling tools, the full set of chemical reactions (with as many as 14 reaction terms, and 4 diffusing species) can be analyzed by solving

a number of coupled differential equations, where the rate constants are obtained by fitting the model predictions to experimental data [31, 27, 26]. Studies have also accounted for the delay in the corrosion initiation due to antioxidant additives, which react with the oxidizing agents and prolong the polymer lifetime [32]. The reaction constants of the anti-oxidant reaction with the oxidizing agent were obtained based on the oxidation induction time [32, 27, 33]. However, these chemistry models are computationally inefficient for modeling of SCC of polymers.

To model the SCC behavior of HDPE, it has been proposed to use fracture kinetics to predict the lifetime of HDPE specimens, where the crack growth rate model is dependent on the corrosive environment [34, 35]. An empirical fracture kinetics modeling approach has limited applications. For example, the structure may experience more complex damage mechanisms as compared to propagation of a single crack. Therefore, it is necessary to develop a general model that combines the stress analysis with corrosion chemistry. To this end, Choi et al. proposed a crack layer model, in which the damage was considered to be concentrated in a process zone [36]. The model included a time decay of fracture energy to account for the static fatigue behavior of the material as well as the chemical degradation. The time-decay model is empirical in nature, and therefore it is only applicable to a given corrosive environment (e.g. a particular chlorine concentration, temperature). The model also does not consider the effect of the evolution of structural geometry due to crack propagation on the diffusion process of the chemical species. Ge et al. combined a viscoplastic material model and cohesive zone model to simulate the static fatigue of HDPE in bleach disinfected water [37]. In the model, the chemical corrosion was described by a diffusion-reaction model, and the fracture toughness was related to the concentration of diffused chemicals. Though the model captures the chemo-mechanical coupling, the model is limited to two-dimensional problems in which the path of crack propagation is known a priori. To enable a general analysis of stress corrosion cracking, a corrosion model must be integrated with the constitutive

model for calculating the stress and strain fields throughout the entire load history, until ultimate failure. Further the corrosion model must be simplified and a reduced order model of the reaction kinetics to reduce the computational cost.

1.2 Objectives

The goal of this study is to develop a chemo-mechanical numerical tools to investigate stress corrosion cracking of HDPE in bleach solution. The objectives of the study towards achieving this goal are:

1. To develop a morphology dependent damage constitutive model of HDPE to capture the ductile to brittle transition of the deformation and damage mechanisms with corrosion,
2. To develop a reduced order chemical-diffusion kinetics model to simulate the corrosion process and capture the rate of change of the HDPE morphology in a bleach solution,
3. To experimentally determine the dependence of constitutive parameters on the molecular weight,
4. To implement the proposed chemo-mechanical model in an FE model and use the numerical model to to simulate the different failure modes of HDPE under a range of stresses and in a chlorinated environment

1.3 Outline of the thesis

The organization of the thesis is as follows: chapter 2 describes the the interaction between a cohesive crack and capillary fluid to obtain the wetting zone in a crack exposed

to a capillary fluid; chapter 3 presents a morphology-based constitutive model of HDPE; chapter 4 presents the reduced corrosion kinetics model; chapter 5 discusses the numerical implementation of the present model and the SCC case study; and chapter 6 presents the main conclusions of the thesis.

Chapter 2

Modeling of cohesive fracture interacting with a stationary capillary fluid

2.1 Introduction

The presence of a capillary fluid within a cohesive crack is a phenomena that occurs in many engineering applications, such as concrete exposed to sea water [38], polymer pipes exposed to potable water [39] or nuclear waste water [40], and polymer geomembrane liners exposed to landfill contaminants [41]. The fracture behavior of these structures is dictated by the externally applied mechanical loading as well as by the fluid pressure exerted on the crack surface. The extent of fluid inside the crack is governed by the crack opening profile, which is governed by the overall loading on the crack. Therefore, the solution of this problem involves coupling between fracture behavior of the solid and capillary action of the fluid. One important engineering problem that is directly

related to this subject is stress corrosion cracking, in which the combination of stress and a corrosive fluid environment can lead to material failure through subcritical crack propagation. Stress corrosion cracking has been observed in many materials, such as concrete [38, 42], polymers [39, 40], and glass [43, 44]. At surfaces in contact with the corrosive fluid, the chemicals diffuse into the structural material and cause local degradation in material resistance, such as strength and fracture toughness [45, 42]. Since stress corrosion cracking typically occurs over a period of years, transient fluid flow into the crack can be neglected for the purpose of modeling. Previous studies of the fracture kinetics in stress corrosion cracking assume that the entire crack surface is wet by the fluid [46, 47]. However, few studies have provided the physical justification for this assumption.

Bui proposed a linear elastic fracture mechanics (LEFM) model for a Griffith crack partially filled with a capillary fluid [48]. The interaction between the fluid and the crack is described by the Young-Laplace equation, from which the overall equilibrium state can be solved by using a conventional LEFM approach. The model was used to determine the capillary stress intensity factor induced by the capillary fluid pressure, which provides a mechanical interpretation of Rehbinder's effect [49]. Bui's model was later extended to a wetting fluid inside a 3D penny shaped crack in an infinite elastic media [50]. It has transpired that LEFM is an idealized mathematical model since in reality there is always a nonlinear zone (e.g. plastic yielding, softening damage, etc.) formed at the crack tip. The LEFM framework provides an acceptable solution only if this nonlinear zone is considerably smaller than the overall specimen size.

In many engineering structures, the validity of LEFM is questionable because the nonlinear zone at the crack tip is not negligibly small compared to the characteristic structure size. Therefore, a nonlinear fracture mechanics model is needed. The simplest way to model this nonlinear zone is to use a cohesive zone model (CZM), which was pioneered independently by Barenblatt and Dugdale [51, 52, 53]. In this model, the

entire volume of the structure is treated as elastic, and the nonlinear behavior of the crack-tip region is smeared as a traction-separation type of boundary conditions at the crack face. The area under this traction-separation curve is equal to the material's fracture energy [54]. Since its development, extensive research has been performed to refine and extend the CZM for different fracture problems, such as fatigue crack growth [55, 56], and mixed-mode fracture [57, 58]. Recently the CZM has also been applied to study the crack propagation induced by hydraulic flow [59, 60, 61]. Despite the simplicity of the concept of CZM, closed-form solutions for structures of finite geometry are not common, and therefore, one often needs to rely on numerical solutions (e.g. finite element method). For engineering designs, it is desirable to develop an approximate model, which may lead to some closed-form solutions for a cohesive crack interacted with capillary fluid.

In this study, we adopt the concept of an equivalent LEFM model for studying the interaction between a cohesive crack and capillary fluid. The focus of the study is on the equilibrium state of a cohesive crack partially filled with the fluid, which is different from many other studies on fluid driven crack growth. The equivalent LEFM uses the principle of far-field equivalence to approximate the nonlinear zone at the crack tip by an extended LEFM crack [62, 63, 64, 65, 66]. In view of the success of CZM for various nonlinear fracture problems, the CZM model is used as a benchmark solution to establish this far-field equivalence. As a demonstration, the equivalent LEFM model is applied to determine the instantaneous failure pressure for polymer pipes, which reveals some key features of the fracture mechanics based approach. The model is further used to determine the wetting zone size for polymer pipes, which is an essential aspect of the numerical modeling of stress corrosion cracking.

2.2 Problem Statement and Model Formulation

Consider a two-dimensional (2D) setting in which a cohesive crack is partially filled with a capillary fluid. The crack is subjected to mode I loading (Fig. 2.1a), where the far-field stress is denoted by σ_∞. The fluid exerts a uniform pressure p on the crack surface. The behavior of the cohesive zone is described by a cohesive law, which can be expressed as

$$\sigma/f_t = g(w/w_u) \tag{2.1}$$

where σ = cohesive stress, f_t = material tensile strength, w = crack opening, and w_u = ultimate opening at which the cohesive stress reduces to zero. The shape of the cohesive law can be fully described by the dimensionless function $g(x)$. The area under the cohesive law is equal to the fracture energy G_f of the material [54], i.e. $f_t w_u \int_0^1 g(x)\mathrm{d}x = G_f$. Therefore, for a given shape of the cohesive law, the behavior of the cohesive crack can be determined by the material tensile strength f_t and the fracture energy G_f. The problem of interest is to determine the size of the wetting zone for given external loading σ_∞ and fluid pressure p such that the system is in an equilibrium state.

The fluid equilibrium can be described by the Young-Laplace equation [67, 68], which relates the difference of the capillary pressures between two stationary fluids to the curvature of the fluid interface. In 2D, this relationship reads

$$p = \gamma/R \tag{2.2}$$

where γ = surface tension, and R = radius of curvature of the interface. Fig. 2.1b presents a schematic fluid profile at the end of the wetting zone ($x = c$). The radius of curvature R can be calculated as

$$R = -\frac{w(c)}{2\cos\{\theta + \tan^{-1}[0.5w'(c)]\}} \tag{2.3}$$

where θ = contact angle ($\theta \geq \pi/2$ is required to form an equilibrated convex meniscus), $w(c)$ = crack opening displacement at $x = c$, and $w'(c) = \partial w(x)/\partial x|_{x=c}$ = spatial gradient of the crack opening displacement at $x = c$. Following [48], we neglect the term $w'(c)$ in Eq, 2.3 since the rotation angle (i.e. $\tan^{-1}[0.5w'(c)]$) is considerably smaller than the contact angle. This approximation becomes invalid when the fluid completely fills an LEFM crack. However, such a case is not encountered in this study, which focuses on cohesive fracture. Substitution of Eq. 2.3 into Eq. 2.2 yields [48]

$$w(c) = w_0 = -\frac{2\gamma \cos\theta}{p} \tag{2.4}$$

Eq. 2.4 gives the relationship between the crack opening displacement and the fluid pressure based on the equilibrium of the fluid interface. To describe the equilibrium of the solid, we first enforce the cohesive law

$$w_u g^{-1}[\sigma(x)/f_t] = C_{\sigma x}(a_c)\sigma_\infty + \int_0^c C_{x'x}(a_c) p \mathrm{d}x' - \int_{a_0}^{a_c} C_{x'x}(a_c)\sigma(x')\mathrm{d}x' \quad \text{for } x \in [a_0, a_c] \tag{2.5}$$

where $C_{\sigma x}(a_c)$ = compliance function describing the crack opening displacement at location x for a unit far-field external stress, $C_{x'x}$ = compliance function describing the crack opening displacement at location x when a pair of unit forces is applied at location x' of the crack surface, a_0 = length of the original traction-free crack, and a_c = total length of the cohesive crack including the traction-free crack.

Furthermore, the smooth closing condition requires that the total stress intensity factor at the tip of the cohesive crack equals zero [62], i.e.

$$\sigma_\infty k_\sigma(\alpha_c) + p k_c(\alpha_c) - \int_{\alpha_0}^{\alpha_c} \sigma(\xi) k_p(\xi, \alpha_c)\mathrm{d}\xi = 0 \tag{2.6}$$

where k_σ = dimensionless stress intensity factor for the far-field external stress (the stress intensity factor due to σ_∞ is expressed as $\sigma_\infty\sqrt{D}k_\sigma(\alpha_c)$), $k_p(\xi, \alpha_c)$ = dimensionless stress

intensity factor for the force pair applied at the crack surface with a relative coordinate $\xi = x/D$, and $k_c(\alpha_c) = \int_0^\chi k_p(\xi, \alpha_c)\mathrm{d}\xi$, $\alpha_0 = a_0/D$, $\alpha_c = a_c/D$, and $\chi = c/D$.

Finally, imposing the fluid equilibrium at the end of the wetting zone (i.e. Eq. 2.4) yields

$$C_{\sigma c}(a_c)\sigma_\infty + \int_0^c C_{xc}(a_c)p\mathrm{d}x - \int_{a_0}^{a_c} C_{xc}(a_c)\sigma(x)\mathrm{d}x = w_0 \tag{2.7}$$

Note that the compliance functions used in Eqs. 2.5-2.7 can be expressed by the dimensionless stress intensity factors as

$$C_{\sigma x}(a) = \frac{2D}{E'}\int_0^{a/D} k_\sigma(\alpha)k_p(\xi,\alpha)\mathrm{d}\alpha \tag{2.8}$$

$$C_{xx'}(a) = \frac{2}{E'}\int_0^{a/D} k_p(\xi',\alpha)k_p(\xi,\alpha)\mathrm{d}\alpha \tag{2.9}$$

where $E' = E$ for plane stress and $= E/(1-\nu^2)$ for plane strain, $E =$ Young's modulus, $\nu =$ Poisson ratio, and $\xi' = x'/D$.

The wetting zone size c, under a given external stress and fluid pressure can be determined using Eqs. 2.5-2.7. Alternatively, the external stress σ_∞ can be solved given a fluid pressure p and wetting zone size c. In general, Eqs. 2.5-2.7 must be solved numerically because the solution implicitly involves the determination of the cohesive zone size a_c. Based on the Vashy-Buckingham Π-theorem [69, 70, 71], the solution for a set of geometrically similar specimens can be written as

$$\frac{\sigma_\infty}{f_t} = \Pi_0\left(\pi_1, \pi_2, \pi_3, \pi_4, \pi_5, \pi_6\right) \tag{2.10}$$

where $\pi_1 = E'/f_t$, $\pi_2 = p/f_t$, $\pi_3 = c/a_0$, $\pi_4 = \alpha_0$, $\pi_5 = D/l_0$, and $\pi_6 = w_0/D$. The Irwin characteristic length $l_0 = EG_f/f_t^2$, is an essential length scale stemming from the cohesive law. For geometrically similar structures made of a given material, π_1 and π_4 are constants.

This problem can be greatly simplified if we consider the LEFM framework (i.e. assuming that the cohesive zone size is negligible compared to the structure size). With such a simplification, Eq. 2.7 directly yields the solution of σ_∞.

$$\sigma_\infty = \frac{w_0}{C_{\sigma c}(a_0)} - \frac{p}{C_{\sigma c}(a_0)} \int_0^c C_{xc}(a_0) \mathrm{d}x \tag{2.11}$$

For many specimen geometries, Eq. 2.11 can be calculated analytically since closed-form expressions of the stress intensity factors are available [72]. Indeed, Eq. 2.11 can be rewritten in a dimensionless form, which represents the limiting case of Eq. 2.10 by dropping the term π_5, i.e.

$$\frac{\sigma_\infty}{f_t} = \pi_1 \pi_6 I_1 - 2\pi_2 I_1 I_2 \tag{2.12}$$

$$\text{where:} \quad I_1 = 0.5 \left[\int_0^{\alpha_0} k_\sigma(\alpha) k_p(\chi, \alpha) \mathrm{d}\alpha \right]^{-1} \tag{2.13}$$

$$I_2 = \int_0^{\chi} \int_0^{\alpha_0} k_p(\xi, \alpha) k_p(\chi, \alpha) \mathrm{d}\alpha \mathrm{d}\xi \tag{2.14}$$

2.3 Equivalent Linear Elastic Fracture Mechanics Model

As shown in Section 2.2, the LEFM solution to this problem is far simpler compared to the CZM. It would be ideal to use the LEFM framework to obtain an approximate solution for the actual cohesive crack. Here we adopt an equivalent LEFM model, in which the fracture process zone (FPZ) is approximated by an extension of the LEFM crack [62, 63]. The concept of equivalent LEFM led to the development of the crack resistance curve (i.e. $R-$curve) for simulating the entire crack evolution process and the load-displacement curve of quasibrittle structures. In this study, the $R-$curve is not needed since the solution point corresponds to one particular equilibrium state.

The equivalent crack extension is directly proportional to the FPZ size, and

the FPZ size is further related to the length scale $l = [K_1(a_0)]^2/f_t^2$. Therefore, the equivalent crack extension Δa_e is expressed as

$$\Delta a_e = \frac{\kappa[K_1(a_0)]^2}{f_t^2} \tag{2.15}$$

where $\kappa =$ a constant to be determined, and $K_1(a_0)$ is the stress intensity factor for the original traction free crack, i.e.

$$K_1(a_0) = \sigma_\infty \sqrt{D} k_\sigma(\alpha_0) + p\sqrt{D} k_c(\alpha_0) \tag{2.16}$$

where σ_∞ is calculated by using Eq. 2.11. Within the framework of equivalent LEFM, the external applied stress can then be calculated as

$$\sigma_\infty = \frac{w_0}{C_{\sigma c}(a_0 + \Delta a_e)} - \frac{p}{C_{\sigma c}(a_0 + \Delta a_e)} \int_0^c C_{xc}(a_0 + \Delta a_e) \mathrm{d}x \tag{2.17}$$

If Δa_e is considerably smaller than a_0, the equivalent LEFM solution converges to the LEFM solution. This case corresponds to perfectly brittle behavior. On the other hand, if $\Delta a_e/a_0$ is not negligible, the FPZ will have a considerable size and the overall structural behavior is quasi-brittle, a transitional case between brittle and ductile behaviors. If Δa_e is comparable to the ligament length, the specimen could exhibit a ductile behavior. In view of this dependence of structural behavior on $\Delta a_e/a_0$, a brittleness number η can be defined

$$\eta = \frac{\Delta a_e}{a_0} = \frac{\zeta[K_1(a_0)]^2}{f_t^2 D} \tag{2.18}$$

where $\zeta = \kappa/\alpha_0$. Obviously a smaller value of η implies a more brittle behavior. In the present analysis, we consider that, at the equilibrium point, the original traction-free crack has not propagated under the given mechanical and fluid loading. This condition implies that $K_1(a_0) \leq K_{1c}$ ($K_{1c} =$ fracture toughness), and therefore $\eta \leq \zeta/\pi_5$.

Expanding Eq. 2.18, the parameter η can be expressed by the aforementioned group of dimensionless parameters as

$$\eta = \zeta(C_1\pi_2^2 + C_2\pi_1\pi_2\pi_6 + C_3\pi_1^2\pi_6^2) \tag{2.19}$$

where $C_1 = 4I_1^2I_2^2k_\sigma^2(\alpha_0) - 4I_2k_c(\alpha_0)k_\sigma(\alpha_0) + k_c^2(\alpha_0)$, $C_2 = 2I_1k_c(\alpha_0)k_\sigma(\alpha_0) - 4I_1^2I_2k_\sigma^2(\alpha_0)$, and $C_3 = I_1^2k_\sigma^2(\alpha_0)$. For geometrically similar specimens, C_1, C_2 and C_3 depend on π_3 only.

It is interesting to discuss the influence of the various model parameters on the brittleness number η. Let us assume that the surface tension and contact angle are constants. First consider the case where the relative wetting zone size π_3 is fixed. In this case, the far-field stress at equilibrium is fully determined by the fluid pressure p (Eq. 2.12). Under these conditions and in consideration of equations 2.4 and 2.19, η is expressed as a function of p as follows

$$\eta = \left(\frac{\zeta C_1}{f_t^2}\right)p^2 + \left(\frac{4\zeta C_3\pi_1^2\gamma^2\cos^2\theta}{D^2}\right)p^{-2} - \frac{2\zeta C_2\pi_1\gamma\cos\theta}{Df_t} \tag{2.20}$$

For a given specimen size, η will decrease if the tensile strength increases while the remaining material properties are constant. The increase of tensile strength leads to a decrease in the Irwin characteristic length l_0. Therefore, the specimen becomes more brittle. The same argument can be used to explain the decrease of η with a decreasing value of π_1.

Now consider that all the material properties and the relative wetting zone size are fixed. As the pressure increases, η first decreases and then increases, and the minimum value of η is given by $\eta_{min} = -2\zeta(Df_t)^{-1}(2\sqrt{C_1C_3} + C_2)\pi_1\gamma\cos\theta$. This non-monotonic behavior arises from the fluid and solid equilibrium conditions. When the fluid pressure p increases, the required crack opening displacement w_0 at the end of

wetting zone decreases, and therefore the external applied stress σ_∞ becomes smaller in order to attain w_0. The opposite trends of p and σ_∞ cause non-monotonic variations of the stress intensity factor and of the brittleness number.

A more practical situation occurs when the external stress is prescribed. As the fluid pressure increases, the critical opening displacement w_0 decreases, and the volume of fluid inside the crack increases. With increasing wetting zone size, the total loading on the FPZ must increase and therefore the brittleness number will increase, which indicates a more ductile behavior. Similarly, if the fluid pressure is constant and the external stress is increased, the crack opening will increase and, to maintain the same critical crack opening at the end of the wetting zone, the wetting zone size must increase. Consequently, the brittleness number will increase.

The LEFM framework provides a reasonable approximation when η is smaller than a threshold value η_{th}. For a given specimen geometry subjected to a fluid pressure p, this threshold value can be determined by limiting the difference between the external stresses predicted by the LEFM and the equivalent LEFM models. It is expected that, at this threshold, the extension of the equivalent LEFM Δa_e must be small. Therefore, we can apply the Taylor expansion to Eq. 2.17 to linearize the term $[C_{\sigma c}(a_0) + C'_{\sigma c}(a_0)\Delta a_e)]^{-1}$. By retaining only the first order term of Δa_e, we have

$$\sigma_\infty(a_0+\Delta a_e) = \sigma_\infty(a_0) - \left\{ \frac{w_0 C'_{\sigma c}(a_0)}{C^2_{\sigma c}(a_0)} - \frac{p}{C_{\sigma c}(a_0)} \left[\frac{C'_{\sigma c}(a_0)}{C_{\sigma c}(a_0)} \int_0^c C_{xc}(a_0)\mathrm{d}x - \int_0^c C'_{xc}(a_0)\mathrm{d}x \right] \right\} \Delta a_e \tag{2.21}$$

where $C'_{\sigma c}(a_0) = \mathrm{d}C_{\sigma c}(a)/\mathrm{d}a|_{a=a_0}$, and $C'_{xc}(a_0) = \mathrm{d}C_{xc}(a)/\mathrm{d}a|_{a=a_0}$.

With Eqs. 2.8 and 2.9, the relative difference between the equivalent LEFM

and LEFM solutions of the external stress is expressed as

$$\frac{\Delta\sigma_\infty}{\sigma_\infty(a_0)} = \sigma_\infty^{-1}(a_0)\left[\frac{E'w_0}{2D}I_3 - p(I_2I_3 - I_4)\right]\frac{\Delta a_e}{D} \tag{2.22}$$

$$\text{where:} \quad I_3 = \frac{k_\sigma(\alpha_0)k_p(\chi,\alpha_0)}{\left[\int_0^{\alpha_0} k_\sigma(\alpha')k_p(\chi,\alpha')\mathrm{d}\alpha'\right]^2} \tag{2.23}$$

$$I_4 = \frac{k_\sigma(\alpha_0)k_p(\chi,\alpha_0)}{\int_0^{\alpha_0} k_\sigma(\alpha')k_p(\chi,\alpha')\mathrm{d}\alpha'} \tag{2.24}$$

We consider LEFM valid when the relative difference of the calculated external stresses (Eq. 2.22) is than a threshold value ϵ (e.g. $\epsilon = 1\%$). Combining Eq. 2.22 with Eq. 2.12, the following expression for the threshold brittleness number is obtained

$$\eta_{th} = \frac{\epsilon(\pi_1\pi_6 I_1 - 2\pi_2 I_1 I_2)}{\pi_4\left[0.5\pi_1\pi_6 I_3 - \pi_2(I_2I_3 - I_4)\right]} \tag{2.25}$$

The threshold brittleness number is explicitly dependent on the material properties, capillary fluid pressure, and the wetting zone size. Eq. 2.25 predicts that, if the applied capillary pressure is considerably small compared to the material tensile strength, η_{th} depends only on the dimensionless parameters π_3 and π_4.

It should be emphasized that the present model is limited to the case in which the wetting zone does not enter the cohesive zone. If the fluid enters the FPZ, the fluid may fill the microcracks in the FPZ as well as pores (if there are any) in the material. It is still an open question whether a cohesive zone partially filled by fluid is sufficient for modeling the interaction between the fluid and FPZ. Modeling the effect of partially wetted FPZ on overall fracture behavior is beyond the scope of this study.

2.4 Numerical studies of Single-Edge Notched Specimens

2.4.1 Description of Analysis

The aforementioned analysis is applied to a single-edge notched specimen under plane strain conditions. The specimen geometry is shown in Fig. 2.1a. Two sets of material parameters are considered: 1) $G_f = 100$ N/m, $f_t = 3$ MPa, $E = 30$ GPa, and $\nu = 0.3$; and 2) $G_f = 1000$ N/m, $f_t = 30$ MPa, $E = 3$ GPa and $\nu = 0.3$. The first set of parameters corresponds to a typical concrete material while the second set corresponds to high density polyethylene (HDPE). These two materials are chosen due to their practical relevance to the present study [38, 39] as well as the large difference in their π_1 values. For both sets, we consider that the surface tension of water $\gamma = 0.072$ N/m and the contact angle $\theta = 105°$. For each material, a range of specimen sizes ($\pi_5 = 3, 9, 21,$ and 50) is analyzed. The initial relative crack length α_0 is 0.2 for all specimens. Two different sets of dimensionless fluid pressure values are considered for these two materials (for material 1, $\pi_2 = 2.5 \times 10^{-4}$ and 5×10^{-4}, and for material 2, $\pi_2 = 2.5 \times 10^{-5}$ and 5×10^{-5}).

Three model approaches are applied in the analysis: the CZM, the equivalent LEFM model, and the LEFM model. The CZM is solved by using the finite element simulation, in which we use a linear softening cohesive law, i.e. $g(x) = 1 - x \ \ (0 \leq x \leq 1)$ for Eq. 2.1. For each specimen, we calculate the relationship between the external stress σ_∞ and the relative wetting zone size c/a_0 for the given fluid pressure π_2. The solution of the CZM provides a benchmark solution to compare with the solutions of the equivalent LEFM and LEFM models. It should be emphasized that the main purpose of this numerical study is to understand the differences between these models. Therefore, low values of the fluid pressure are chosen purposely so that the critical crack opening w_0 is large enough to result in the formation of the FPZ of a non-negligible size for a

considerable range of the relative wetting zone sizes.

2.4.2 Results and Discussion

Figs. 2.2 and 2.3 present the solutions of these three methods for concrete and HDPE specimens, respectively. For each material, solutions are presented for the dimensionless applied external stress σ_∞/f_t as a function of the wetting zone size c/a_0. Four different specimen sizes are plotted a) $D/l_0 = 3$, b) $D/l_0 = 9$, c) $D/l_0 = 21$, and d) $D/l_0 = 50$. The solutions presented here correspond to the case where the original traction free crack has not propagated (i.e. $K_1(a_0) \leq K_{1c}$). For the CZM, this condition implies that the equilibrated far-field stress must occur in the pre-peak region. For all modeling conditions, σ_∞/f_t increases with increasing wet zone size. Regardless of the material or specimen size, the equivalent LEFM solution and the CZM solution show excellent agreement. For a given relative wetting zone size and fluid pressure, the external stress predicted by the CZM is lower than that predicted by the LEFM. The main feature of the CZM is that it allows gradual softening damage at the crack tip region (i.e. cohesive zone). Therefore, a specimen with a cohesive crack is more compliant than a specimen with an LEFM crack. A prescribed fluid pressure implies a fixed critical crack opening displacement w_0 at the end of the wetting zone. Consequently, the CZM will predict a lower external stress compared to the LEFM model. A detailed discussion follows in which predictions from the equivalent LEFM and LEFM models are compared with the CZM.

Equivalent LEFM model

For the equivalent LEFM model, we need to determine the proportionality constant κ (Eq. 2.15) by matching the equivalent LEFM solution with the CZM. This is essentially the far-field equivalence requirement of the equivalent LEFM model. As mentioned

earlier, κ is primarily governed by the cohesive stress profile [62], which can further be related to the brittleness of the specimen described by a dimensionless parameter $\beta = K_I^2(a_0)/f_t^2 D$ (similar to Eq. 2.18). Fig. 2.4 presents the relationship between κ and β for all the simulation cases. Regardless of the values of π_1, π_2, π_3, and π_5, all cases collapse reasonably onto a single curve.

Fig. 2.4 shows that κ asymptotically approaches constants for small and large values of β. In these two limiting cases, the cohesive stress profile converges to some particular forms. For large β values, the specimens exhibit a ductile behavior, which implies that the stress profile in the cohesive zone is approximately uniform [62]. Whereas for small β values, there is a softening stress profile in the cohesive zone, which is determined only by the cohesive law and the specimen geometry. The simulation also shows that the asymptotic κ value for small β is larger than that for large β. This result is expected because a more softening cohesive stress profile leads to a larger value of κ [62]. As shown in Fig. 2.4, the simulated relationship between κ and β can be approximated by the following equation

$$\kappa = \kappa_0 \exp[-(\beta/\beta_0)^m] + \kappa_1 \tag{2.26}$$

where $\kappa_0, \kappa_1, \beta_0, m =$ constants to be calibrated for given specimen geometry and cohesive law. For example, if an exponential or bi-linear cohesive law is used, these constants will change and further influence the brittleness number η. Though the geometry dependence of κ-curve is not investigated in this study, we may consider that, in the most general case, the κ-curve is a structural property. Once a κ-curve is calibrated for a given geometry and cohesive law, it can then be used for all different cases of π_1, π_2, π_3 and π_5. Therefore, in general, the equivalent LEFM model is much more efficient than the cohesive model.

LEFM model

LEFM offers the simplest solution to the problem and in many cases a closed form solution is possible. However, as discussed, LEFM is valid only if the brittleness number η is smaller than the threshold value η_{th} (Eq. 2.25). When determining η, the value of κ must be known. For the purpose of examining the validity of LEFM, we can use the maximum value of κ, i.e. $\kappa_m = \kappa_0 + \kappa_1$, which gives a conservative estimate of the equivalent crack length. κ_m can be determined by comparing the equivalent LEFM solution with the cohesive model for a small value of β. This conservative approach is much simpler than the equivalent LEFM solution, in which the entire κ curve is needed.

Figs. 2.5 and 2.6 present the relationship between η and c/a_0 for the aforementioned simulation results (Figs. 2.2 and 2.3) as well as the dependence of η_{th} and c/a_0. In this calculation, the value of η is computed by using k_m and a threshold ϵ value of 1% (Eq. 2.25). Since the present analysis uses small values of dimensionless fluid pressue ($\pi_2 = p/f_t$), Eq. 2.25 indicates that η_{th} is independent of the dimensionless stiffness ($\pi_1 = E'/f_t$). We observe that, for a given relative specimen size ($\pi_5 = D/l_0$), LEFM provides a reasonable approximation when the relative wetting zone size ($\pi_3 = c/a_0$) is small, as dictated by the condition $\eta \leq \eta_{th}$ (shaded regions in Figs. 2.5 and 2.6). This is because, for a small wetting zone and a given fluid pressure, the critical opening displacement w_0 is imposed at the location close to the crack mouth. As the wetting zone size increases, the same displacement must be imposed further inside the crack. Therefore, for a given fluid pressure ($\pi_2 = p/f_t$), a smaller wetting zone size is associated with a lower external stress. Consequently, the size of the FPZ is small. Under these conditions, the CZM is indistinguishable from the LEFM model. As the wetting zone size increases, the difference between these two models becomes more pronounced.

It is also found that, for a given specimen size and relative wetting zone size, an increase in fluid pressure p leads to a smaller difference between the LEFM solution

and the CZM, as indicated by the shaded regions in Figs. 2.5 and 2.6. To explain this observation, recall the previous analysis of the brittleness number (Eq. 2.20), in which we argued that the brittleness number η exhibits a non-monotonic behavior with respect to p if all other parameters are fixed: η initially decreases and then increases with an increasing value of p. The capillary pressure that corresponds to the minimum value of η is given by

$$p_0 = \left(\frac{C_3}{C_1}\right)^{1/4} \sqrt{-\frac{2\pi_1 \gamma \cos\theta f_t}{D}} \tag{2.27}$$

Consider the largest concrete specimen as a limiting case. The maximum value of p_0 is approximately 0.45 MPa, which is much larger than the applied fluid pressure p considered in this analysis. This finding confirms the aforementioned observation that a larger fluid pressure causes the specimen to behave in a more brittle manner.

Finally, Figs. 2.5 and 2.6 indicate that the difference between the CZM and LEFM diminishes as the specimen size increases (i.e. π_5 increases). This behavior is expected because, for large size specimens, the FPZ becomes negligible compared to the overall specimen size. Therefore, the specimen exhibits a brittle failure behavior, which implies that the CZM and LEFM essentially yield the same solution.

2.5 Application to Polymer Pipes

The foregoing analysis focused on the cases where the external applied stress is independent of the fluid pressure. However, in some engineering problems, these stresses are fully dependent on each other. One pertinent example is fluid induced cracking in pipes, which can be either instantaneous fracture or time-dependent subcritical crack growth under constant stress. Consider a polymer pipe containing a pre-existing crack at the inner surface (Fig. 2.7a). The hoop stress in the pipe is directly related to the fluid pressure inside the crack as $\sigma_\infty = pr/t$ (r = pipe radius, and t = pipe thickness). When

the radius of the pipe r is much larger than the pipe thickness t (typically, $r/t \approx 10$), the behavior of the inner crack can be approximated by analyzing a single-notched plane strain specimen (Fig. 2.7b). In this section, we discuss the application of the present model to the analysis of two pertinent failure modes: 1) instantaneous fracture, and 2) stress corrosion cracking.

2.5.1 Critical fluid pressure for instantaneous failure

One basic design criterion is that the fluid pressure should not cause any instantaneous failure of the pipe, which amounts to the determination of the critical fluid pressure p_c. For instantaneous fracture, we may ignore the time-dependent viscoplastic behavior of the bulk polymer material. Within the framework of equivalent LEFM, we consider that failure occurs as the stress intensity factor at the equivalent crack tip reaches the material fracture toughness, K_{1c}, i.e.

$$\frac{p_c r}{t}\sqrt{t}k_\sigma(\alpha_e) + p_c\sqrt{t}k_c(\alpha_e) = K_{1c} \tag{2.28}$$

where $\alpha_e = \alpha_0 + \Delta a_e/t$, in which Δa_e is calculated based on Eq. 2.15. In addition to Eq. 2.28, the displacement constraint at the end of the wetting zone must be imposed (Eq. 2.17) in which σ_∞ is replaced by $p_c R/t$. Solving Eqs. 2.28 and 2.17 together yields the critical fluid pressure as well as the wetting zone size. Note that the wetting zone will always be contained inside the traction-free crack.

To understand the influence of pipe size on the failure pressure, we consider a series of geometrically similar HDPE pipes ($r/t = 10$) of different thicknesses ($t = 5, 10, 20, 30, 40, 50, 100$ mm). The material parameters are the same as those for material 2 (see Section 2.4.1). The log-log plot in Fig. 2.8a shows the relationship between the critical fluid pressure normalized by the material tensile strength and the pipe thickness.

The critical fluid pressure decreases significantly with an increasing pipe thickness. In the log-log plot, this scaling asymptotically converges to a straight line with a slope of "$-1/2$" for large-size pipes, which matches the well-known scaling law predicted by LEFM [63]. For each thickness, the relative wetting zone size c/a_0 is found to be close to 1. At the large size limit, the equivalent crack length may be neglected (i.e. $\Delta a_e/t \to 0$), and therefore Eq. 2.28 directly yields

$$p_c = \frac{K_{1c}}{\sqrt{t}} \left[\frac{r}{t} k_\sigma(\alpha_0) + k_c(\alpha_0) \right]^{-1} \tag{2.29}$$

For intermediate pipe thicknesses, the scaling behavior of p_c predicted by the equivalent LEFM deviates significantly from the LEFM solution because the FPZ becomes non-negligible. This behavior is also demonstrated by comparing the brittleness number η with the corresponding LEFM threshold value η_{th} for each thickness (Fig. 2.8b). The η/η_{th} ratio is much larger than 1 as the pipe thickness decreases, which indicates that the pipe would behave in a quasibrittle manner.

It is worthwhile to compare the critical pressure predicted by equivalent LEFM with that calculated by the strength-based approach. For the strength-based approach, the critical pressure is $p_c^s = (1 - \alpha_0) f_t t/r$. The most evident difference between these two predictions is that the size effect is absent in the strength-based approach whereas the fracture mechanics approach predicts a strong size effect. Thus, for large pipes, the strength-based approach could significantly overestimate the critical pressure.

2.5.2 Wetting zone for stress corrosion cracking

Stress corrosion cracking is a typical time-dependent failure behavior for polymer pipes. The applied pressure is considerably lower than the critical pressure value for instantaneous failure. However, in stress corrosion cracking, the fluid enters the crack and

diffuses into the polymer material. This process leads to the degradation of material properties and further crack propagation. Such a chemomechanical failure mechanism eventually causes an unstable crack propagation in the material signifying pipe burst.

Since stress corrosion cracking takes place over a long period of time, the fluid can be approximately considered as quasi-stationary. The analysis of stress corrosion cracking typically requires modeling of diffusion of chemicals into the polymer, material degradation, and material fracture. In chemomechanical modeling, it is important to determine the wetting zone size, which provides the boundary condition for the diffusion of chemicals. In this analysis, we consider the pipe subjected to an allowable fluid pressure p_a, which is a fraction of the critical fluid pressure calculated in Section 2.5.1 (i.e. $p_a = \varphi p_c$). The factor φ accounts for 1) the factor of safety used for pipe design and 2) degradation of fracture properties due to corrosion. Here we assume $\varphi = 1/4$.

We use the equivalent LEFM model to calculate the relationship between the dimensionless fluid pressure p/f_t and relative wetting zone size c/a_0 for the aforementioned HPDE pipes, as shown in Fig. 2.9. For a given p/f_t value, the wetting zone size increases as the pipe thickness increases. The fluid pressure dictates the critical opening at the end of the wetting zone. As the pipe thickness increases, the crack mouth opening displacement also increases, and therefore the critical opening must occur at a location that is closer to the crack tip. Fig. 2.9 indicates that, for each pipe thickness, the crack can be considered to be fully wet under the allowable fluid pressure. Note that in this analysis we did not consider the time-dependent viscoplastic behavior of the bulk polymer material. However, the viscoplastic behavior of the bulk material would further increase the crack separation, and therefore the actual wetting zone would be larger than that predicted by the equivalent LEFM model.

Based on the aforementioned discussion, it can be concluded that we can consider a fully wet crack for modeling of the stress corrosion cracking of HDPE polymer

pipes. This approach simplifies the modeling process since it is unnecessary to calculate the wetting zone size during each step of crack propagation. Meanwhile, the present analysis indicates that, in addition to the viscoplastic bulk behavior of polymer materials, it is also necessary to consider the nonlinear fracture behavior of the FPZ, which can be modeled by either a simplified CZM or a detailed constitutive material model accounting for material damage.

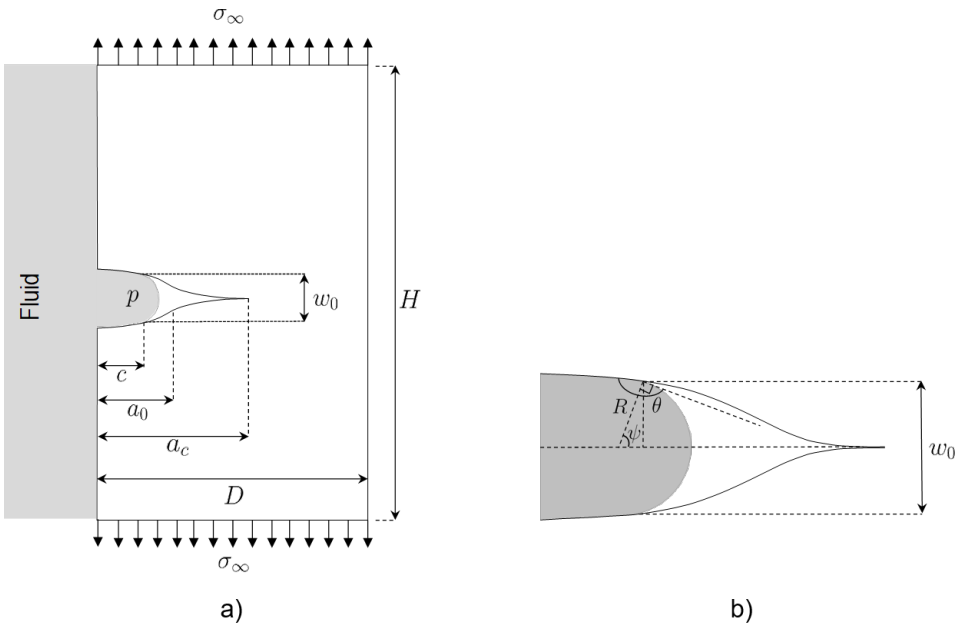

Figure 2.1: Schematic of a cohesive crack filled with stationary capillary fluid: a) specimen submerged in fluid, and b) capillary fluid inside a cohesive crack.

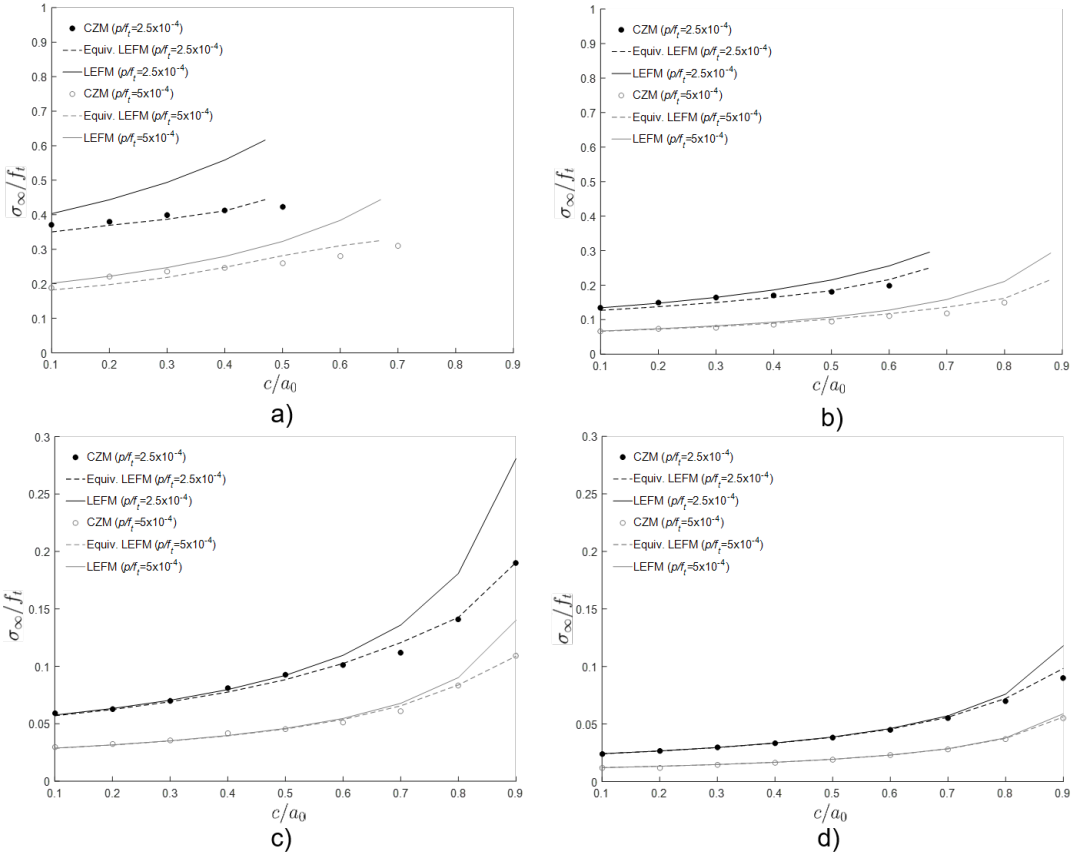

Figure 2.2: Relationships between the external applied stress σ_∞/f_t and the wetting zone size c/a_0 for concrete material for different D/l_0 values: a) $D/l_0 = 3$, b) $D/l_0 = 9$, c) $D/l_0 = 21$, and d) $D/l_0 = 50$.

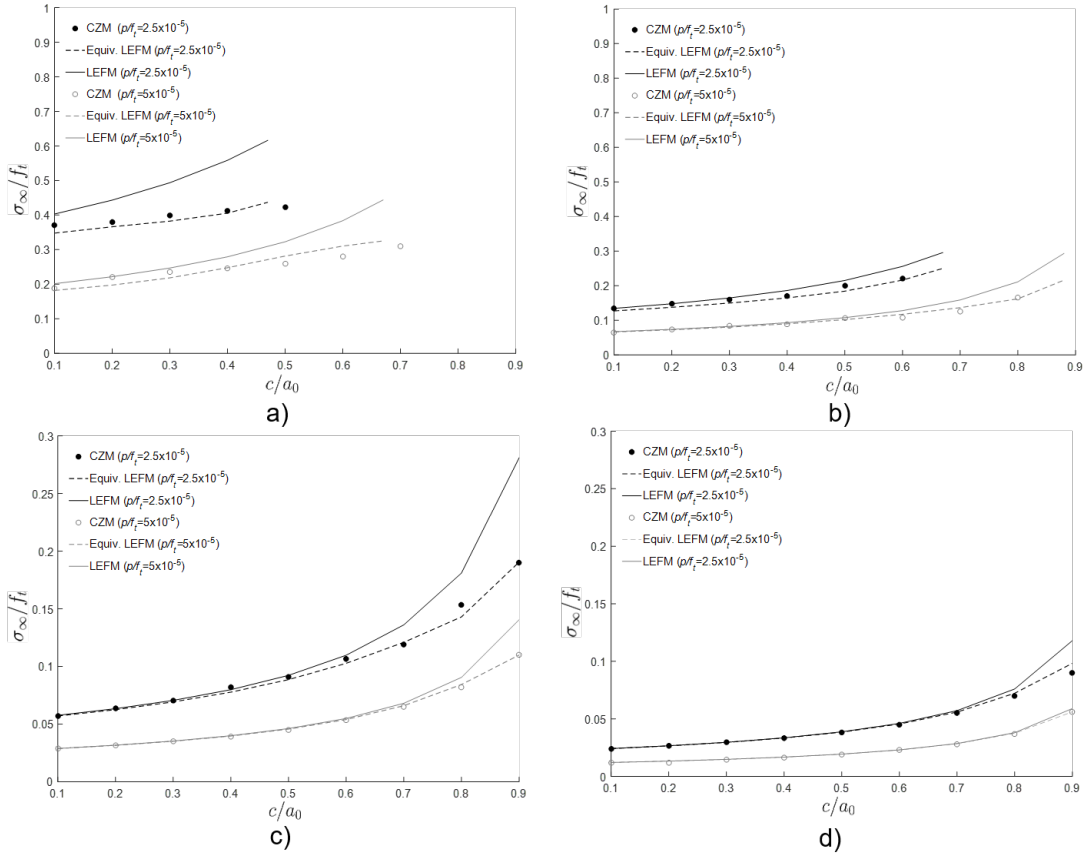

Figure 2.3: Relationships between the external applied stress σ_∞/f_t and the wetting zone size c/a_0 for HDPE material for different D/l_0 values: a) $D/l_0 = 3$, b) $D/l_0 = 9$, c) $D/l_0 = 21$, and d) $D/l_0 = 50$.

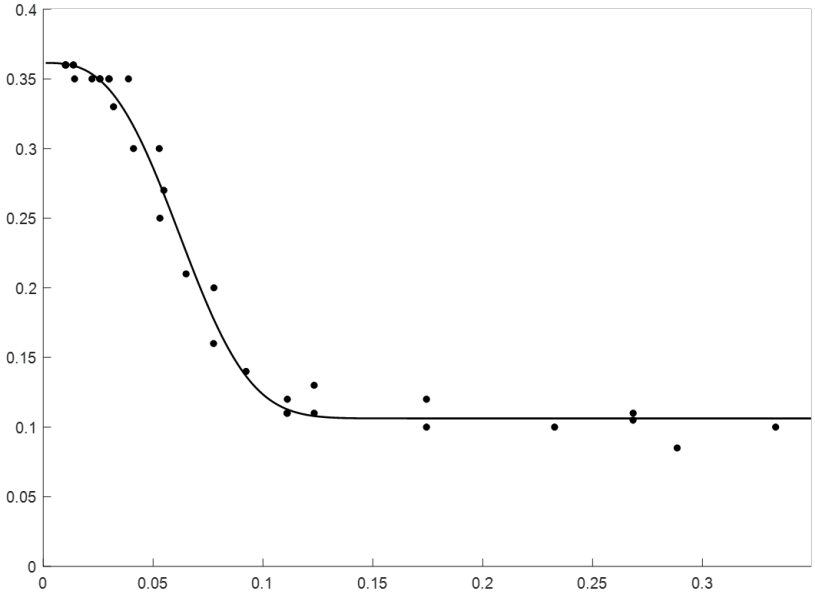

Figure 2.4: Relationship between constant κ and the dimensionless parameter β.

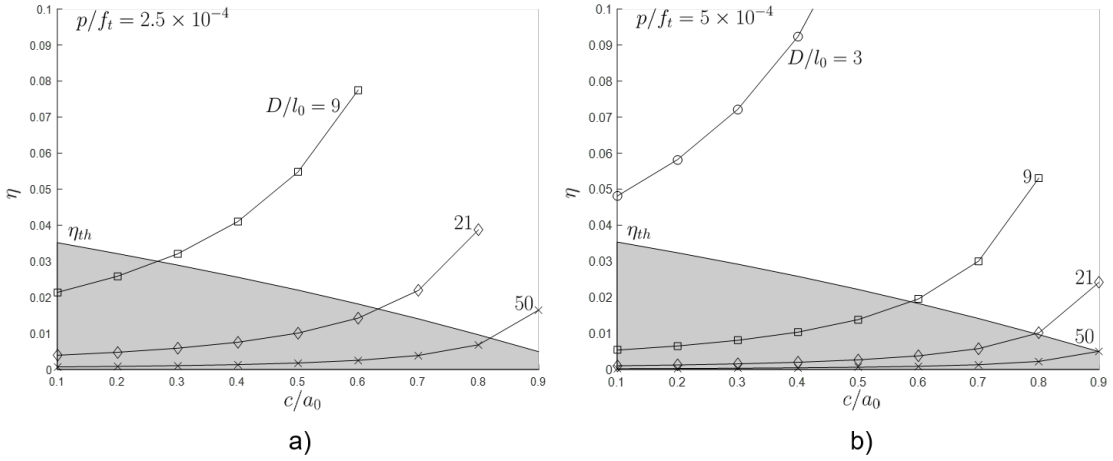

Figure 2.5: The validity of LEFM solution for various wetting zone size c/a_0 for concrete material under different fluid presssures: a) $p/f_t = 2.5 \times 10^{-5}$, and b) $p/f_t = 2.5 \times 10^{-5}$.

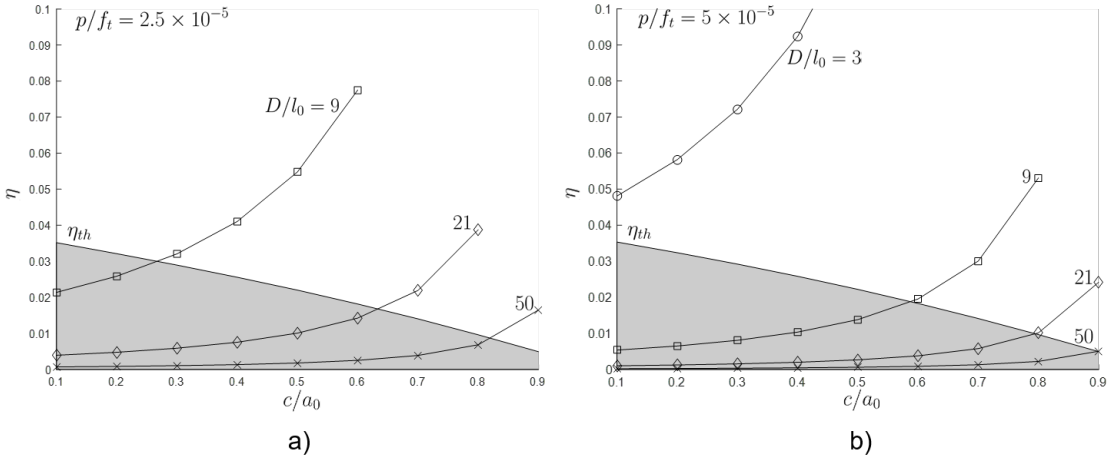

Figure 2.6: The validity of LEFM solution for various wetting zone size c/a_0 for HDPE material under different fluid presssures: a) $p/f_t = 2.5 \times 10^{-5}$, and b) $p/f_t = 2.5 \times 10^{-5}$.

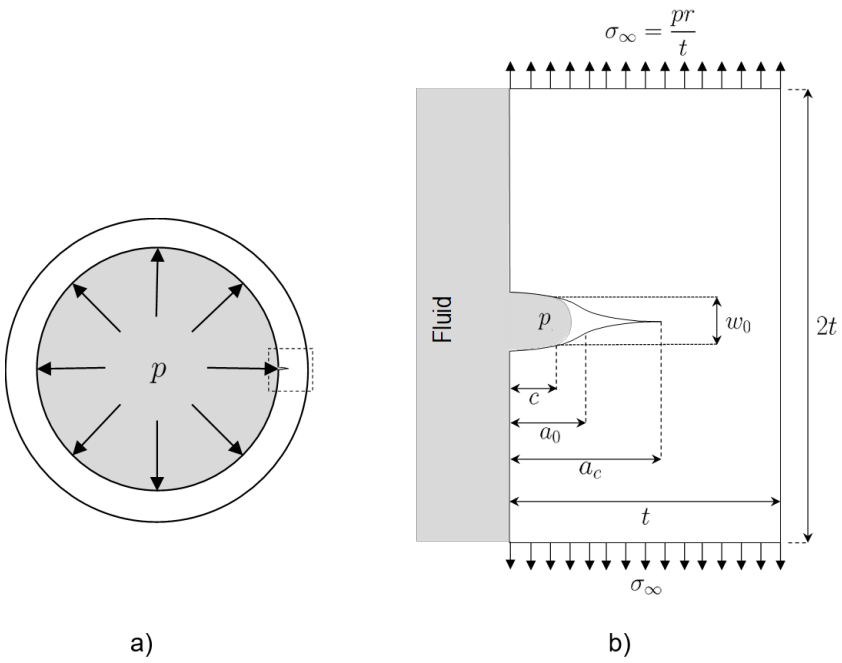

Figure 2.7: Simplified analysis of HDPE pipes with an inner crack: a) cross-section of pipe with an inner crack, and b) approximation by using a single edged notched specimen.

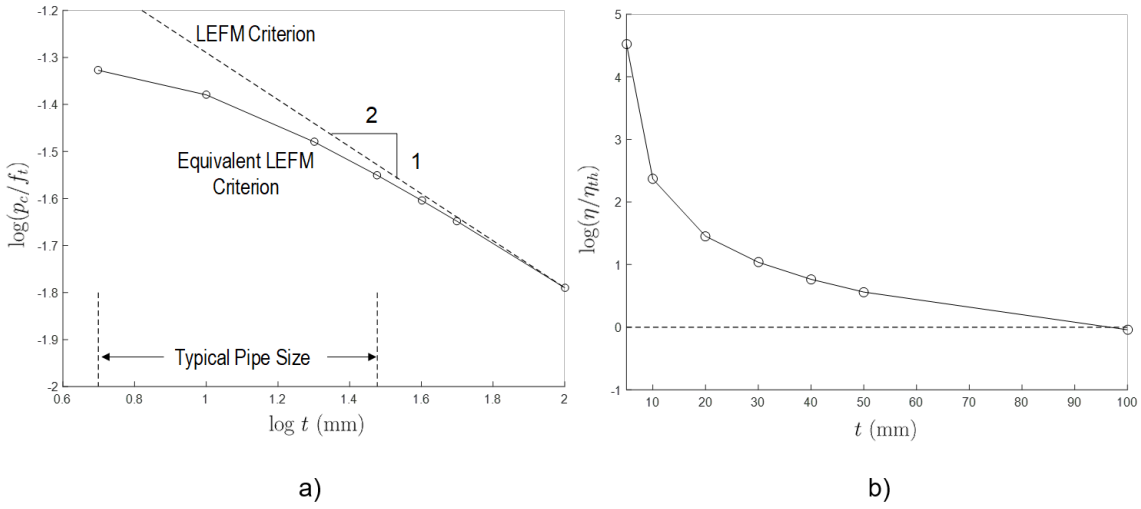

Figure 2.8: Analysis result of instantaneous failure of HDPE pipes: a) critical fluid pressures of HDPE pipes for different pipe thicknesses, and b) comparison between the brittleness number and the LEFM threshold brittleness number.

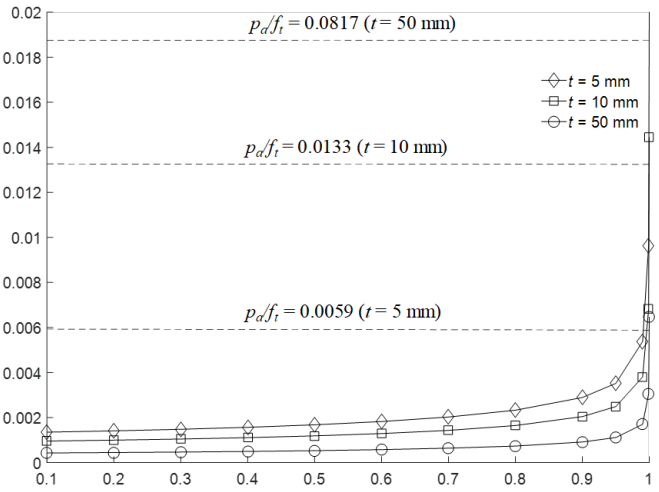

Figure 2.9: Relationship between the applied fluid pressure and the wetting zone size for HDPE pipes.

Chapter 3

Morphology based constitutive model of HDPE

3.1 Introduction

High density polyethylene (HDPE), a common type of semicrystalline polymer, is widely used in water supply pipes. These pipe systems are designed for an ideal service lifetime of several decades. However, exposure of HDPE to chlorine over an extended period of time leads to chemical corrosion, which influences the morphology of HDPE, such as the crystallinity and the molecular weight. As a direct consequence, the material fails in a brittle manner manifested by sub-critical crack growth, which significantly reduces the structural lifetime. Therefore, the design of HDPE structures for long-term applications must be anchored by understanding how a corrosive environment influences the failure mechanisms. To investigate the long-term behavior of HDPE, accelerated experimental techniques, such as high temperature and high UV exposure have been proposed [7, 1, 2]. With advances in computational mechanics, direct numerical modeling has become an

attractive tool for lifetime prediction of HDPE [36, 34, 37]. For computational modeling, an important research area has been development of constitutive models to describe the mechanical response of the material.

Over the past several decades, extensive effort has been devoted to developing physically-motivated constitutive models for semicrystalline polymers. Many attempts relied on phenomenological approaches, in which the amorphous and crystalline phases were lumped together without considering the differences between their deformation mechanisms [12, 13, 14, 15, 73]. Recognizing that the polymer morphology is comprised of long macromolecules (chains) that may be ordered or entangled, researchers have proposed that the intermolecular and network resistances contribute to the deformation behavior. Intermolecular resistance is the resistance to deformation from adjacent polymer chains, while network resistance is the resistance to stretching of the chain entanglement network. Using this approach, the elasto-viscoplastic constitutive behavior of the amorphous phase was attributed to both intermolecular and network resistances, which were modeled by a combination of elastic springs and viscous dashpots [74, 75, 76, 19, 16]. The crystalline phase deformation behavior is captured by an intermolecular resistance model [21, 22, 23].

At large deformations, the elasto-viscoplastic response is accompanied by damage growth, which often leads to plastic volumetric expansion [77]. One phenomenological approach to model this damage mechanism is continuum damage mechanics [77], in which a state variable is used to describe the evolution of irreversible macroscopic damage. Another commonly used approach to model the ductile failure of the polymer is the homogeneous void growth model [78, 79, 80, 81, 82], which uses a yield potential function to describe void nucleation and growth. Most of these models were developed by modifying the Gurson-Tvergaard-Needleman (GTN) model [83].

In addition to the ductile failure mode, brittle failure of semicrystalline polymers has also been studied, which results from the crazing mechanism [84, 85, 86]. At low stresses, the material experiences homogeneous deformation. When the applied stress is sufficiently high, micro-voids localize into regions with well defined planar surfaces, leading to craze initiation. Crazes form as an array of voids separated by many fine fibrils stretched along the principal tensile stress direction. The craze damage process has been investigated using advanced experimental tools such as transmission electron microscopy and small angle X-ray scattering [87, 88, 89, 86, 84]. These techniques elucidated the mechanism of craze widening through chain drawing from the bulk material. The growth and breakdown of crazes eventually lead to the formation and propagation of a traction free crack. Motivated by the experimental finding of the crazing mechanism, mechanical models to capture this brittle failure were also developed based on concepts of linear elastic fracture mechanics [90], cohesive zone model [17, 18], and a smeared damage model [20]. These models were shown to be capable of capturing the competition between shear yielding and craze damage in glassy polymers.

Despite the aforementioned extensive efforts on constitutive modeling of semicrystalline polymers, few studies have developed a comprehensive constitutive model that accounts for deformation and failure mechanisms as corrosion proceeds. This study is motivated by the need of formulating such a constitutive model for future computational simulations of long-term behavior of HDPE exposed to chlorinated environment. The chapter is planned as follows: Section 3.2 presents the framework of the constitutive model and its relation to the underlying deformation mechanism, Section 3.3 discusses the experimental investigation, which involves uniaxial tensile tests on HDPE specimens at different corrosion levels, and Section 3.4 presents the model calibration and validation based on the present experiments.

3.2 Constitutive Modeling Framework

Semicrystalline polymers consist of polymeric chains regularly arranged in crystalline lamellae interconnected by amorphous tie chains. The mechanical behavior is strongly affected by the material morphology, such as the molecular chain structure, the degree of polymerization, and the crystallinity. The microstructure of HDPE is featured by unbranched linear chains of carbon-carbon single bonds. The length of these chains is quantified by the molecular weight. The short unbranched chains can easily arrange themselves in a regular pattern to form the crystalline lamellae. On the other hand, it is difficult for long-chain polymers to fully crystallize. The crystalline lamellae are interconnected by randomly coiled and entangled tie chain molecules (Fig. 3.1) that make up the amorphous phase of the HDPE. The longer molecular chains tend to be present in the amorphous phase [28].

When HDPE is exposed to chlorinated environment, chlorine selectively diffuses into the amorphous phase with loosely packed tie chains instead of the densely packed crystalline phase. Chlorine reacts with the tie chain molecules and breaks the tie chains into shorter chains, a process referred to as chain scission. Chain scission not only reduces the average molecular weight, but also causes considerable change in the entanglement network of the HDPE. The change in the entanglement network promotes craze damage and deteriorates the load carrying capacity of the material. Consequently, the failure mode transitions from ductile to brittle, as the corrosion level increases. Meanwhile, the short segments of tie molecules formed as a result of chain scission tend to crystallize, which is known as chemi-crystallization. However, these newly formed lamellae are not interconnected and do not contribute to the overall load-carrying capacity. Therefore, the overall load resistance of the polymer deteriorates.

Based on the foregoing discussion, it is clear that, to capture the various governing failure mechanisms of the material as corrosion proceeds, one must model the

constitutive behaviors of the crystalline and the amorphous phases separately. In this study, we consider a parallel coupling of the crystalline and the amorphous phases (Fig. 3.2) [16] and therefore we have $\mathbf{F}_c = \mathbf{F}_a$, where $\mathbf{F}_c$ and $\mathbf{F}_a$ denote the deformation gradients of the crystalline and amorphous phases, respectively.

Based on Fig. 3.2, the total stress is given by the weighted sum of the stresses in the crystalline and amorphous phases. The weights are determined by the crystallinity, which is defined as the volume fraction of the crystalline phase. The primary mechanism of chemical corrosion of HDPE is scission of long tie chain molecules, and the resulting short molecular segments undergo chemi-crystallization. Since the lamellae formed from chemi-crystallization do not have load-carrying capacity, the resistance of the crystalline phase must be calculated based on the initial crystallinity. The total stress in HDPE can be expressed by:

$$\mathbf{T} = z_0\mathbf{T}_c + (1 - z)\mathbf{T}_a \tag{3.1}$$

where z is the crystallinity at the current state, z_0 is the initial crystallinity, $\mathbf{T}$ is the Cauchy stress in the polymer, $\mathbf{T}_c$ is the Cauchy stress in the crystalline phase, and $\mathbf{T}_a$ is the Cauchy stress in the amorphous phase. The following sections will discuss the constitutive relations for the crystalline and amorphous phases.

3.2.1 Crystalline resistance

In the crystalline phase, the molecules have a regular arrangement without any entanglements (Fig. 3.1). Therefore, the resistance to deformation is provided only through the intermolecular mechanism. Under external loading the molecules are displaced from their equilibrium positions. When the loading is sufficiently high, the deformation of the crystalline phase exhibits a plastic flow through crystal rotation and slip along the preferred directions.

To formulate the constitutive relation of the crystalline phase, we decompose the deformation gradient into the elastic and plastic components, i.e. $\mathbf{F}_c = \mathbf{F}_c^e \mathbf{F}_c^p$ [91, 92]. Therefore, the velocity gradient can be calculated as

$$\mathbf{L}_c = \dot{\mathbf{F}}_c^e \mathbf{F}_c^{e^{-1}} + \mathbf{F}_c^e \dot{\mathbf{F}}_c^p \mathbf{F}_c^{p^{-1}} \mathbf{F}_c^{e^{-1}} \tag{3.2}$$

Eq. 3.2 suggests that the velocity gradient $\mathbf{L}_c$ can be separated into the elastic and plastic parts, i.e. $\mathbf{L}_c^e = \dot{\mathbf{F}}_c^e \mathbf{F}_c^{e^{-1}}$, and $\mathbf{L}_c^p = \mathbf{F}_c^e \dot{\mathbf{F}}_c^p \mathbf{F}_c^{p^{-1}} \mathbf{F}_c^{e^{-1}}$. The plastic part of the velocity gradient can further be decomposed into the rate of deformation and spin tensors:

$$\mathbf{L}_c^p = \mathbf{D}_c^p + \mathbf{W}_c^p \tag{3.3}$$

Following [92], we conveniently choose $\mathbf{W}_c^p = 0$ here since there is no clear constitutive constraint on the plastic spin.

The intermolecular stress in the crystalline phase can be directly calculated from the elastic deformation [22, 23]:

$$\mathbf{T}_c = \frac{\mathbf{C}_c^e \ln(\mathbf{V}_c^e)}{J_c} \tag{3.4}$$

where $\mathbf{C}_c^e$ is the fourth order stiffness tensor with components $C_{c,ijkl}^e = \lambda_c \delta_{ij} \delta_{kl} + \mu \delta_{ik} \delta_{jl}$, where $\lambda_c = E_c \nu_c / (1 + \nu_c)(1 - 2\nu_c)$ and $\mu_c = E_c / 2(1 + \nu_c)$ are the Lames constants, E_c is the elastic modulus, ν_c is the Poisson's ratio, $\mathbf{V}_c^e = \left(\mathbf{F}_c^e \mathbf{F}_c^{eT}\right)^{1/2}$ = left elastic stretch tensor, and J_c = volume change of the crystalline phase. J_c can be calculated as $J_c = (1 - f_c)\det(\mathbf{F}_c^e)$, where f_c is the void volume fraction in the crystalline phase.

During the plastic flow of the crystalline phase, the crystal breakdown eventually causes void growth and coalescence. The void nucleation and growth occur homogeneously in the crystalline phase, irrespective of the molecular weight or the crystallinity, which results in a ductile failure mode. One of the most widely used models for void growth and coalescence is the Gurson-Tvergaard-Needleman (GTN) model [93, 83], which has recently been applied to semicrystalline polymers [82, 94]. The GTN yield function is given by [83]

$$\Phi_c = \frac{\sigma_{eq}^2}{\sigma_{fc}^2} + 2q_1 f_c^* \cosh\left(\frac{q_2 \bar{\sigma}_m}{2\sigma_{fc}}\right) - (q_1 f_c^*)^2 - 1 \tag{3.5}$$

where $\bar{\sigma}_m = (1 - f_c)\mathrm{tr}(\mathbf{T}_c)$, $\sigma_{eq} = (1 - f_c)\sqrt{3\mathbf{T}_c' : \mathbf{T}_c'/2}$ ($\mathbf{T}_c'$ denotes the deviatoric Cauchy stress in the crystalline phase), σ_{fc} is the tensile flow stress in the crystalline phase, f_c^* = effective void ratio, and q_1, q_2 = constants. The plastic flow is governed by the yield criterion $\Phi_c = 0$, from which the flow stress σ_{fc} can be determined. The effective void ratio f_c^* is defined as [83]

$$f_c^* = f_c \quad \text{if} \quad f_c \le f_{cc} \tag{3.6}$$

$$f_c^* = f_{cc} + \frac{f_{cu} - f_{cc}}{f_{cf} - f_{cc}}(f_c - f_{cc}) \quad \text{if} \quad f_c > f_{cc} \tag{3.7}$$

where $f_{cu} = 1/q_1$ is the theoretical ultimate value of f_c^* at final failure [83, 94], f_{cf} is the actual void volume fraction at the failure, and f_{cc} is the critical void volume fraction at which the accelerated void growth occurs due to void coalescence [83, 94]. Note that f_c^* takes into account the effect of void coalescence on the flow potential Φ_c whereas f_c is the actual void ratio in the material.

The rate of plastic deformation can be calculated based on the potential function [95]:

$$\mathbf{D}_c^p = \frac{(1 - f_c)\dot{\gamma}_c \tau_c}{\mathbf{T}_c : \frac{\partial \Phi_c}{\partial \mathbf{T}_c}} \frac{\partial \Phi_c}{\partial \mathbf{T}_c} \tag{3.8}$$

where $\tau_c = \sqrt{\mathbf{T}'_c : \mathbf{T}'_c/2}$, and $\dot{\gamma}_c$ = viscoplastic shear strain rate. Eq. 3.8 implies an associated flow rule. By taking $f_c = 0$, Eq. 3.8 becomes $\mathbf{D}^p_c = \dot{\gamma}_c \mathbf{T}'_c/\sqrt{2}\tau_c$, which recovers a previously proposed formulation without considering the void growth [16]. The viscoplastic shear strain rate $\dot{\gamma}_c$ is follows an Arrhenius type expression [96, 16, 95].

$$\dot{\gamma}_c = \gamma_{c0} \exp\left(-\frac{1 - \tau_c/s_c}{k_b T/\Delta G_c}\right) \tag{3.9}$$

where γ_{c0} = a constant, k_b = Boltzmann constant, T = absolute temperature, and ΔG_c = energy barrier governing the flow. The shear resistance s_c is given by $s_c = [s_{c0} + \alpha_c \mathrm{tr}(\mathbf{T}_c)]$, where s_{c0} = shear resistance under zero hydrostatic stress, and α_c = pressure coefficient.

The formulation of the constitutive relation is completed by prescribing a void growth kinetics model. Here we consider the void growth rate to be associated with the volumetric part of the plastic flow [81, 82]:

$$\dot{f}_c = (1 - f_c)\mathrm{tr}(\mathbf{D}^p_c) \tag{3.10}$$

The crystalline phase loses its load carrying capacity either when the void ratio reaches a critical value f_{cf}, or when the amorphous phase breaks down.

3.2.2 Amorphous resistance

The amorphous phase is composed of entanglement networks of randomly coiled tie chain segments. The resistance to deformation in the amorphous phase is provided by intermolecular and network orientation mechanisms. In the present model, these mechanisms are coupled in parallel (Fig. 3.2). The overall stress and deformation of the amorphous phase are related to the stresses and deformations of the intermolecular and

network resistances as

$$\mathbf{F}_a = \mathbf{F}_{aI} = \mathbf{F}_{aN} \tag{3.11}$$

$$\mathbf{T}_a = \mathbf{T}_{aI} + \mathbf{T}_{aN} \tag{3.12}$$

where $\mathbf{T}_{aI}$ is the amorphous intermolecular stress, $\mathbf{T}_{aN}$ is the network stress, and $\mathbf{F}_{aI}$ and $\mathbf{F}_{aN}$ are the deformation gradients in the intermolecular the network models, respectively.

The intermolecular resistance is responsible for the initial stiff stress-strain behavior of the amorphous phase, whereas the network resistance governs the response at large strains [16]. The intermolecular resistance arises primarily from the hindrance to the uncoiling and sliding of the randomly coiled tie chain segments by the surrounding molecules. The initial stiff stress-strain response is then followed by a viscoplastic flow once the intermolecular barriers to uncoiling and sliding are overcome. It is reasonable to consider that the elastic-viscoplastic behavior of the amorphous intermolecular region can be described by the same mathematical model used for the crystalline phase (Eqs. 3.2 - 3.10) with different parameters. In HDPE, the amorphous tie chains are present in their rubbery state at room temperature, which means these loosely packed tie chains have higher mobility and can slide past each other easily. Therefore, the contribution of the amorphous intermolecular resistance to applied loading is relatively small.

After the intermolecular barriers are crossed, the resistance to deformation arises from the stretch mechanism of the entanglement network of tie molecules. The network resistance exhibits a nonlinear hardening behavior, which is governed by the chain entanglement density, deformation rate, and temperature [76]. The deformation of the amorphous network is rate dependent due to the relaxation processes, such as molecular chain rotation and reptation, which are activated above the glass transition temperature. Similar to the elastic-plastic decomposition of the deformation gradient

of the crystalline phase, we separate the deformation of the network region into the elastic network orientation and plastic flow, i.e. $\mathbf{F}_{aN} = \mathbf{F}^e_{aN}\mathbf{F}^p_{aN}$, where $\mathbf{F}^e_{aN}, \mathbf{F}^p_{aN}$ are the deformation gradients of network orientation and plastic flow, respectively. Similar to Eq. 3.2, the velocity gradient $\mathbf{L}_{aN}$ are decomposed as: $\mathbf{L}_{aN} = \mathbf{L}^e_{aN} + \mathbf{L}^p_{aN}$, where $\mathbf{L}^e_{aN} = \dot{\mathbf{F}}^e_{aN}\mathbf{F}^{e^{-1}}_{aN}$, and $\mathbf{L}^p_{aN} = \mathbf{F}^e_{aN}\dot{\mathbf{F}}^p_{aN}\mathbf{F}^{p^{-1}}_{aN}\mathbf{F}^{e^{-1}}_{aN}$. The inelastic part of the velocity gradient is equal to the rate of deformation, i.e. $\mathbf{L}^p_{aN} = \mathbf{D}^p_{aN}$, by prescribing the plastic spin to be zero.

The network stress due to the stretch of the elongated molecular chain can be modeled by an eight-chain rubble elasticity model [76], i.e.

$$\mathbf{T}_{aN} = \frac{1}{J_N}\frac{nk_bT}{3}\frac{\sqrt{N}}{\lambda_N}\mathcal{L}^{-1}\left(\frac{\lambda_N}{\sqrt{N}}\right)\left(\overline{\mathbf{B}}^e_N - \lambda^2_N\mathbf{I}\right) \tag{3.13}$$

where the relative volume change is $J_N{=}(1-f_a)\det(\mathbf{F}^e_{aN})$ (f_a is the void fraction in the amorphous phase), n is the chain density, i.e. the number of chains present per unit volume of the amorphous phase, (the combined term $nk_bT/3$ is the hardening modulus), and N is the number of chain units between the entanglements. The effective elastic stretch is $\lambda_N = \sqrt{\mathrm{tr}(\overline{\mathbf{B}}^e_N)/3}$ where $\overline{\mathbf{B}}^e_N = \mathbf{F}^e_{aN}\mathbf{F}^{e^T}_{aN}/\sqrt{J^3_N}$. $\mathcal{L}^{-1}(x)$ is the inverse Langevin function, which can be approximated by $\mathcal{L}(x) = \coth(x) - (1/x)$. The term $\left(\overline{\mathbf{B}}^e_N - \lambda^2_N\mathbf{I}\right)$ represents the effective shear stretch tensor, $\mathbf{I}$ = second-order identity tensor. Eq. 3.13 predicts that the stress would rise dramatically as the chain stretch approaches the maximum possible stretch $\sqrt{N}$.

The viscous deformation of the entanglement network due to molecular relaxation mechanisms is described through a constitutive equation on the rate of inelastic deformation [19]

$$\mathbf{D}^p_{aN} = \dot{\gamma}^p_{aN}\frac{\mathbf{T}'_{aN}}{\sqrt{2}\tau_{aN}} \tag{3.14}$$

where $\dot{\gamma}^p_{aN}$ is the relaxation rate, the deviatoric network stress $\mathbf{T}'_{aN} = \mathbf{T}_{aN} - \frac{1}{3}\mathrm{tr}(\mathbf{T}_{aN})\mathbf{I}$,

and $\tau_{aN} = (\mathbf{T'}_{aN} : \mathbf{T'}_{aN}/2)^{1/2}$. The relaxation rate is given as

$$\dot{\gamma}^p_{aN} = \gamma_{N0} \frac{\tau_{aN}}{\lambda_p - 1} \tag{3.15}$$

where the inelastic stretch $\lambda_p = \sqrt{\mathrm{tr}(\mathbf{F}^p_{aN} \mathbf{F}^{p^T}_{aN})/3}$. The prefactor γ_{N0} includes the temperature dependence through the Arrhenius relation $\gamma_{N0} = C \exp(-Q/k_b T)$, where $C =$ constant, and $Q =$ activation energy barrier to be overcome for viscoplastic deformation of the amorphous network.

The aforementioned plastic deformation mechanisms lead to homogeneously distributed void growth in both the phases. As the deformation proceeds, the polymer exhibits a craze damage mechanism characterized by the appearance of localized damage zones, which are planar in structure. Crazes can be defined as arrays of voids separated by fibrils stretched along the principal tensile stress direction (Fig. 3.3). These fibrils bridge the planar surfaces and transfer the load. The growth and breakdown of these crazes lead to the formation and propagation of a traction free crack. Therefore, the stability of these crazes governs the failure mode in HDPE components.

It has been observed that crazing occurs preferentially in the amorphous region when the crystalline lamellae are stronger than the amorphous tie chains. This is a typical case for HDPE [84]. Meanwhile, when exposed to chlorinated environment, the HDPE experiences a considerable reduction in both the molecular weight and the inter-lamellar connectedness, which further intensifies the craze damage in the amorphous phase [84]. Therefore, in this study we consider that crazing occurs only in the amorphous phase.

The process of craze damage involves three stages: initiation, widening, and breakdown. The stability of the molecular chains surrounding the voids determines the onset of crazing in the amorphous phase. The voids localize into crazes when the

maximum principal stress σ_A in the amorphous phase exceeds a threshold, σ_{cr}, i.e. $\sigma_A \geq \sigma_{cr}$ provided that the hydrostatic stress $\bar{\sigma}$ of the amorphous phase is positive. In this case ($\sigma_A \geq \sigma_{cr}$), the fibrils start to get drawn out from the bulk entangled network into the voids. Oriented in the direction of the maximum principal stress, these highly stretched fibrils create an array of voids arranged perpendicular to the direction of maximum tensile stress forming crazes.

Previous studies have shown that the stress threshold σ_{cr} depends on many factors, such as the flow stress in the amorphous intermolecular region, the entanglement density, and the Van der Waal surface energy [87]. It has also been suggested that σ_{cr} is affected by the hydrostatic stress $\bar{\sigma}$ of the amorphous region ($\sigma_{cr} = F(\bar{\sigma})$) [20]. In this study, the dependence on the hydrostatic stress is not considered due to two reasons: 1) the present experimental calibration is limited to uniaxial tension specimens, which is not able to determine the dependence of σ_{cr} on the hydrostatic stress, and 2) the subsequent numerical simulations focus on tensile failure of double-edge notched specimens under a plane stress condition, and it reasonable to consider $\sigma_A \approx 3\bar{\sigma}$. Therefore, the craze initiation criterion can be rewritten as $\sigma_A = \sigma_c$, where σ_c = constant.

After the craze damage initiates, the inelastic behavior of the amorphous phase is primarily governed by the widening of the crazes. Craze widening occurs inside the active zone at the boundary of the crazes, where fibrils are formed through the loss of entanglements [89] (Fig. 3.3). The loss of entanglements could be attributed to either the breakdown of polymer chains (chain scission), which occurs at high deformation rates and low temperatures, or sliding of polymer chains (disentanglement), which occurs at low deformation rates and high temperatures [85, 86]. On the continuum level, the inelastic response of the amorphous phase can be described by a phenomenological constitutive

relation proposed by [20]:

$$\mathbf{D}^p_{aN} = \mathbf{D}^p_{aI} = \gamma_{cz}\mathbf{e}_1 \otimes \mathbf{e}_1 \qquad \text{if } \sigma_A > \sigma_c \tag{3.16}$$

$$\text{and} \quad \gamma_{cz} = \gamma_{cz0}\left(\frac{\sigma_A}{s_{cz}}\right)^{1/m_{cz}} \tag{3.17}$$

where $\mathbf{e}_1$ = unit vector denoting the direction of the maximum principal stress σ_A, γ_{cz0} = craze flow constant, m_{cz} = rate sensitivity constant, and s_{cz} = craze flow resistance.

Craze breakdown occurs when two opposite craze boundaries reach a critical separation and the fibrils break down at the craze-bulk interface. The craze breakdown leads to the formation of a traction free crack. The craze strain ϵ_{cz} is defined as the inelastic strain accumulated after the onset of craze initiation, i.e.

$$\epsilon_{cz}(t) = \int_{t_0}^{t} \gamma_{cz}(t')\mathrm{d}t' \tag{3.18}$$

where t_0 = time when craze initiation begins. Since the width of the craze zone represents a material constant (similar to the width of fracture process zone) [94], the critical separation of craze boundaries is equivalent to a critical strain value ϵ_f. We consider that a craze breaks down once ϵ_{cz} reaches ϵ_f.

3.2.3 Effect of corrosion on the constitutive behavior

In the section, we discuss how the proposed constitutive model would be affected by chlorine corrosion. Exposure to chlorine would change the morphology of HDPE, and influence the deformation mechanisms. Chlorine preferentially diffuses into the amorphous phase, where the molecular chains are loosely packed and randomly entangled, instead of the densely packed crystalline phase [28]. Therefore, we consider that the corrosion only influences the constitutive behavior of the amorphous phase.

In the amorphous phase, the chlorine oxidizes the tie molecules causing chain scission. The chain scission events causes substantial changes in the morphology, as shown in Fig. 3.4. These morphological changes have a profound influence on the mechanical properties and are reflected directly in the molecular weight of HDPE, which can be measured experimentally using techniques such as size exclusion chromatography (SEC). Therefore, in this study we use the relative molecular weight $m_w = M_w/M_{w0}$ to quantify the degree of corrosion, where M_w is the molecular weight at a given exposure time and M_{w0} is the initial undegraded molecular weight. As mentioned earlier, the chain scission in the amorphous phase is accompanied by an increase in the crystallinity due to chemi-crystallization. However, the newly formed lamellae do not contribute to the overall load carrying capacity of HDPE, which is reflected in Eq. 3.1. The change of crystallinity can be experimentally measured using the differential scanning calorimetry (DSC).

Chain scission of tie molecules reduces the length of these tie chains and also cuts off the entanglements (Fig. 3.4). This change implies a decrease in chain density n (Eq. 3.13) as the corrosion proceeds. In terms of the stress-strain relation, the decrease in n is manifested by a decrease in the hardening modulus ($nk_bT/3$). On the other hand, the number of molecular units between entanglements, N, remains unaffected by chain scission events. The effect of chain scission on the molecular relaxation parameter γ_{N0} cannot be easily isolated in the experiments, and therefore it is assumed to remain unaffected by the corrosion.

The amorphous intermolecular resistance originates from the hindrance to uncoiling of the tie molecules by adjacent molecules. This hindrance is assumed to be unaffected by the corrosion since the molecules occupy the same space after chain scission. This assumption can be checked against the measured yield strength at different corrosion levels. Based on the present constitutive model, the yield strength of HDPE is governed by the intermolecular contribution from both the crystalline and amorphous

phases (Eq. 3.1). As will be shown in the experimental validation, the change in the yield strength observed in this study can be captured based on the change of crystallinity.

Corrosion-induced change of the entanglement network promotes craze damage in the amorphous phase. Corrosion influences all three stages of craze damage: craze initiation, craze widening, and final breakdown. With an increasing level of corrosion, shorter chains can easily disentangle and orient into craze fibrils, leading to an early formation of crazes. This is because the threshold stress σ_{cz}, at which crazes initiate, is directly related to the entanglement density [87]. As mentioned earlier, the entanglement density decreases with an increasing level of corrosion. This leads to a decrease in σ_{cz} with the molecular weight.

Corrosion also influences the widening mechanism of the crazes, which involves chain scission and disentanglement. The aforementioned morphological changes in the amorphous network suggest that corrosion would accelerate the craze widening mechanism. Based on the present formulation (Eq. 3.16), we consider the craze flow resistance s_{cz} decreases with the molecular weight while other parameters, i.e. m_{cz} and γ_{cz0} are assumed to be independent of the molecular weight.

The final craze breakdown occurs when the opposite surfaces of the craze reach a critical separation, which is dependent on the chain length. In undegraded HDPE with long tie chains, the formation of crazes is a stable process and the stretch of the crazes to failure requires significant energy. When the polymer undergoes chain scission, the chain length decreases and less energy is required to reach the point of craze breakdown. Hence, the critical strain ϵ_f is considered to decrease with the molecular weight.

The foregoing discussion indicates that the exposure to chlorinated environment would promote craze damage. When the molecular weight is sufficiently low, the craze stress threshold could be so low that the crazing damage preceeds the viscoplastic deformation mechanism. Meanwhile, corrosion also causes craze to break down at a smaller

critical separation, which implies a brittle failure behavior. Therefore, by relating the constitutive parameters to the molecular weight, the present model naturally captures the transition from the ductile failure to brittle failure with as corrosion increases.

3.3 Experimental Investigations

To calibrate and validate the constitutive model, a series of experiments was designed and performed on HDPE specimens. The specimens were prepared by extruding unimodal HDPE into 70-100 μm thick sheets. The sheets were post-processed in an oven to obtain two sets of specimens at two different initial crystallinities, labelled as A and B.

These thin HDPE sheets were exposed to a water bath with a 5 ppm concentration chlorine solution at 65°C (corresponding to an oxidation-reduction potential (ORP) of approximately 825 mV) for accelerated chemical corrosion of the polymer. The water bath design and operation are described in detail in [97]. The HDPE sheets were submerged in the water bath for up to 750 hours and batches of specimens were removed at intervals of 250 hours. The morphology of the HDPE specimens, i.e. the crystallinity and the molecular weight, was characterized at each exposure interval. The crystallinity was determined by DSC and the molecular weight was measured by SEC [98]. These morphology measurements were made for several material points from the specimen and the average value was used in the model calibration. Tensile tests and double edge notch tests were performed on specimens that were prepared from these sheets.

For the tensile tests, dog-bone specimens with a gauge length of 5mm×22mm were die-cut from the 700-100 μm HDPE sheets. Uniaxial tensile tests were performed at four (engineering) strain rates ($\dot{\epsilon} = 10^{-1}$/s, 10^{-2}/s, 10^{-3}/s, and 10^{-4}/s) and four exposure times (0, 250, 500, and 750 hours) following the procedures described in ASTM D1708 [99]. The true stress-strain curves were obtained by digital image correlation

(DIC) using NCORR software [100]. Based on DIC measurements in the necking zone, the logarithmic strain in the loading direction as well as the in-plane horizontal deformation of the necking zone were calculated. The change in thickness of the necking zone was considered to be proportional to the change in width because the material is isotropic. The true stress was evaluated based on the change of cross-section area of the necking zone. Note that the DIC measurement becomes inaccurate when the gray pattern of the DIC image is indiscernible due to stress-whitening. This happens at an approximate true strain of 120%.

The true stress-strain data were used to calibrate the proposed constitutive model. Fig. 3.5a shows the typical stress-strain curves of the undegraded specimens A and B. Based on the present modeling framework (Eq. 3.1), the stress-strain responses attributed to the crystalline and amorphous phases are separated (Fig. 3.5b and c). The crystalline stress-strain response is governed entirely by the intermolecular resistance, whereas the amorphous stress-strain response is governed by different mechanisms depending on the deformation level. At small strains, the intermolecular resistance is dominant. Upon yielding, the response at intermediate strain level is governed primarily by the network orientation. For very large applied strains, the response is dominated by the crazing mechanism.

The intermolecular resistance parameters of both phases are determined using the small strain response before yielding. The network model parameters, which include the chain density n, the number of rigid links between the entanglements N, and the relaxation constant γ_{N0}, are obtained by fitting the intermediate strain range of the stress-strain curve of the amorphous phase.

Given the calibrated intermolecular and network model parameters, the predicted stress strain curve is compared to the experimental data. The point of deviation from the experimental curve indicates the initiation of crazing. This deviation point is

used to determine the threshold stress for crazing initiation. The remaining model parameters for crazing damage are subsequently calibrated by curve fit to the stress-strain data over the large strain range. It should be pointed out that, due to the limitation of the DIC analysis, the experimental stress-strain curve of unexposed specimen may not reach the strain level, at which the craze damage initiates.

As discussed in Section 3.2.3, chemical corrosion affects only the chain density, n, and the crazing parameters σ_{cz}, s_{cz}, and ϵ_f. The corrosion effect is expressed in terms of the molecular weight and crystallinity. The crystallinity was explicitly measured in the experiments, and the dependence of the constitutive parameters on the molecular weight is determined by optimum fitting of the stress-strain curves of degraded specimens.

In a separate set of experiments, double-edge notched (DEN) tests were performed following ASTM D5397 [101]. The tests were performed on A specimens at exposure times of 0, 500, and 750 hours. The overall specimen size was 30×50 mm, and the ligaments (L_g = 8 mm, 12 mm, and 16 mm) were prepared across the 30 mm dimension, such that the ligament length was 27, 40, and 53 % of the specimen width. Note that, due to the brittle failure behavior at long exposure times, DEN samples could not be prepared from specimens exposed for more than 750 hours. The DEN specimens were tested under uniaxial deformation at 0.165 mm/s. The complete load-deflection curves were recorded for each specimen. The calibrated constitutive model was used to simulate the DEN fracture tests, and the simulated load-deflection responses were compared with the experimental measurements.

3.4 Results and Discussion

3.4.1 Calibration results

In the present experiments, the morphological change of HDPE due to corrosion was measured by the change in molecular weight and crystallinity. Table 1 presents the relative molecular weights ($m_w = M_w/M_{w0}$) and the change of crystallinity z for different exposure times. The average initial molecular weight M_{w0} for specimens A and B was 199462 and 194994 g/mol, respectively, which reduced to 78939 and 101580 g/mol, respectively. The decrease in molecular weight with increasing corrosion is caused by chain scission events. On the other hand, the initial crystallinity for specimens A and B was 74.9% and 83.3%, respectively, and after 750 hours exposure, it increased to 83.5% and 91.7%, respectively. This increase in crystallinity is due to the migration of shortened chains formed after chain scission at a relatively higher temperature (65°C). The constitutive model was calibrated based on the measured true stress-strain tensile test data in two steps: 1) both specimens A and B were used to determine the constitutive parameters for the undegraded case, and 2) only A specimens were used to determine the dependence of constitutive parameters on the molecular weight. The test results of specimens B were used for the model validation.

The stress-strain curves of undegraded specimens A and B measured at four strain rates are shown in Fig. 3.6. Each experimental curve represents the average response of three specimens. The stress-strain curves show an initial stiff response due to the intermolecular resistance in both the crystalline and amorphous phases. The stress-strain behavior then exhibits a viscoplastic response, where an increase in the loading rate produces a higher stress. The yield strength of the material increases with the crystallinity since the crystalline intermolecular resistance is considerably greater than that of the amorphous phase. In the calibration, the elastic moduli of both phases

phase, E_c and E_a were obtained from the initial tangent of the stress-strain curve. The intermolecular parameters that governed the rate dependence, γ_{0i} and ΔG_i $(i = a, c)$, were obtained using the yield stress at different loading rates. Other model parameters were taken from the literature: $\nu_i = 0.45$; $\alpha_i = 0.2$ and $s_{i0} = 0.15E_i/2(1 + \nu_i)$ [16]; $q_1 = 1.5$ and $q_2 = 1$ [83]; $\sigma_{fi0} = 1.18$MPa, $f_{ic} = 0.15$, and $f_{if} = 1.0$ [83, 94] . Fig. 3.6 shows that the model fits the measured stress-strain curves of undegraded specimens very well. It is found that the craze model is not needed for fitting over the present strain range. Therefore, the crazing parameters for the unexposed specimens can not be determined.

The effect of chlorine-induced chemical corrosion on the constitutive response is captured by calibrating the relevant parameters $n, \sigma_c, s_{cz}, \epsilon_f$ as a function of m_w. Representative true stress-strain curves for A specimens measured at the four strain rates and at exposure times of 250, 500, and 750 hours are shown in Fig. 3.7. These exposure durations result in decreasing molecular weights, corresponding to $m_w = 0.93$, 0.63, and 0.39, respectively. These tensile test results indicate that the chemical corrosion has a minimal effect on the pre-yielding small strain response. Thus, the constitutive responses of the intermolecular amorphous and crystalline phases are not affected by corrosion.

The post-yielding load resistance is reduced significantly as the molecular weight decreases. The behavior in this deformation region is captured by the network and the crazing models. We calibrate the chain density, n, of the amorphous network, and the crazing parameters (σ_{cz}, s_{cz} and ϵ_f) to fit optimally the measured stress-strain curves for each level of corrosion. The following empirical functions shows the relationship between

normalized n, σ_{cz}, s_{cz} and ϵ_{cz}, and the normalized molecular weights, m_w (Fig. 3.8):

$$E_h/E_{h0} = -0.93m_w^2 + 2.16m_w - 0.23 \quad (3.19)$$

$$\sigma_c/\sigma_{c0} = 3.41m_w^2 - 3.21m_w + 0.80 \quad (3.20)$$

$$s_{cz}/s_{cz0} = 2.27m_w^2 - 1.85m_w + 0.58 \quad (3.21)$$

$$\epsilon_f/\epsilon_{f0} = 0.57m_w + 0.43 \quad (3.22)$$

where E_{h0}, σ_{c0}, and s_{cz0} and ϵ_{f0} are the corresponding values of E_h, σ_c, s_{cz} and ϵ_f for undegraded HDPE. These fittings are valid for relative molecular weight m_w ranging from 0.35 to 1.0. This is because, when m_w is less than 0.35, the property is significantly degraded and the material has very little load resistance (less than 10% of the strength of undegraded material). Consequently, at the crack tip which experiences significant stress concentration, such a degraded material element would fail right away. The the unexposed material parameters attain the following values: for the crystalline phase.During oxidation, chain scission occurs and the crystallinity increases due to chemi-crystallization. This increase in crystallinity was measured by differential scanning calorimetry for the particular HDPE tested in [24]. The following empirical function is fit to measured relationship between the crystallinity and molecular weight of HDPE:

$$z = -0.18m_w^4 + 0.63m_w^3 - 0.71m_w^2 + 0.12m_w + 0.89 \quad (0.35 \leq m_w \leq 1.0) \quad (3.23)$$

All of these parameters decrease with corrosion levels, which is directly reflected in the stress-strain response. The decrease in the chain density due to chain scission leads to a decrease in the hardening modulus. The decrease in the crazing parameters indicates a weaker resistance to crazing damage, as discussed in Section 3.2.3. Due to the capacity of DIC measurement, the final craze breakdown strain ϵ_f is determined only for the cases of $m_w = 0.63$ and 0.39, and a considerable decrease is observed. Table 2 summarizes

the calibrated values of all the model parameters for both the undegraded and degraded cases.

3.4.2 Model validation

Once calibrated, the present constitutive model was used to predict the stress-strain data of specimens B at two corrosion levels ($m_w = 0.75$ and 0.52). The change of crystallinity at these two corrosion levels were experimentally measured. The crystallinity is initially 83.3%, and increases to 90.2% and 91.7% after 500 and 750 hours of exposure, respectively (Table 1). Fig. 3.9 shows the model agrees well with the stress-strain curves measured at different strain rates. This result indicates that the present model framework is able to capture the effect of crystallinity on the stress-strain response for degraded specimens.

The model was also validated with the DEN fracture test data for A specimens. The constitutive model was incorporated into a commercial finite element (FE) software and the fracture experiments on DEN specimens were simulated. In the FE simulation, the specimen was modeled by 3D elements with mesh refinement near the crack tips. Following the experiments, a displacement controlled load with rate of 0.165 mm/sec was applied at the top surface of the specimen and the bottom surface was fixed. It has been long known that the FE simulations of localized damage suffers spurious mesh sensitivity [102, 103, 63, 104]. Here we adopted the crack band model for objective FE simulation of the crazing damage. In the model [102], we set the FE size in the direction of the load equal to the physical width h_0 of the localized crazing zone, which is approximately 0.7 mm [94].

Since the molecular weight and crystallinity were explicitly measured in the DEN fracture tests, the corresponding constitutive parameters at different exposure durations were input to the FE model (Table 2). Fig. 3.10 shows that the model prediction

agrees well with the experimental measurement for all specimens at all three exposure conditions. It is seen that the undegraded specimens exhibit a relatively ductile response, which is featured by a gentle softening beyond the peak load. The damage in these specimens arises due to void growth that leads to a ductile failure. In contrast, specimens with 500 hour exposure exhibits a steeper softening slope. In the present model, this behavior is explained by the combined effect of the decreasing hardening modulus of the amorphous network, the early onset of crazing damage, and the deterioration of the crazing resistance. For specimens exposed after 750 hours, the load-displacement curve shows almost a vertical drop after the peak load. Despite the brittle post-peak behavior, the pre-peak regime of the load-displacement curve exhibits non-linearity, suggesting plastic flow occurs right before craze breakdown. The present model is able to predict this behavior due to the significant decrease in the craze stress threshold and the final craze breakdown strain. On the other hand, it is interesting to note that the peak load capacity of the specimen is not affected by the corrosion since the initial part of the curves are governed by the intermolecular resistances, which remains unchanged during the corrosion process.

Table 3.1: Molecular weight and crystallinity of HDPE measured at different exposure hours

Specimen batch	Exposure time (hours)	Crystallinity z %	Molecular weight M_w (g/mol)	Relative molecular weight m_w
A	0	74.9±0.3	199462 ± 16666	1.00
	250	78.2±1.1	185111 ± 21929	0.93
	500	82.6±4.5	125594 ± 17322	0.63
	750	83.5±3.6	78939 ± 14400	0.39
B	0	83.3±1.8	194994 ± 1320	1.00
	500	90.2±0.6	146961 ± 12199	0.75
	750	91.7±1.5	101580 ± 11195	0.52

Table 3.2: Calibrated constitutive parameters

Submodel	Model Parameter		Exposure time			
			0 hours	250 hours	500 hours	750 hours
Crystalline intermolecular	Crystalline elastic modulus	E_c (MPa)	2000			
	Rate constant	γ_{c0} (s^{-1})	2×10^7			
	Crystalline plastic flow activation energy	ΔG_c (J)	9.11×10^{-20}			
Amorphous intermolecular	Amorphous elastic modulus	E_a (MPa)	35			
	Rate constant	γ_{a0} (s^{-1})	2×10^7			
	Amorphous plastic flow activation energy	ΔG_a (J)	8.68×10^{-20}			
Amorphous network	Rigid links between entanglement	N	50			
	Chain density	n (m^{-3})	7.73×10^{27}	7.24×10^{27}	6.03×10^{27}	3.62×10^{27}
	Temperature dependent pre-factor	γ_{N0} (s^{-1})	10^{-7}			
Craze damage	Craze stress threshold	σ_c (MPa)	-	120	25	10
	Craze flow resistance	s_{cz} (MPa)	-	30	12.5	7.5
	Craze flow parameter	γ_{cz0} (s^{-1})	-	10^{-7}	10^{-7}	10^{-7}
	Craze flow rate sensitivity parameter	m_{cz}	-	0.15	0.15	0.15
	Craze breakdown strain	ϵ_f	-	-	0.69	0.57

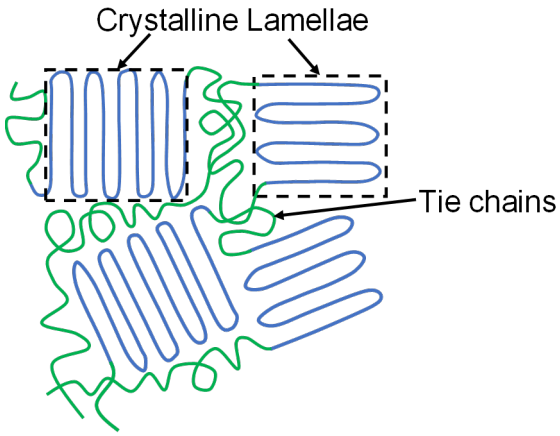

Figure 3.1: Schematic of microstructure of HDPE featured by regularly arranged crystalline lamellae and amorphous tie molecules.

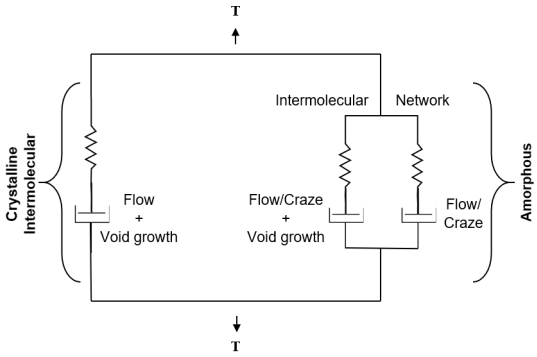

Figure 3.2: Rheological model of HDPE representing the different deformation and damage modes in the crystalline and amorphous phases.

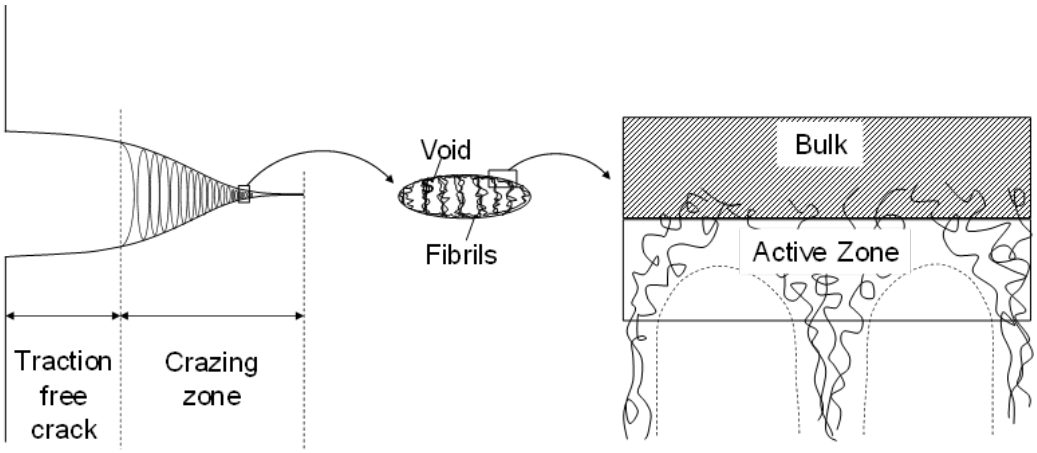

Figure 3.3: Schematic of microstructure of crazes formed in the amorphous phase of HDPE.

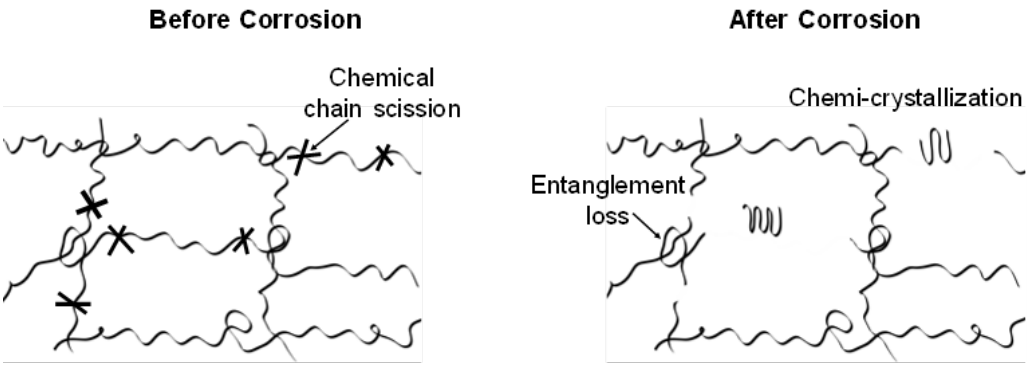

Figure 3.4: Schematic of the amorphous entanglement network before and after chain scission.

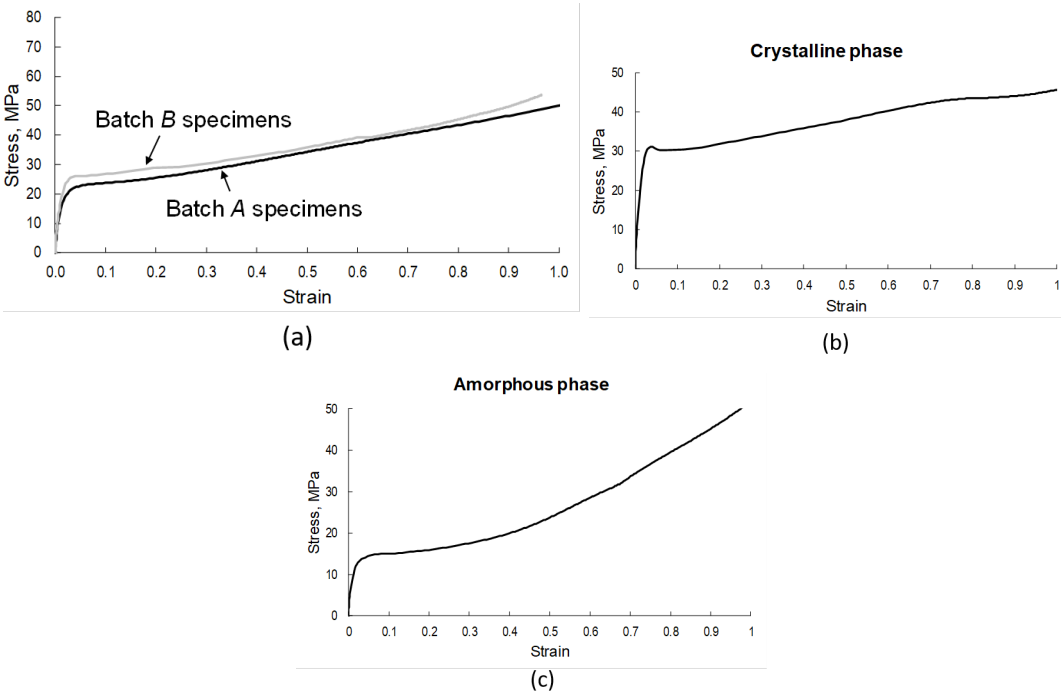

Figure 3.5: a) A typical stress-strain response of undegraded HDPE, b)-c) stress-strain responses of the crystalline and amorphous phases.

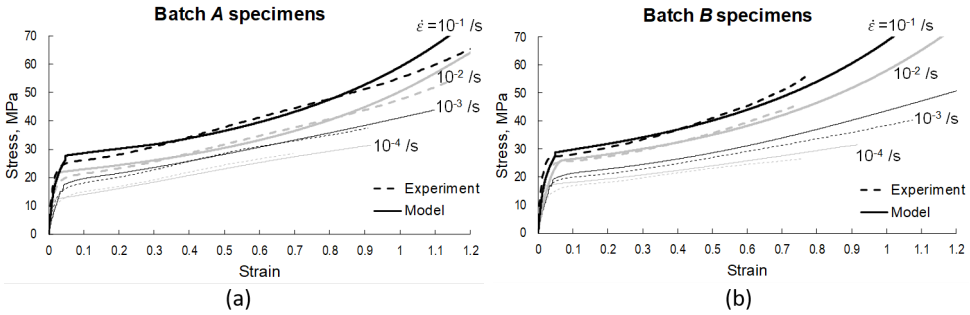

Figure 3.6: Model calibration using experimental true stress-strain curves at different strain rates for unexposed a) specimens A, b) specimens B.

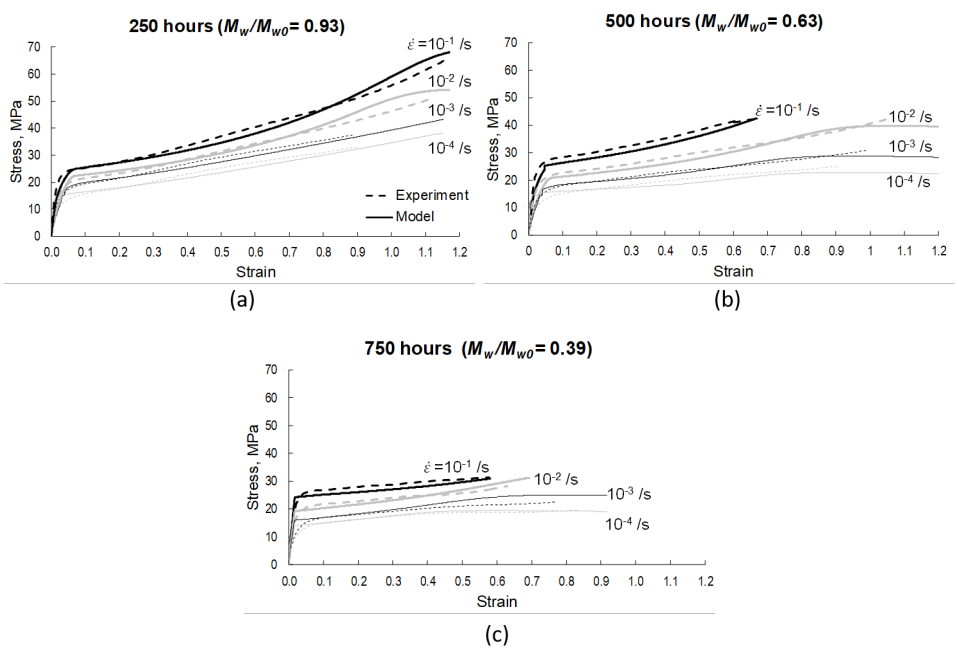

Figure 3.7: Optimum fits of experimental stress-strain curves for bath A specimens with different exposure times: a) 250 hours (m_w=0.93), b) 500 hours (m_w=0.63), and c) 750 hours (m_w=0.39).

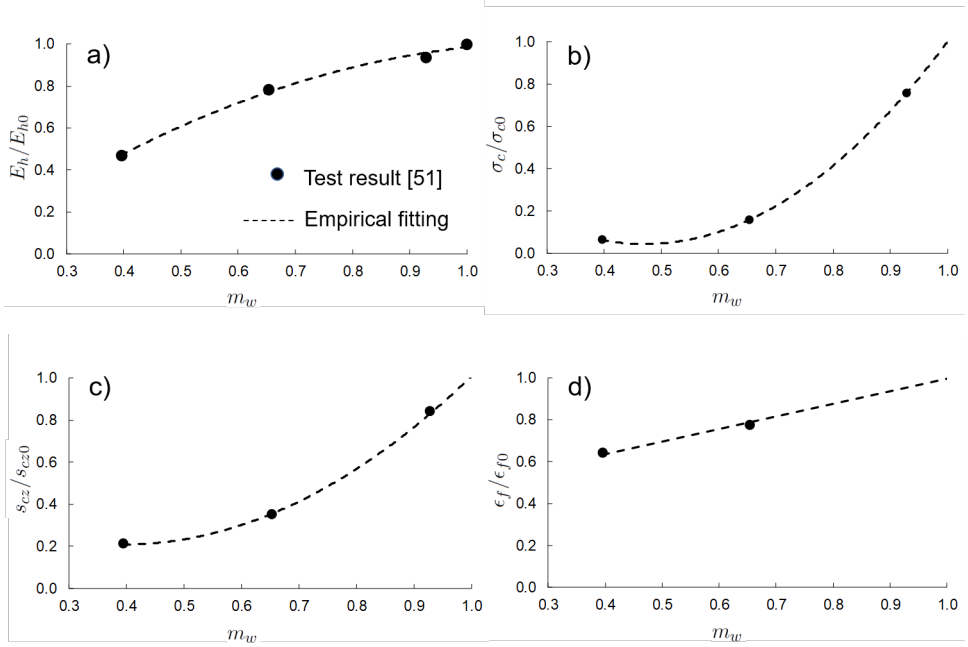

Figure 3.8: Effect of the molecular weight on constitutive parameters.

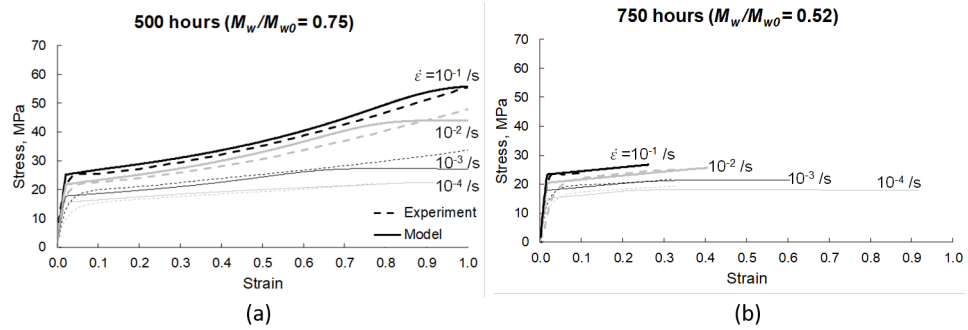

Figure 3.9: Comparison between the predicted and measured stress-strain curves for specimens B uniaxial tensile specimens under exposed conditions.

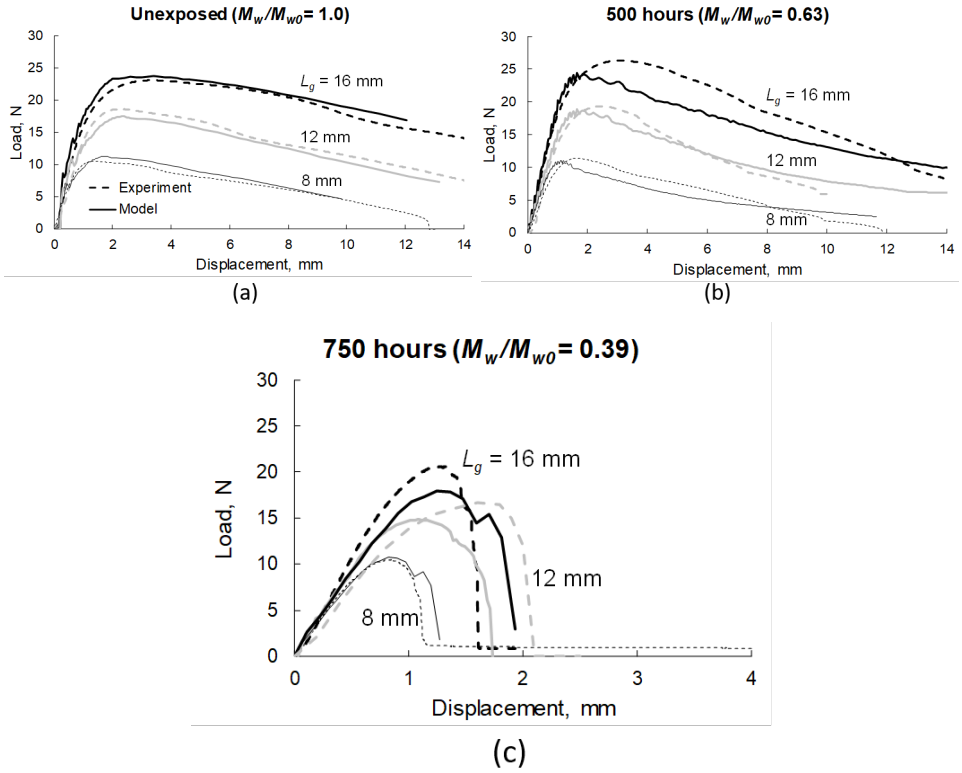

Figure 3.10: Predicted and measured load-displacement curves for DEN specimens with different exposure times: a) 0 hours (m_w=1.0), b) 500 hours (m_w=0.63), and c) 750 Hours (m_w=0.39).

Chapter 4

Reduced order kinetics model for HDPE corrosion in bleach solution

When polymers are exposed to a corrosive environment, chemical species diffuse into the polymer and cause localized degradation at the polymer-liquid boundary. Crack propagation under mechanical loading causes further ingress of the corrosive liquid, thereby accelerating the corrosion process. Thus, the corrosion kinetics model is needed along with the mechanical model to simulate the lifetime of polymers under SCC. The kinetics model should also be computationally efficient to be coupled with the mechanical model to perform chemo-mechanical analyses. The chapter describes the formulation of the reduced order corrosion kinetics model in section 4.1, calibration of the model in section 4.2, and model validation in section 4.3.

4.1 Reduced-Order Diffusion-Reaction Model for Corrosion Kinetics

The corrosion process begins with the dissociation of the corrosive chemicals into radicals. These highly reactive radicals react with the polymer chains, beginning an oxidation process that leads to chain scission and cross linking. Chain scission and cross-linking events change the micro-structure of the polymer entanglement network. This change in entanglement network is reflected in the molecular weight that is used to link the chemical model to the mechanical one. The relationship among chain scission, cross linking and the molecular weight is as follows [105]:

$$\frac{1}{M_w} - \frac{1}{M_{w0}} = \frac{s}{2} - 2x \tag{4.1}$$

where s and x are the number of chain scission and cross linking events (per kg-mol^{-1}), respectively. In the case of HDPE exposed to a chlorinated water environment, chain scission events dominate over cross-linking events and the molecular weight decreases [106]. By neglecting cross-linking, Eq. 4.1 can be rewritten in the following dimensionless form:

$$\frac{1}{m_w} - 1 = \frac{1}{2}\eta\bar{s} \tag{4.2}$$

where $\bar{s} = s/s_m$, $\eta = M_{w0}s_m$, $s_m = 2(M_{c0}^{-1} - M_{w0}^{-1})$ is the theoretical maximum possible number of scission events, and M_{c0} is molecular weight of the monomer.

To prolong the lifetime of polymer components, antioxidants are added to the polymer. Antioxidants have a high affinity for the corrosive oxidizing agents, such that the reaction between the corrosive chemicals and antioxidants proceeds much faster than the oxidation reaction with the polymer. Therefore, the polymer oxidation is delayed until the antioxidants are depleted, but the rate of the reaction between the polymer and radicals is unaffected. In this study, we consider the corrosion reaction of HDPE,

with no antioxidant additives, exposed to an oxidative bleach solution.

Several studies have proposed comprehensive kinetics models for oxidation that track cross linking and chain scission events along with intermediate reaction species. Mikdam et al. (2017) developed a corrosion kinetics model for polyethylene in bleach disinfected water. This model predicts the time evolution and space distribution of the concentration of reactants, number of chain scission and cross-linking events, as well as the bi-product concentrations [26]. Though the model is comprehensive, it requires modeling numerous reactions, intermediate species, and chemical yields of multiple species, that makes it computationally inhibitive for coupled chemomechanical analysis.

The only output required from the kinetics model to couple it with the mechanical model is chain scission $\bar{s}$. For bleach disinfected water, the hydrolysis reaction causes the formation of hypochlorous acid (HOCl), which is the dominant corrosive species. HOCl dissociates into OH^+ and Cl^- radicals, which react with the polymer to form other radicals along with scission and other oxidation products. In this study, we propose that, for a given corrosion process of HDPE in bleach water, the rate of chain scission is related to the concentration of HOCl, and the current chain scission state:

$$\frac{\mathrm{d}\bar{s}}{\mathrm{d}t} = f([\mathrm{HOCl}], \bar{s}) \tag{4.3}$$

The advantage of Eq. 4.3 is that only the time evolution and space distribution of HOCl are tracked: other reactions of intermediate species are lumped into the kinetics function $f([\mathrm{HOCl}], \bar{s})$. As will be discussed later, this kinetics function is determined by fitting the reduced order model to the result of the full model from [26].

The diffusion and chemical dissociation changes in [HOCl] can be described by the modified Fick's law:

$$\frac{\mathrm{d}[\mathrm{HOCl}]}{\mathrm{d}t} = D_{HOCl}\nabla^2[\mathrm{HOCl}] - k_{HOCl}[\mathrm{HOCl}] \tag{4.4}$$

where t is time, and k_{HOCl} and D_{HOCl} are the dissociation and the diffusion coefficients of HOCl, respectively. The concentration of HOCl on the polyethylene surface exposed to bleach water is given by [26]

$$[\mathrm{HOCl}]_s = \kappa(1-z)[\mathrm{HOCl}]_w \exp\left(-\frac{U_s}{k_b T}\right) \tag{4.5}$$

where κ, U_s are constants, and z is the crystalline fraction of the polymer, and $[\mathrm{HOCl}]_w$ is the HOCl concentration in the solution. The surface concentration $[\mathrm{HOCl}]_s$ provides the boundary condition for Eq. 4.4. In the present study, we consider exposure at constant temperature.

The functional form for predicting chain scission events (Eq.4.3) is obtained by studying the complete corrosion kinetics model available in the literature [26]. The model was used to simulate a 1-D diffusion and reaction process in HDPE exposed to bleach water. The model predicts that the spatial distribution of [HOCl] reaches a steady state quickly. By examining the chain scission behavior at different locations (i.e. at different [HOCl]), we observe the following features: 1) in the initial phase when the polyethylene bond (-C-C-) is abundant, the rate of oxidation reaction and the radical concentration increase rapidly as the reaction proceeds; 2) after some time, the reaction rate is limited by the availability of the polyethylene bonds; and 3) the reaction rate is strongly governed by [HOCl]. To describe these features, we propose the following functional form for the chain scission kinetics:

$$\frac{\mathrm{d}\bar{s}}{\mathrm{d}\tau} = \frac{b + a\bar{s}}{1 + c\bar{s}} \tag{4.6}$$

where $\tau = k_{HOCl}t$, and a, b, and c are parameters that are functions of [HOCl] and the reaction rates of all the intermediate reactions. Referring to Eq.4.6, at the initiation of the reaction, $\bar{s}$ increases at a rate of b. As chain scission $\bar{s}$ approaches its maximum value ($\bar{s} \to 1$), the scission rate asymptotically approaches $(a+b)/(1+c)$. To ensure

that the final scission rate is larger than the initial scission rate, we require $a > bc$ for any given [HOCl]. Note, the condition $a > bc$ also implies that, for a given [HOCl], the rate of chain scission is always increasing with $\bar{s}$ and approaches an asymptotic limit.

The reduced order diffusion and reaction model (Eqs. 4.3-4.6) provides the distribution of the oxidizing agent (HOCl) and the chain scission events. Based on Eq. 4.2, the number of chain scission events determines the molecular weight, which is input to the constitutive model. The main advantage of the present model is that it contains only one partial differential equation which, when combined with the constitutive model, can be implemented in commercial FE software for coupled chemomechanical analysis.

The present reduced order diffusion-reaction model is developed for HDPE exposed to bleach solution. Nevertheless, the model framework can be applied to other corrosion processes, which involve one dominant corrosion species, and the intermediate reactions can be lumped into the kinetics of chain scission.

4.2 Corrosion model calibration

Parameters a, b, and c of the reduced order chain scission model (Eq. 4.6) are determined by calibration to the chain scission rate predicted by the full model (from [26]). In particular, the calibration is based on 1D diffusion-reaction in HDPE of crystallinity $z = 0.75$ exposed to bleach water of 5 ppm [HOCl] at $T = 60°$C and pH=6.5 (Fig. 4.1a). We simulate a 300-day diffusion-reaction process.

Fig. 4.1b presents normalized concentration profiles for $\bar{C}_{HOCl} = [\text{HOCl}]/[\text{HOCl}]_s$ as a function of sample thickness, calculated by the full model. The profiles show an exponential decay along the thickness direction with nearly zero concentration at the center-line. The figure also indicates that a steady state is reached relatively quickly

when the HOCl net influx due to diffusion equal the rate of dissociation. As expected, the thickness of the layer where [HOCl] is highly concentrated is governed by the length scale $\sqrt{D_{HOCl}/k_{HOCl}}$. Given the steady state concentration profile, the evolution of chain scission events, $\mathrm{d}\bar{s}/\mathrm{d}\tau vs.\bar{s}$, is readily determined as a function of $\bar{C}_{HOCl}$ (Fig. 4.1c) (Note each $\bar{C}_{HOCl}$ corresponds to a location through the thickness of the specimen). By optimum fitting this result, the values of a, b, and c are determined:

$$a = 1.78 \times 10^{-10} \times [\mathrm{HOCl}]^{0.08} \tag{4.7}$$

$$b = 2.22 \times 10^{-7} \times [\mathrm{HOCl}]^{0.5} \tag{4.8}$$

$$c = 2.22 \times 10^{-4} \times [\mathrm{HOCl}]^{-0.15} \tag{4.9}$$

Fig. 4.1d shows that the time evolution of the relative molecular weight predicted by the present model matches well that predicted by the full model. Note that parameters a, b, and c are also temperature dependent. If a different temperature is considered, the parameters of the reduced-order kinetics model must be recalibrated.

4.3 Corrosion model validation

To demonstrate the robustness of the present model, we apply the model to simulate a 2D diffusion reaction case.The specimen as shown in Fig. 4.2 is modeled. This specimen has the same geometry as the quarter of the specimen in Fig. 5.2, but of a much smaller size ($h = 9$ μm, $w = 6$ μm and $a_0 =$ 1.5 μm) given the extensive computational time required by the full model. Due to the symmetry, we simulate a 750-hour diffusion-reaction process of a quarter specimen.

The simulation yields the time evolution and spatial distribution of molecular weight, as shown in Fig. 4.3a. The present model predicts that the material degradation occurs in a narrow region (~ 0.15 μm) close to the specimen edge and crack surface.

The predicted spatial distributions of molecular weight at different times (250, 500, and 750 hours) are compared with those predicted by the full model, and the relative errors are plotted in Fig. 4.3b. The comparison shows the difference in the predicted molecular weight is less than 7%. For SCC analysis, the material degradation along the crack path is critical. A comparison of model predictions of m_w along the crack path, the ligament, is shown in Fig. 4.3c. It is seen that the maximum relative difference is about 7% at 750 hours. The close agreement indicates that the present reduced order model is sufficiently accurate for predicting the time evolution and spatial distribution of molecular weight during the corrosion process.

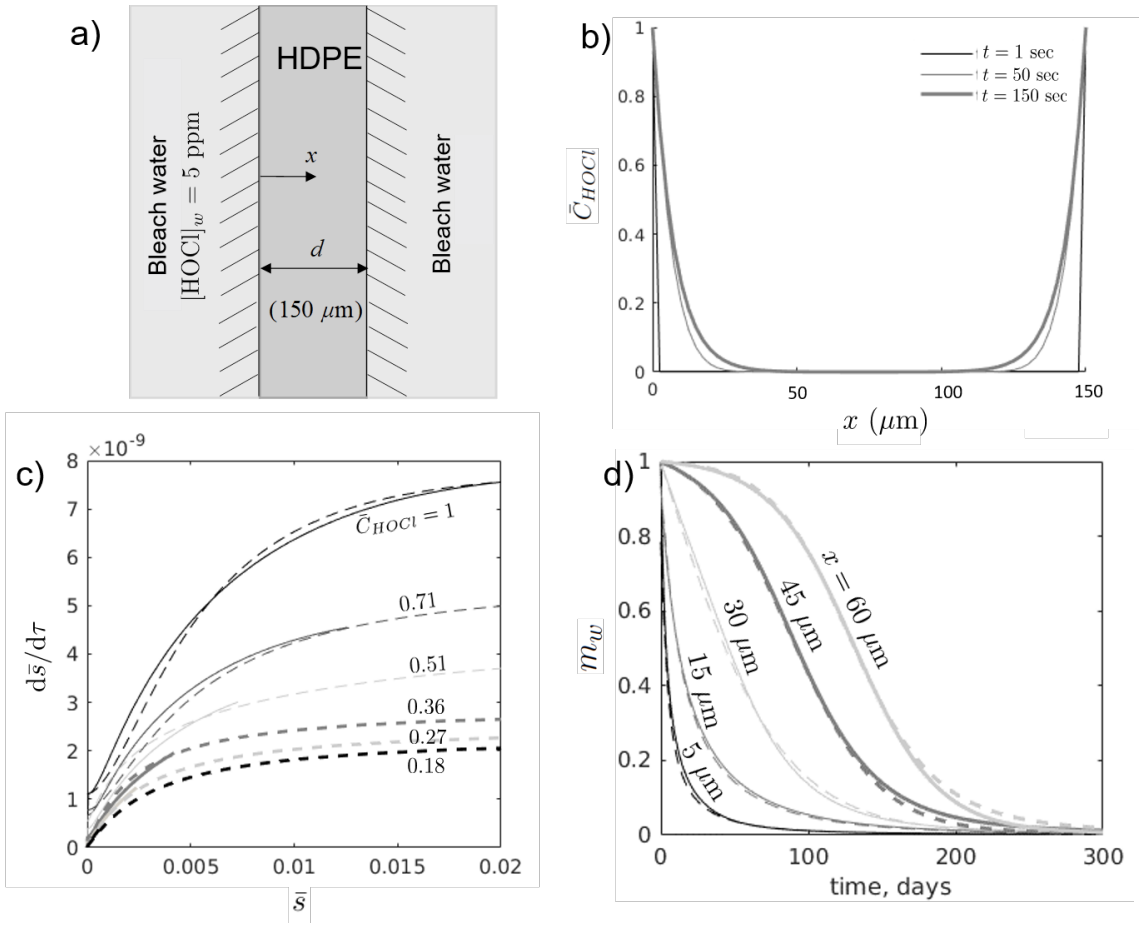

Figure 4.1: Simulation of 1D diffusion-reaction in HDPE exposed to bleached water: a) problem set-up, b) Profile of [HOCl] at different times, c) simulated kinetics of chain scission at different locations (solid line: simulation result; dashed line: optimum fits), and d) Time evolution of the relative molecular weight at different locations predicted by the present model (solid line) and the full model (dashed line).

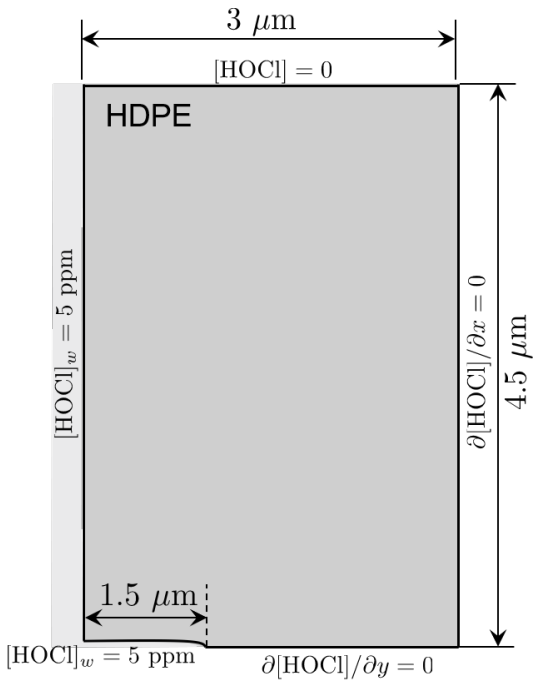

Figure 4.2: DEN specimen in bleach water

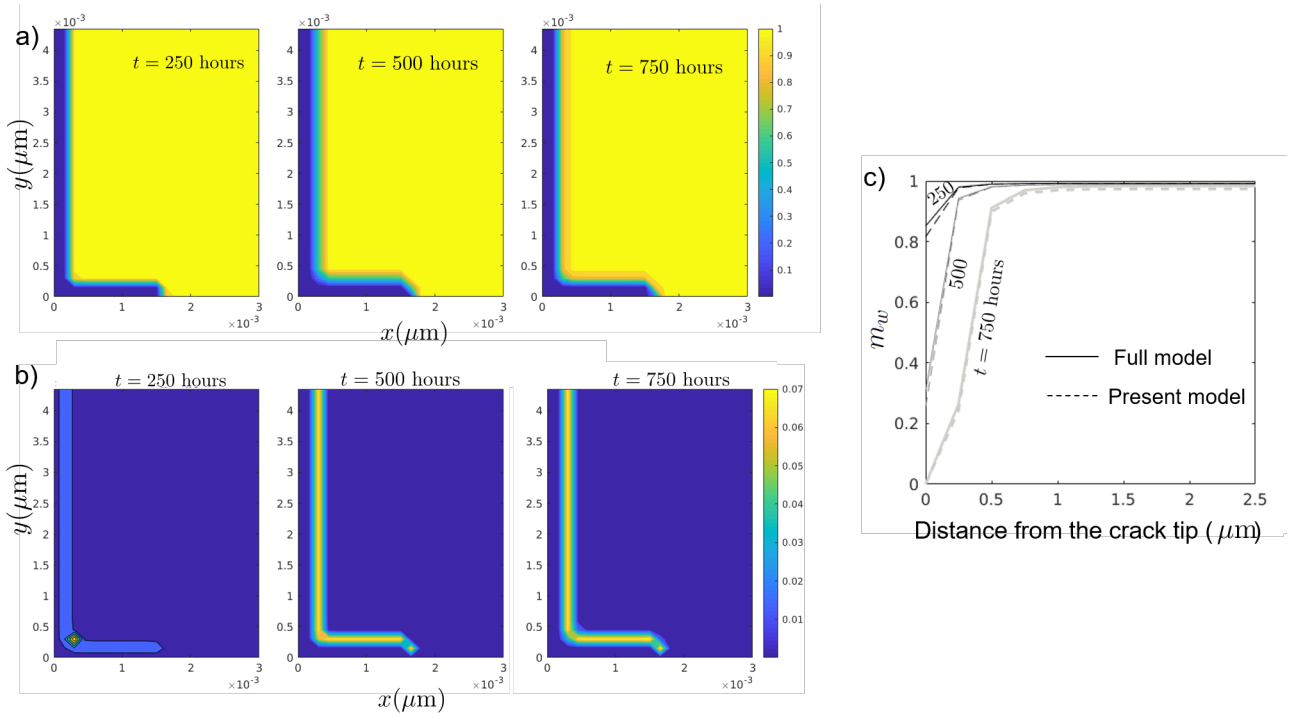

Figure 4.3: Results of 2D diffusion-reaction simulation: a) time evolution of molecular weight, b) relative error in predicted molecular weight, and c) comparison of the relative molecular weights along the crack ligament predicted by the present and full models

Chapter 5

Numerical implementation and case study

The proposed chemo-mechanical model is implemented in finite element software ABAQUS, and the numerical model is used to investigate SCC in HDPE specimens exposed to bleach solution. Section 5.1 describes the numerical implementation of the chemo-mechanical model in ABAQUS, section 5.2 describes the problem setup of the case study on SCC of HDPE specimens, and section 5.3 discusses the key results and observations from this case study.

5.1 Numerical Implementation

The present model is implemented in a commercial FE software ABAQUS. Since the diffusion-reaction equation of HOCl (Eq. 4.4) is mathematically equivalent to the heat transfer equation, the present chemomechanical analysis can be treated as a coupled thermomechanical analysis in ABAQUS. In the implementation, we treat [HOCl] as

temperature, D_{HOCl} as thermal diffusivity, k_{HOCl} as the rate of heat dissipation in a heat sink. Eq. 4.4 is solved through the user-subroutine HETVAL. The material constitutive model and reduced order kinetic model for chain scission (Eq. 4.3) are implemented through the user-subroutine UMAT.

In each iteration, new stresses and state variables are calculated from the current values of material properties. Given the updated stresses and state variables, element failure is evaluated first. The material element fails when either of the following scenarios occurs: 1) the effective void ratio in crystalline or amorphous phase reaches one, or 2) craze breakdown as the craze strain reaches its critical value ϵ_f. Once the element meets the failure criterion, it is removed from the analysis. Element removal is achieved by reducing the stress to zero gradually over several steps to avoid numerical instabilities. If the element does not fail, the concentration of HOCl calculated from HETVAL is used to calculate the chain scission, and the new molecular weight in UMAT. The new set of constitutive parameters are then determined for the next iteration. Fig. 5.1 shows the flowchart of the numerical implementation scheme.

The key feature of SCC is stable crack propagation, and the progression of bleach solution into the crack tip region. Previous studies suggested that, for the analysis of SCC, the crack can be assumed to be fully wet [107]. Therefore, in addition to the coupling between the corrosion chemistry and constitutive model, the boundary condition of the diffusion-reaction equation (Eq. 4.4) is also updated once the crack propagates. In the present implementation, once the element at the crack tip experiences failure and is deleted from the analysis, the analysis is paused, the boundary condition of Eq. 4.4 is updated, and the analysis is restarted with the stress and strain fields and [HOCl] distribution calculated at the moment of element deletion.

5.2 Problem setup for SCC case study

A double edge notched (DEN) specimen under uniaxial tension σ_0 is simulated (Fig. 5.2). The specimen is 2 mm thick and has in-plane dimensions $h = 50$ mm, $w = 30$ mm, and the notch length $a_0 = 7$ mm. In the simulation, the specimen is subject to constant loading. Five loading levels, $\sigma_0 = 1.6$, 3.2, 4.8, 6.4, and 8 MPa (corresponding to initial nominal stress on the ligament of 3, 6, 9, 12, and 15 MPa), are applied to investigate the stress-life curve of the specimen.

In the simulation, we consider the bleach water has a concentration of 5 ppm (6.7×10^{-8} mol/L) [HOCl] at $T = 60°$C such that (following [26]): $D_{HOCl} = 10^{-10}$ m^2s^{-1}, $k_{HOCl} = 1.8$ s^{-1}, $\kappa = 5.1 \times 10^{-3}$, and $U_s = 6.243 \times 10^{-20}$J. Static fatigue behavior in a non-corrosive environment is also simulated for a baseline comparison.

The bleach water is modeled by imposing constant $[\text{HOCl}]_s$ along the two vertical edges of the specimen as well as at the crack surface based on Eq. 4.5. The top and bottom loading surfaces are unexposed to the bleach water (Fig. 5.2). Due to its relatively low diffusivity, HOCl will diffuse into a very thin layer in the thickness direction during the entire lifetime of the specimen. As compared to the diffusion of HOCl at the crack surface, the diffusion in the transverse (thickness) direction has a minimal effect on the SCC behavior. Therefore, in the present analysis the in-plane surface of the specimen is assumed to be free from the bleach water.

Due to the symmetry of specimen geometry, a quarter of the specimen is modeled. The specimen is discretized using 3D elements and the mesh is refined near the crack tip. During the corrosion process, the decrease in molecular weight promotes craze damage, which features a damage localization mechanism. Based on the crack band model, we set the mesh depth according to the physical width of the localized crazing zone, which is approximately 0.7 mm [108].

The simulation is performed using an implicit analysis scheme in ABAQUS. The analysis is terminated when the solution does not converge with an extremely small attempted time increment ($\sim 10^{-40}$ s). The divergence of solution indicates that no equilibrium state can be found, and therefore it physically represents that the specimen is not able to sustain the applied constant load signifying ultimate failure.

The constitutive model parameters calibrated using the uniaxial tensile tests and the evolution of crystallinity presented in Chapter 3, and the reduced order corrosion model parameters obtained in Chapter 4 are used in this study.

5.3 Results and Discussion

5.3.1 Time-dependent deformation behavior and stress-life curve

Fig. 5.3 presents the simulated time evolution of average displacement of the top surface of the specimen under two different stress levels ($\sigma_0 = 8$ and 1.6 MPa) and different environments (0 and 5 ppm). For the case of high sustained loading $\sigma_0 = 8$ MPa, the corrosion almost has no effect on the displacement evolution, since under high stress, the lifetime of the specimen is so short that there is not sufficient time for chemical corrosion to occur. From Fig. 5.3a, the time evolution of the displacement can be divided into three regimes. In the first regime (the primary creep stage), the displacement grows rapidly with time due to the short-time response to the applied load. In the second regime (secondary creep), the displacement increases slowly over a substantial period of time due to viscoplastic behavior and void growth. In the last regime (tertiary stage), the void growth accelerates and consequently the displacement increases rapidly until the ultimate failure.

For the case of low applied stress ($\sigma_0 = 1.6$ MPa), the corrosive environment has

a pronounced effect on the deformation behavior (Fig. 5.3b). When exposed to 5 ppm bleach solution, the specimen fails in a much shorter duration compared to unexposed specimens. The displacement evolution of the unexposed specimen exhibits a similar behavior as the specimen under high stress ($\sigma_0 = 8$ MPa) except that the primary creep stage cannot be easily discerned. This is because the applied stress is low so that the initial elastic displacement in response to the stress is only a small fraction of the ultimate displacement at failure. During the entire loading duration, the deformation of specimen is primarily governed by the secondary creep. By contrast, the specimen exposed to 5 ppm bleach solution does not exhibit significant secondary creep. Instead, the displacement increases rapidly all the way to failure. This is because corrosion significantly degrades the material properties, and accelerates void growth. Based on the present model, degradation of material properties promotes the early onset of craze damage, which leads to rapid void growth and fast failure.

By considering different applied loads, the present simulation yields the relationship between applied load and lifetime, referred to as the stress-life curve, plotted in log-log scale (Fig. 5.4). The stress-life curve is often used to predict the structural lifetime for a given applied loading, a key consideration for the design of HDPE members. For unexposed specimens, the stress-life curve consists of two regimes, each exhibits an inverse power-law relation with different exponents. In the high stress regime (zone 1), the slope of the stress-life curve is small, and the lifetime is highly sensitive to the applied load: a reduction of 40% in applied load leads to an almost three-orders of magnitude increase in lifetime. In the lower stress regime (zone 2), the stress-life curve exhibits a steeper slope indicating weaker dependence of lifetime on the applied stress.

The stress-life curve of specimens exposed to bleach solution exhibits a complicated behavior. As shown in Fig. 5.4, the stress-life curve of exposed specimens shows the same zone I behavior as the unexposed specimen. This indicates that, in the high stress regime, corrosion does not affect the failure behavior due to the relatively short

lifetime. When the applied stress decreases, the stress-life curve of the exposed specimen approaches the zone 2 behavior of the unexposed specimen. However, as the stress further decreases, the stress-life curve of the exposed specimen exhibits a much steeper slope, which indicates that the lifetime becomes almost insensitive to the applied load. This regime is referred to as zone 3.

The aforementioned three zones of the stress-life curve have been experimentally observed for HDPE specimens [109, 4, 10, 34, 2]. These studies documented a change in failure mode in these three zones. In zone 1, the material fails in a ductile mode, i.e. the entire ligament yields before crack growth. In zone 2, the material fails when the crack grows with a small yielding zone at the crack tip and the far-field material is undamaged. In zone 3, the specimen fails when the crack propagates without material yielding. Therefore, it is expected that zone 3 is dominated by corrosion-induced failure, which explains the insensitivity of lifetime on the applied load.

5.3.2 Load and environmental effects on failure mechanism

The simulated stress-life curves indicate that both the applied load and the external corrosive environment have a significant effect on the failure mechanisms. In this section, we analyze the predominant failure mechanism of the different regimes of the stress-life curve by probing the stress distribution and damage status in the specimen. In all simulation cases, the failure of specimen is observed to be caused by the breakdown of its amorphous phase.

Fig. 5.5 shows the stress and damage distributions for the unexposed specimen subjected to $\sigma_0 = 8$ MPa. This represents a typical behavior of zone 1 of the stress-life curve. Fig. 5.5a shows the profiles of the effective void ratio f_a^* of the amorphous phase along the ligament at different times. During the early stage of loading, the material near the crack-tip region undergoes much more signifi

cant void growth than the remainder of the ligament. As loading continues, the effective void ratio f_a^* along the entire ligament increases from the void growth due to the yielding of the material, without craze damage. At ultimate failure, the minimum value of f_a^* along the ligament is approximately 0.36. This results in large deformation, usually referred to as ballooning, and indicates a ductile failure phenomenon. Fig. 5.5b shows the effective void ratio f_a^* in the entire specimen at ultimate failure, showing yielding of the entire ligament.

The foregoing analysis is further supported by the simulated stress profile at the ligament, shown in Fig. 5.5c. The ligament first exhibits a stress concentration at the crack tip, leading to more significant void growth at the crack tip. As the effective void ratio f_a^* at the tip region reaches its critical value, the material loses load resistance and the stress drops to zero. The remainder of the ligament experiences a mild increase in stress over the entire loading period. At ultimate failure, the stress distribution in the ligament is uniform with some softening behavior at the crack tip region. Such a stress profile represents a typical ductile failure mechanism.

To investigate the failure mechanism for zone 2, we study the distributions of the stress and effective void ratio f_a^* for an unexposed specimen subjected to $\sigma_0 = 1.6$ MPa, shown in Fig. 5.6. During the initial load stage, the behavior of zone 2 is similar to that of zone 1. The crack tip region experiences significant void growth and stress concentration. However, unlike zone 1, such a localized void growth pattern persists for the entire duration of loading (Fig. 5.6a). Fig. 5.6b shows that the effective void ratio f_a^* is localized in a small region at the crack tip. Due to this localized void growth, a significant portion of the ligament near the crack tip exhibits a softening behavior and the stress gradually decreases till the far end of the ligament (Fig. 5.6c).

A comparison of Figs. 5.5c and 5.6c reveals that the length of the traction free crack at ultimate failure is longer under a lower applied stress. Consequently, the

stress at the crack tip is higher, which leads to craze damage. Fig. 5.6d presents the crazing strain profile along the ligament at different times. The material near the crack tip undergoes craze damage, but the craze strain does not reach the critical failure strain. The material still fails by void growth governed by crazing flow. This results in a different stress-life relation as compared to zone 1, where a more homogeneous void growth occurs due to viscoplastic deformation.

Zone 3 occurs when the specimen is exposed to a corrosive environment and subjected to a low stress. In the present simulation, the exposed specimen loaded at $\sigma_0 = 1.6$ MPa corresponds to such a case. As shown in Figs. 5.7a and b, the region of void growth is highly localized at the crack tip region. Compared to the unexposed specimen (Figs. 5.7a and b), the localization region of void growth in the exposed specimen is smaller. This indicates that corrosion causes more localized damage due to the degradation of material properties. Fig. 5.7c shows that, during the early stage of loading, the molecular weight of the near-tip region drops by more than 50%. At the final failure point, the molecular weight at the crack tip drops by 20%, which is considerably less than that at the early stage. This is because crack propagation leads to higher stress at the crack tip, and consequently less time for crack propagation resulting in material failure at less degraded state.

Fig. 5.7d presents the stress profile along the ligament. The stress profile is qualitatively similar to that shown in Fig. 5.6c except that, in the exposed specimen, the crack propagates further along the ligament before the specimen fails. Fig. 5.7e shows the crazing strain profile along the ligament at ultimate failure. The material at the crack tip experiences craze breakdown. Based on the foregoing analysis of the unexposed specimen, it is clear that the occurrence of craze breakdown is due to the degradation of material properties, e.g. significant decrease in craze flow resistance and critical breakdown strain. This indicates that the specimen lifetime is governed by the diffusion-reaction timescale of HOCl. Therefore, zone 3 features a steep stress-life curve

indicating that the applied load has minimal effect on structural lifetime.

It is interesting to investigate the behavior of the exposed specimen under $\sigma_0 = 3.2$ MPa. Based on the stress-life curve (Fig. 5.4), it is expected that the behavior of the specimen lies in the transition region from zone 2 to zone 3. Fig. 5.8 shows that the distributions of the effective void growth f_a^* and stress in this specimen are qualitatively similar to those plotted in Figs. 5.6 a-c. Fig. 5.8d shows the distribution of the normalized craze strain. The initial stage of crack propagation is governed by craze breakdown at the crack tip, which is a feature of zone 3 behavior. This is correlated to the simulated distribution of molecular weight (Fig. 5.8e), which shows a considerable decrease in molecular weight at the crack tip during the initial loading stage. As the loading continues, the decrease in molecular weight becomes milder. Consequently, the crack propagates due to void growth driven by craze flow, a typical mechanism of zone 2 behavior. Both the craze breakdown and void growth mechanisms govern crack propagation for different portions of the entire specimen lifetime.

The simulated stress-lifetime curves indicate that the specimen exposed to 5 ppm bleach solution exhibits a pure zone 2 behavior over a very narrow range of applied stress. This is because the timescale of corrosion overlaps that of zone 2 behavior. It is expected that, when exposed to a bleach solution with lower concentration of HOCl, the specimen would show a clear zone 2 behavior over a larger range of stress, and zone 3 failure would be suppressed.

5.3.3 Fracture kinetics

In addition to the stress-life curve, the other important measure of the static fatigue behavior is the fracture kinetics curve (i.e. the relationship between the crack growth velocity $\mathrm{d}a/\mathrm{d}t$ and stress intensity factor K_I). In this analysis, we calculate the crack growth rate based on the simulated propagation of the traction free crack. The stress

intensity factor K_I represents merely a loading parameter of the crack-tip, where $K_I = \sigma_0\sqrt{w}k_I(a/w)$. The dimensionless function $k_I(a/w)$ depends on the specimen geometry only. Here we evaluate $k_I(a/w)$ by performing the J-integral on an elastic specimen of different crack lengths under a unit far-field stress.

Fig. 5.9 shows the fracture kinetics curves, plotted in log-log scale, of the specimen under three different environments: unexposed, 3 ppm bleach solution, and 5 ppm bleach solution. It should be emphasized that the simulated fracture kinetics curve represents a basic characteristic of stress corrosion cracking of HDPE. The curve only depends on the concentration of the bleach solution, but not on the level of sustained loading used in the simulations. The unexposed specimen exhibits a power-law relationship of the crack growth rate, i.e. $\dot{a} \propto K_I^p$ (where $\dot{a} = \mathrm{d}a/\mathrm{d}t$). Such a power law has been observed in HDPE [6, 110, 35, 34] as well as in other engineering materials, including ceramics and rock [111, 112, 113, 104]. The present analysis predicts that exponent $p = 4.9$, which is consistent with the range of the exponents experimentally measured in previous studies [6, 110, 35, 34].

When the specimen is exposed to the bleach solution, the fracture kinetics curve changes its shape. As shown in Fig. 5.9, at low values of K_I, the crack growth rate is independent of the stress intensity factor. This implies that crack propagation is driven by corrosion, and the crack growth velocity is governed by the rate of chemical diffusion and reaction. In the regime of high K_I, the crack growth velocity is strongly influenced by K_I, and the fracture kinetics relationship follows exactly that of the unexposed condition. This indicates that the fracture kinetics is not influenced by corrosion. As the concentration of the bleach solution increases, this transition occurs at a higher stress intensity factor. It is interesting to note that this behavior has also been observed in corrosion fatigue experiments on glass [43].

The foregoing discussion indicates that the fracture kinetics of HDPE under

static corrosion fatigue loading can be described by

$$\dot{a} = \max(\dot{a}_c, AK_I^p) \tag{5.1}$$

where $\dot{a}_c$ = crack growth rate purely due to chemical corrosion, and A, p = constants. However, direct use of Eq. 5.1 for predicting the structural lifetime is not straightforward because one needs to know the final crack length a_f at ultimate failure. Figs 5.5 - 5.7 show that a_f varies significantly with the applied loading and the concentration of the bleach solution. Nevertheless, Eq. 5.1 can be conveniently used for predicting the nominal service lifetime of the specimen, which corresponds to a particular extent of crack propagation.

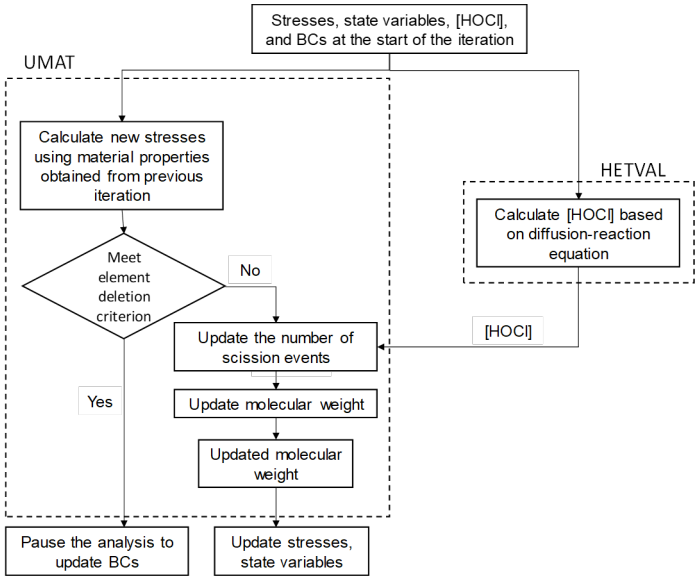

Figure 5.1: Flowchart of numerical implementation of the present chemo-mechanical model.

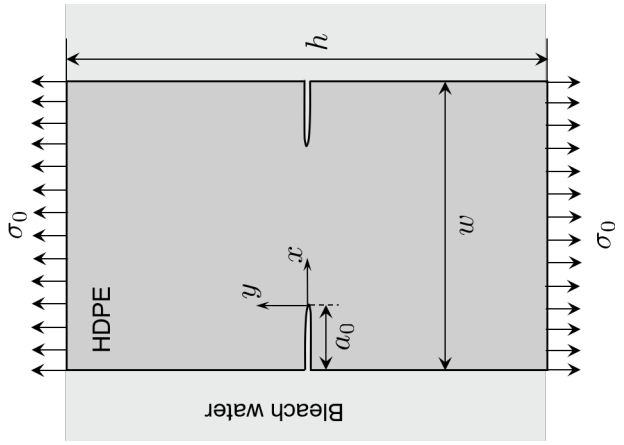

Figure 5.2: DEN specimen in bleach water

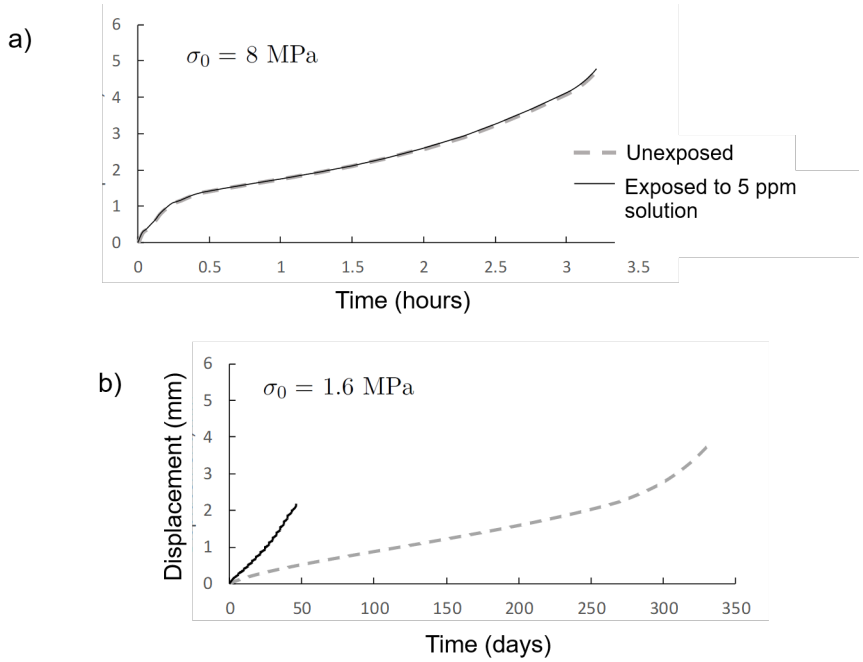

Figure 5.3: Time evolution of cross-head displacement: a) without exposure to bleach solution, and b) exposed to bleach solution (5 ppm).

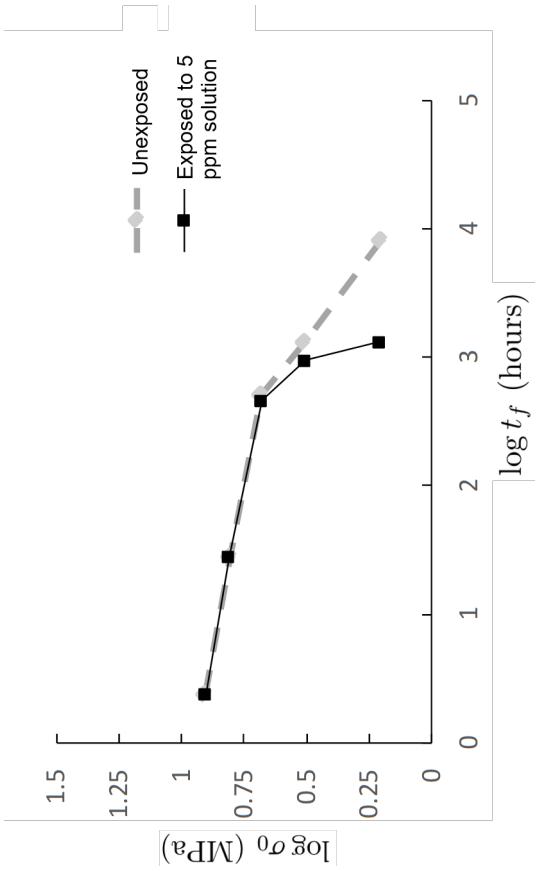

Figure 5.4: Simulated stress–life curves.

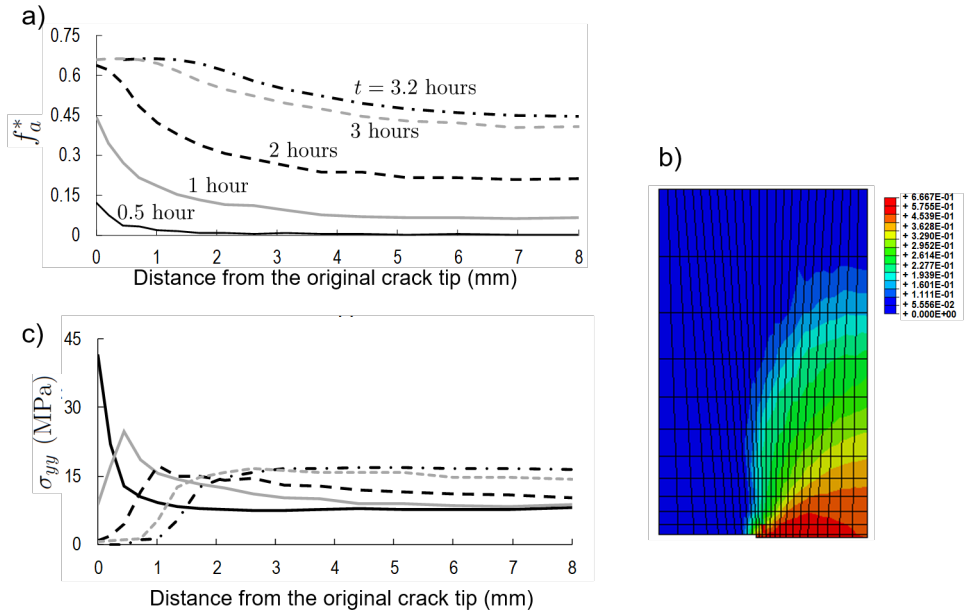

Figure 5.5: Simulated behavior of unexposed specimen subjected to $\sigma_0 = 8$ MPa: a) time evolution of the distribution of effective void ratio f_a^* of the amorphous phase along the ligament, b) distribution of f_a^* in the specimen at ultimate failure, and c) time evolution of the distribution of opening stress σ_{yy} along the ligament.

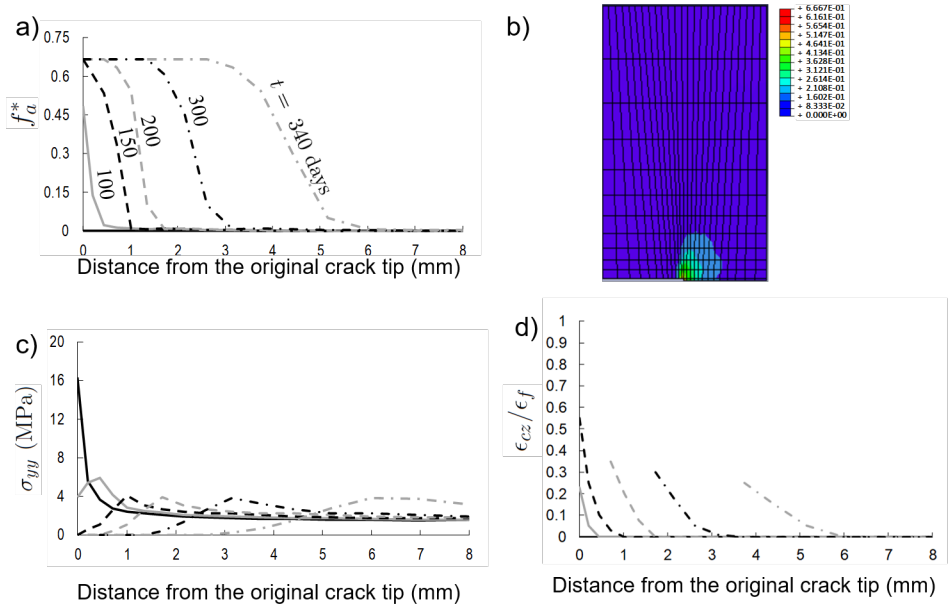

Figure 5.6: Simulated behavior of unexposed specimen subjected to $\sigma_0 = 1.6$ MPa: a) time evolution of the distribution of effective void ratio f_a^* of the amorphous phase along the ligament, b) distribution of f_a^* in the specimen at ultimate failure, c) time evolution of the distribution of opening stress σ_{yy} along the ligament, and d) time evolution of the distribution of normalized craze strain along the ligament.

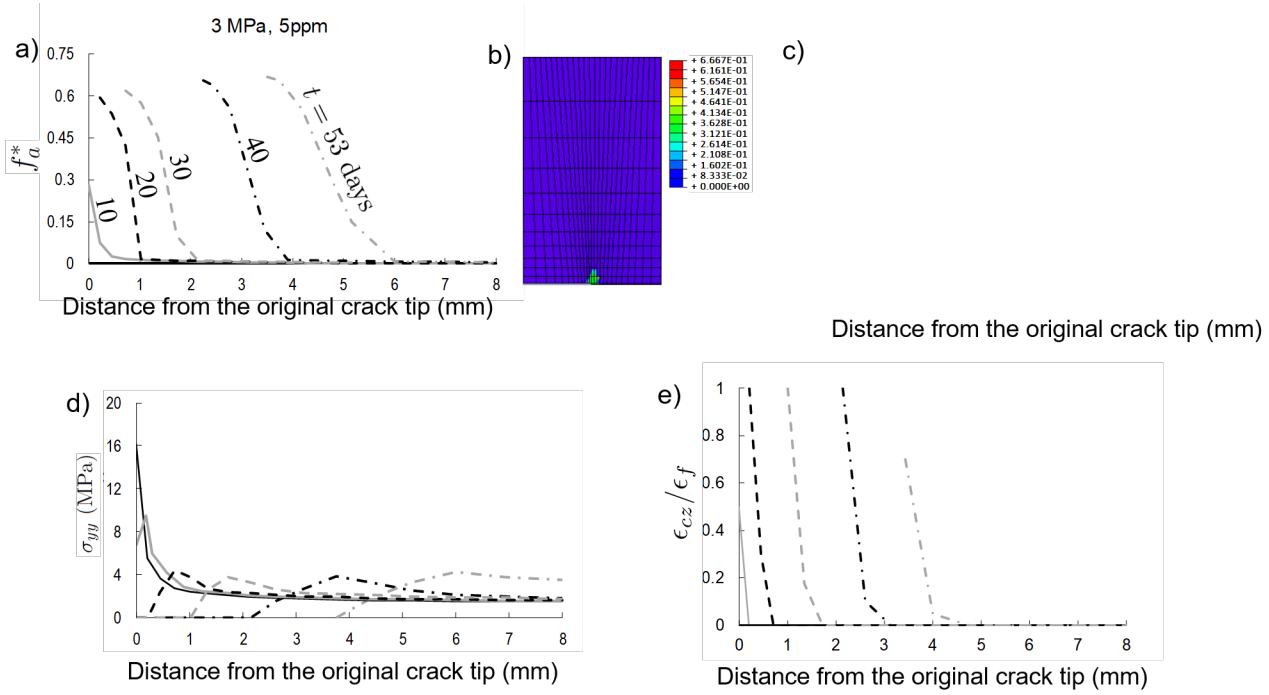

Figure 5.7: Simulated behavior of exposed specimen subjected to $\sigma_0 = 1.6$ MPa: a) time evolution of the distribution of effective void ratio f_a^* of the amorphous phase along the ligament, b) distribution of f_a^* in the specimen at ultimate failure, c) time evolution of the distribution of relative molecular weight along the ligament, d) time evolution of the distribution of opening stress σ_{yy} along the ligament, and e) time evolution of the distribution of normalized craze strain along the crack ligament.

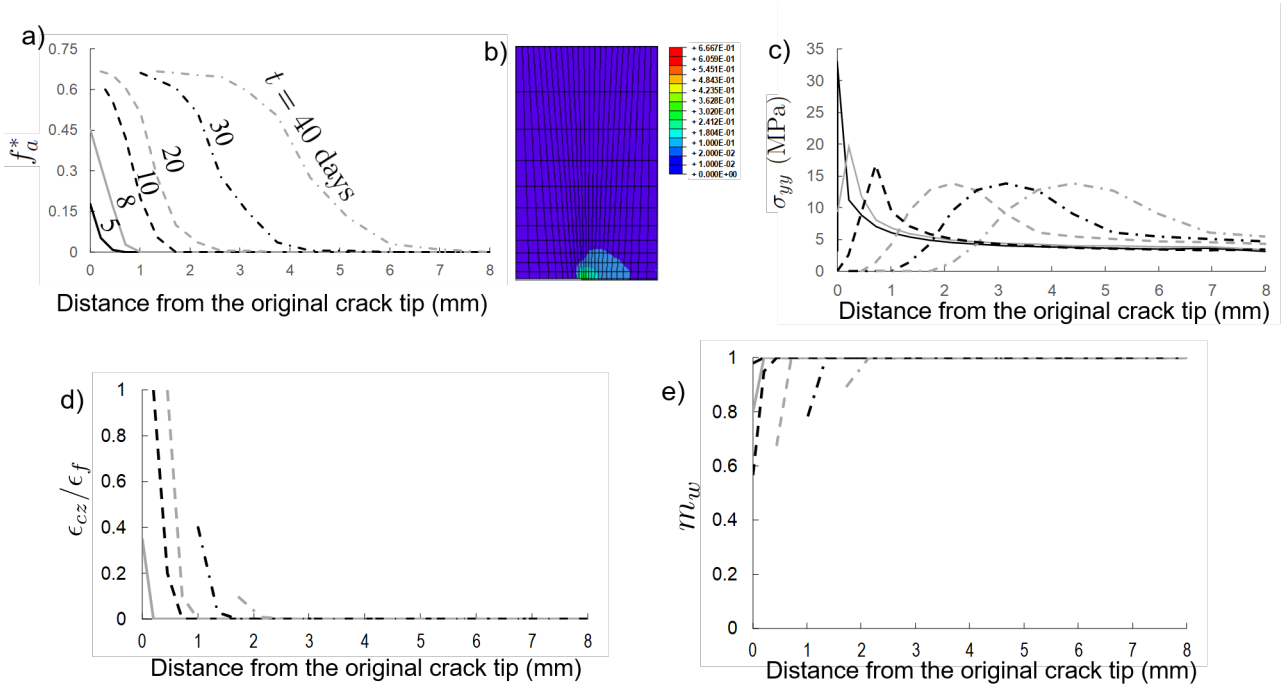

Figure 5.8: Simulated behavior of exposed specimen subjected to $\sigma_0 = 3.2$ MPa: a) time evolution of the distribution of effective void ratio f_a^* of the amorphous phase along the ligament, b) distribution of f_a^* in the specimen at ultimate failure, c) time evolution of the distribution of opening stress σ_{yy} along the ligament, d) time evolution of the distribution of normalized craze strain along the ligament, and e) time evolution of the distribution of relative molecular weight along the ligament.

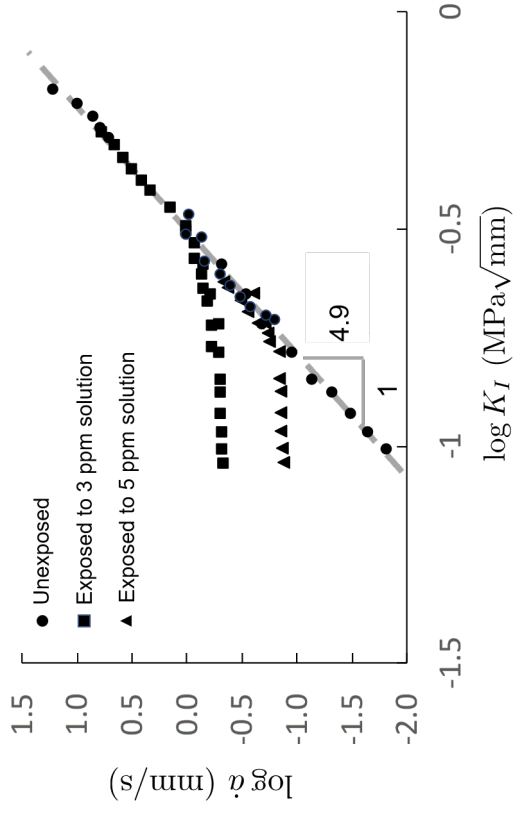

Figure 5.9: Simulated fracture kinetics curves for different environments.

Chapter 6

Conclusions

In this study, we investigate phenomenon of the stress corrosion cracking of HDPE specimens exposed to bleach solutions. We develop a chemo-mechanical model of HDPE and numerically implement it in an FE model to understand the driving mechanisms behind the accelerated crack growth in corroding polymers, which is an essential aspect of lifetime prediction of HDPE pipes. The study leads to the following conclusions:

1. We study the interaction between the cohesive crack and the capillary fluid to determine the wetting zone in the crack and the boundary conditions in a specimen under SCC. The analysis indicates that, under standard pressure values in potable water supply pipes, the crack can be considered to be fully wet. The cohesive crack-fluid study is further applied to pipe design based on fracture mechanics and shows that for a given radius-to-thickness ratio in a pipe, the critical pressure for pipe failure decreases with the pipe thickness.

2. The proposed morphology dependent constitutive model of HDPE explicitly takes into account the relevant deformation and damage mechanisms at different corrosion levels. The model considers the constitutive responses of the crystalline and

amorphous phases of HDPE separately, to capture the differences in their deterioration due to corrosion. The model incorporates the intermolecular resistance leading to void growth in both the phases along with the network resistance followed by craze damage in amorphous phase. These constitutive features allow us to capture the deviations in the long-term behavior of HDPE from the short-term observations.

3. The constitutive model is calibrated by a set of uniaxial tensile tests performed at different levels of corrosion. The calibrated model successfully predicts the stress-strain responses of HDPE with different crystallinities. Some of the amorphous phase parameters, such as the chain density and the craze parameters, are dependent on the molecular weight, which makes the overall constitutive response of the material vary with the corrosion level.

4. The constitutive model is incorporated into a finite element analysis, which is used to simulate the DEN fracture tests at different corrosion levels. The model predicts well the load-displacement response of the DEN specimens for all corrosion levels. The model shows that, as the corrosion level increases, the craze damage becomes the dominant failure mode, which explains the observed transition from a ductile to brittle response with an increasing corrosion level.

5. The corrosion level is described by the change of molecular weight and crystallinity, due to the micro-structural changes due to corrosive chemical reactions causing chain scission. A reduced order diffusion-reaction model is developed to trace only the diffusion and reaction of bleach (HOCl), whereas all secondary reactions and intermediate species are lumped into a kinetics equation of chain scission. The reduced order model yields an accurate prediction of the time evolution of the molecular weight as compared to a full diffusion-reaction model. In addition to the significant improvement in computational efficiency, another important advantage of the reduced order model is that it can be easily coupled with the constitutive

model in a single FE model in commercial software ABAQUS.

6. The chemo-mechanical model is used to predict the behavior of a DEN HDPE specimen exposed to a corrosive environment under different sustained loadings. The model successfully yields the stress-life curves, which qualitatively matches the literature data. For unexposed specimens, the model predicts a stress-life curve of two regimes, while for exposed specimens a stress-life curve of three regimes is predicted.

7. Through a detailed analysis of stress and damage distribution, the specimen in high stress regime is shown to fail in ductile manner, with a large portion of the ligament experiencing yielding at failure. In this regime, corrosive environment has a negligible effect on the specimen failure. When the applied stress is low, the unexposed specimen exhibits a localized region of void growth at the crack tip, which is primarily governed by craze damage flow. For specimens exposed to bleach solution, corrosion governs the failure mode if the applied stress is sufficiently low. In this case, failure is caused by craze breakdown in a localized region at the crack tip.

8. The model also predicts the fracture kinetics of HDPE when exposed to a range of bleach concentration. The crack growth rate law is highly dependent on the concentration of bleach solution, and it can be described by the envelop of two regimes: 1) a constant crack growth rate governed purely by corrosion, and 2) a power-law fracture kinetics model for mechanical loading. The model provides a convenient means for prediction of the service lifetime of HDPE structures.

References

[1] Y. G. Hsuan, R. M. Koerner, and A. E. Lord Jr. Stress-cracking resistance of high-density polyethylene geomembranes. *Journal of Geotechnical Engineering*, 119(11):1840–1855, 1993.

[2] J. P. Dear and N. S. Mason. Effect of chlorine on polyethylene pipes in water distribution networks. *Proceedings of the Institution of Mechanical Engineers, Part L: Journal of Materials: Design and Applications*, 220(3):97–111, 2006.

[3] N. Brown, J. Donofrio, and X. Lu. The transition between ductile and slow-crack-growth failure in polyethylene. *Polymer*, 28(8):1326–1330, 1987.

[4] A. L. Ward, X. Lu, Y. Huang, and N. Brown. The mechanism of slow crack growth in polyethylene by an environmental stress cracking agent. *Polymer*, 32(12):2172–2178, 1991.

[5] J. Fischer, R. W. Lang, P. R. Bradler, P. J. Freudenthaler, W. Buchberger, and S. C. Mantell. Global and local aging in differently stabilized polypropylenes exposed to hot chlorinatedwater with and without superimposed mechanical-environmental loads. *Polymers*, 11(7):1165, 2019.

[6] Y.-L. Huang and N. Brown. The effect of molecular weight on slow crack growth

in linear polyethylene homopolymers. *Journal of Materials Science*, 23(10):3648–3655, 1988.

[7] X. Lu and N. Brown. The ductile-brittle transition in a polyethylene copolymer. *Journal of Materials Science*, 25(1):29–34, 1990.

[8] Y.-L. Huang and N. Brown. The dependence of butyl branch density on slow crack growth in polyethylene: kinetics. *Journal of Polymer Science, Part B: Polymer Physics*, 28(11):2007–2021, 1990.

[9] R. Lang, A. Stern, and G. Doerner. Applicability and limitations of current lifetime prediction models for thermoplastics pipes under internal pressure. *Angewandte Makromolekulare Chemie*, 247:131–145, 1997.

[10] R. K. Krishnaswamy. Analysis of ductile and brittle failures from creep rupture testing of high-density polyethylene (hdpe) pipes. *Polymer*, 46(25):11664–11672, 2005.

[11] C. Devilliers, B. Fayolle, L. Laiarinandrasana, S. Oberti, and E. Gaudichet-Maurin. Kinetics of chlorine-induced polyethylene degradation in water pipes. *Polymer Degradation and Stability*, 96(7):1361–1368, 2011.

[12] S. R. Bodner and Y. Partom. A large deformation elastic-viscoplastic analysis of a thick-walled spherical shell. *Journal of Applied Mechanics*, 39(3):751–757, 1972.

[13] S. R. Bodner and Y. Partom. Constitutive equations for elastic-viscoplastic strain-hardening materials. *Journal of Applied Mechanics*, 42(2):385–389, 1975.

[14] C. Zhang and I. D. Moore. Nonlinear mechanical response of high density polyethylene. Part II: Uniaxial constitutive modeling. *Polymer Engineering and Science*, 37(2):414–420, 1997.

[15] A. D. Drozdov and Q. Yuan. The viscoelastic and viscoplastic behavior of low-density polyethylene. *International Journal of Solids and Structures*, 40(10):2321–2342, 2003.

[16] M. C. Boyce, S. Socrate, and P. G. Llana. Constitutive model for the finite deformation stress-strain behavior of poly(ethylene terephthalate) above the glass transition. *Polymer*, 41:2183–2201, 2000.

[17] M. G. A. Tijssens, E. Van der Giessen, and L. J. Sluys. Modeling of crazing using a cohesive surface methodology. *Mechanics of Materials*, 32(1):19–35, 2000.

[18] R. Estevez, M. G. A. Tijssens, and E. Van der Giessen. Modeling of the competition between shear yielding and crazing in glassy polymers. *Journal of the Mechanics and Physics of Solids*, 48(12):2585–2617, 2000.

[19] J. S. Bergström and M. C. Boyce. Constitutive modeling of the time-dependent and cyclic loading of elastomers and application to soft biological tissues. *Mechanics of Materials*, 33(9):523–530, 2001.

[20] B. P. Gearing and L. Anand. On modeling the deformation and fracture response of glassy polymers due to shear-yielding and crazing. *International Journal of Solids and Structures*, 41(11-12):3125–3150, 2004.

[21] J. V. van Dommelen, D. M. Parks, M. C. Boyce, W. A. M. Brekelmans, and F. P. T. Baaijens. Micromechanical modeling of the elasto-viscoplastic behavior of semi-crystalline polymers. *Journal of the Mechanics and Physics of Solids*, 51(3):519–541, 2002.

[22] S. Ahzi, A. Makradi, R. V. Gregory, and D. D. Edie. Modeling of deformation behavior and strain-induced crystallization in poly(ethylene terephthalate) above the glass transition temperature. *Mechanics of Materials*, 35:1139–1148, 2003.

[23] G. Ayoub, F. Zaïri, M. Naït-Abdelaziz, and J. M. Gloaguen. Modelling large deformation behaviour under loading-unloading of semicrystalline polymers: application to a high density polyethylene. *International Journal of Plasticity*, 26(3):329–347, 2010.

[24] A. Tripathi, S. C. Mantell, and J.-L. Le. A morphology based constitutive model for high density polyethylene. *Mechanics of Materials*, 137:103091, 2019.

[25] G. Papet, L. Audouin-Jirackova, and J. Verdu. Diffusion controlled radiochemical oxidation of low density polyethylene—ii. kinetic modelling. *Radiation Physics and Chemistry*, 33(4):329–335, 1989.

[26] A. Mikdam, X. Colin, G. Minard, N. Billon, and R. Maurin. A kinetic model for predicting the oxidative degradation of additive free polyethylene in bleach desinfected water. *Polymer Degradation and Stability*, 146:78–94, 2017.

[27] X. Colin, L. Audouin, J. Verdu, M. Rozental-Evesque, B. Rabaud, F. Martin, and F. Bourgine. Aging of polyethylene pipes transporting drinking water disinfected by chlorine dioxide. i. chemical aspects. *Polymer Engineering and Science*, 49(7):1429–1437, 2009.

[28] B. Fayolle, E. Richaud, X. Colin, and J. Verdu. degradation-induced embrittlement in semi-crystalline polymers having their amorphous phase in rubbery state. *Journal of Materials Science*, 43(22):6999–7012, 2008.

[29] G. A. Russell. Deuterium-isotope effects in the autoxidation of aralkyl hydrocarbons. mechanism of the interaction of peroxy radicals1. *Journal of the American Chemical Society*, 79(14):3871–3877, 1957.

[30] R. C. Golike and S. W. Lasoski Jr. Kinetics of hydrolysis of polyethylene terephthalate films. *The Journal of Physical Chemistry A*, 64(7):895–898, 1960.

[31] X. Colin, L. Audouin, and J. Verdu. Determination of thermal oxidation rate constants by an inverse method. application to polyethylene. *Polymer Degradation and Stability*, 86(2):309–321, 2004.

[32] J. Viebke and U. W. Gedde. Assessment of lifetime of hot-water polyethylene pipes based on oxidation induction time data. *Polymer Engineering and Science*, 38(8):1244–1250, 1998.

[33] G. Mittelman, J. H. Davidson, S. C. Mantell, and Y. Su. Prediction of polymer tube life for solar hot water systems: A model of antioxidant loss. *Solar Energy*, 82(5):452–461, 2008.

[34] P. Hutař, M. Ševčík, Luboš Náhlík, G. Pinter, A. Frank, and I. Mitev. A numerical methodology for lifetime estimation of HDPE pressure pipes. *Engineering Fracture Mechanics*, 78(17):3049–3058, 2011.

[35] A. Chudnovsky, Z. Zhou, H. Zhang, and K. Sehanobish. Lifetime assessment of engineering thermoplastics. *International Journal of Engineering Science*, 59:108–139, 2012.

[36] B.-H. Choi, A. Chudnovsky, and K. Sehanobish. Stress corrosion cracking in plastic pipes: Observation and modeling. *International Journal of Fracture*, 145:81–88, 2007.

[37] H. Ge, J.-L. Le, and S. C. Mantell. Numerical modeling of stress corrosion cracking of polymers. *Engineering Fracture Mechanics*, 160:199–212, 2016.

[38] W. Sun, R. Mu, X. Luo, and C. Miao. Effect of chloride salt, freeze–thaw cycling and externally applied load on the performance of the concrete. *Cement and Concrete Research*, 32(12):1859–1864, 2002.

[39] J. Hassinen, M. Lundbäck, M. Ifwarson, and U. W. Gedde. Deterioration of polyethylene pipes exposed to chlorinated water. *Polymer Degradation and Stability*, 84(2):261–267, 2004.

[40] P. K. Shukla and M. J. Rubal. Evaluating properties of chemically-aged high density polyethylene piping material used in nuclear power plants. In *NACE International Corrosion Conference Proceedings*, page 1. NACE International, 2016.

[41] R. K. Rowe and H. P. Sangam. Durability of hdpe geomembranes. *Geotextiles and Geomembranes*, 20(2):77–95, 2002.

[42] Weijin Wang, Teng Tong, Susheng Tan, and Qiang Yu. Subcritical crack growth in cementitious materials subject to chemomechanical deterioration—experimental test using specimens of negative geometry. *Journal of Applied Mechanics*, 84(4), 2017.

[43] S. M. Wiederhorn and L. H. Bolz. Stress corrosion and static fatigue of glass. *Journal of the American Ceramic Society*, 53(10):543–548, 1970.

[44] M. Ciccotti. Stress-corrosion mechanisms in silicate glasses. *Journal of Physics D: Applied Physics*, 42(21):214006, 2009.

[45] W. Yu, B. Azhdar, D. Andersson, T. Reitberger, J. Hassinen, T. Hjertberg, and U. W. Gedde. Deterioration of polyethylene pipes exposed to water containing chlorine dioxide. *Polymer Degradation and Stability*, 96(5):790–797, 2011.

[46] B.-H. Choi, Z. Zhou, A. Chudnovsky, S. S. Stivala, K. Sehanobish, and C. P. Bosnyak. Fracture initiation associated with chemical degradation: observation and modeling. *International Journal of Solids and Structures*, 42(2):681–695, 2005.

[47] H. Ge, J.-L. Le, and S. C. Mantell. Numerical modeling of stress corrosion cracking of polymers. *Engineering Fracture Mechanics*, 160:199–212, 2016.

[48] H. D. Bui. Interaction between the griffith crack and a fluid: theory of rehbinder's effects, 1996.

[49] P. A. Rebinder and V. Likhtman. Effect of surface-active media on strain and rupture in soils. In *Proceedings of 2nd International Conference on Surface Activity*, pages 563–580, 1957.

[50] A. Feraille-Fresnet, H.-D. Bui, and A. Ehrlacher. Hydrostatic interaction of a wetting fluid and a circular crack in an elastic material. *Mechanics of Materials*, 35(3-6):581–586, 2003.

[51] G. I. Barenblatt. The formation of equilibrium cracks during brittle fracture. general ideas and hypotheses. axially-symmetric cracks. *Journal of Applied Mathematics*, 23(3):622–636, 1959.

[52] G. I. Barenblatt. The mathematical theory of equilibrium cracks in brittle fracture. *Advances in Applied Mechanics*, 7(1):55–129, 1962.

[53] D. S. Dugdale. Yielding of steel sheets containing slits. *Journal of the Mechanics and Physics of Solids*, 8(2):100–104, 1960.

[54] J. R. Rice. A path independent integral and the approximate analysis of strain concentration by notches and cracks. *Journal of Applied Mechanics*, 35(2):379–386, 1968.

[55] O. Nguyen, E. A. Repetto, M. Ortiz, and R. A. Radovitzky. A cohesive model of fatigue crack growth. *International Journal of Fracture*, 110(4):351–369, 2001.

[56] K. L. Roe and T. Siegmund. An irreversible cohesive zone model for interface fatigue crack growth simulation. *Engineering Fracture Mechanics*, 70(2):209–232, 2003.

[57] X.-P. Xu and A. Needleman. Void nucleation by inclusion debonding in a crystal matrix. *Modelling and Simulation in Materials Science and Engineering*, 1(2):111, 1993.

[58] K. Park, G. H. Paulino, and J. R. Roesler. A unified potential-based cohesive model of mixed-mode fracture. *Journal of the Mechanics and Physics of Solids*, 57(6):891–908, 2009.

[59] S. Salehi and R. Nygaard. Full fluid–solid cohesive finite-element model to simulate near wellbore fractures. *Journal of Energy Resources Technology*, 137(1), 2015.

[60] K. Sato and T. Hashida. Cohesive crack analysis of toughness increase due to confining pressure. *Pure and Applied Geophysics*, 163(5-6):1059–1072, 2006.

[61] J. Réthoré, R. De Borst, and M.-A. Abellan. A two-scale model for fluid flow in an unsaturated porous medium with cohesive cracks. *Computational Mechanics*, 42(2):227–238, 2008.

[62] Z. P. Bažant and J. Planas. *Fracture and size effect in concrete and other quasibrittle materials*, volume 16. CRC press, 1997.

[63] Z. P. Bažant and G. Lewis. Scaling of structural strength. *Applied Mechanics Reviews*, 56(5):B70–B72, 2003.

[64] G. Cusatis and E. A. Schauffert. Cohesive crack analysis of size effect. *Engineering Fracture Mechanics*, 76(14):2163–2173, 2009.

[65] S. Morel, C. Lespine, J.-L. Coureau, J. Planas, and N. Dourado. Bilinear softening parameters and equivalent lefm r-curve in quasibrittle failure. *International Journal of Solids and Structures*, 47(6):837–850, 2010.

[66] J.-L. Coureau, S. Morel, and N. Dourado. Cohesive zone model and quasibrittle failure of wood: a new light on the adapted specimen geometries for fracture tests. *Engineering Fracture Mechanics*, 109:328–340, 2013.

[67] T. Young. Iii. an essay on the cohesion of fluids. *Philosophical Transactions of the Royal Society A*, 95:65–87, 1805.

[68] P. S. Laplace. Traité de mécanique celeste, vol. 4. *Supplements au Livre X*, 1805.

[69] E. Buckingham. On physically similar systems; illustrations of the use of dimensional equations. *Physical Review*, 4(4):345, 1914.

[70] E. Buckingham. Model experiments and the form of empirical equations. *Physical Review*, 2:345, 1914.

[71] G. I. Barenblatt. *Scaling*, volume 34. Cambridge University Press, 2003.

[72] H. Tada, P. Paris, and G. Irwin. The analysis of cracks handbook. *New York: ASME Press*, 2:1, 2000.

[73] O. U. Colak and N. Dusunceli. Modeling Viscoelastic and Viscoplastic Behavior of High Density Polyethylene (HDPE). *Journal of Engineering Materials and Technology*, 128(4):572–578, 05 2006.

[74] R. N. Haward and G. Thackray. The use of a mathematical model to describe isothermal stress-strain curves in glassy thermoplastics. *Proceedings of the Royal Society A: Mathematical, Physical and Engineering Sciences*, 302(1471):453–472, 1968.

[75] S. R. Bodner and Y. Partom. Constitutive equations for elastic-viscoplastic strain-hardening materials. *Journal of Applied Mechanics*, 42(2):385–389, 06 1975.

[76] E. M. Arruda and M. C. Boyce. A three-dimensional constitutive model for the large stretch behavior of rubber elastic materials. *Journal of the Mechanics and Physics of Solids*, 41(2):389–412, 1993.

[77] R. Balieu, F. Lauro, B. Bennani, R. Delille, T. Matsumoto, and E. Mottola. A fully coupled elastoviscoplastic damage model at finite strains for mineral filled semi-crystalline polymer. *International Journal of Plasticity*, 51:241–270, 2013.

[78] M. Challier, J. Besson, L. Laiarinandrasana, and R. Piques. Damage and fracture of polyvinylidene fluoride (pvdf) at 20 c: Experiments and modelling. *Engineering Fracture Mechanics*, 73(1):79–90, 2006.

[79] F. Zaïri, M. Naït-Abdelaziz, J.-M. Gloaguen, and J.-M. Lefebvre. Modelling of the elasto-viscoplastic damage behaviour of glassy polymers. *International Journal of Plasticity*, 24(6):945–965, 2008.

[80] L. Laiarinandrasana, J. Besson, M. Lafarge, and G. Hochstetter. Temperature dependent mechanical behaviour of pvdf: experiments and numerical modelling. *International Journal of Plasticity*, 25(7):1301–1324, 2009.

[81] C. Regrain, L. Laiarinandrasana, S. Toillon, and K. Saï. Multi-mechanism models for semi-crystalline polymer: Constitutive relations and finite element implementation. *International Journal of Plasticity*, 25(7):1253–1279, 2009.

[82] K. Sai, L. Laiarinandrasana, I. B. Naceur, J. Besson, M. Jeridi, and G. Cailletaud. Multi-mechanism damage-plasticity model for semi-crystalline polymer: Creep damage of notched specimen of pa6. *Materials Science and Engineering: A*, 528(3):1087–1093, 2011.

[83] V. Tvergaard and A. Needleman. Analysis of the cup-cone fracture in a round tensile bar. *Acta Metallurgica*, 32(1):157–169, 1984.

[84] H.-H. Kausch, R. Gensler, C. Grein, C. J. G. Plummer, and P. Scaramuzzino. Crazing in semicrystalline thermoplastics. *Journal of Macromolecular Science, Part B*, 38(5-6):803–815, 1999.

[85] C. J. G. Plummer, C. L. Soles, C. Xiao, J. Wu, H.-H. Kausch, and A. F. Yee. Effect of limiting chain mobility on the yielding and crazing behavior of bisphenol-a polycarbonate derivatives. *Macromolecules*, 28(21):7157–7164, 1995.

[86] C. J. G. Plummer, N. Cudré-Mauroux, and H.-H. Kausch. Deformation and entanglement in semicrystalline polymers. *Polymer Engineering and Science*, 34(4):318–329, 1994.

[87] E. J. Kramer. Microscopic and molecular fundamentals of crazing. In *Crazing in polymers*, pages 1–56. Springer, 1983.

[88] L. L. Berger. On the mechanism of craze fibril breakdown in glassy polymers. *Macromolecules*, 23(11):2926–2934, 1990.

[89] E. J. Kramer and L. L. Berger. Fundamental processes of craze growth and fracture. In *Crazing in Polymers*, volume 2, pages 1–68. Springer, 1990.

[90] C. B. Bucknall. Role of surface chain mobility in crazing. *Polymer*, 53(21):4778 – 4786, 2012.

[91] E. H. Lee. Elastic-plastic deformation at finite strains. *Journal of Applied Mechanics*, 36(1):1–6, 1969.

[92] M. C. Boyce, G. G. Weber, and D. M. Parks. On the kinematics of finite strain plasticity. *Journal of the Mechanics and Physics of Solids*, 37(5):647–665, 1989.

[93] A. L. Gurson. Continuum theory of ductile rupture by void nucleation and growth: Part i –yield criteria and flow rules for porous ductile media. *Journal of Engineering Materials and Technology*, 99, 1977.

[94] A. Oral, G. Anlas, and J. Lambros. Determination of gurson–tvergaard–needleman model parameters for failure of a polymeric material. *International Journal of Damage Mechanics*, 21(1):3–25, 2012.

[95] F. Zaïri, M. Naït-Abdelaziz, J. M. Gloaguen, and J. M. Lefebvre. A physically-based constitutive model for anisotropic damage in rubber-toughened glassy polymers during finite deformation. *International Journal of Plasticity*, 27(1):25–51, 2011.

[96] A. S. Argon. Physical basis of distortional and dilational plastic flow in glassy polymers. *Journal of Macromolecular Science, Part B*, 8(3-4):573–596, 1973.

[97] E. Cosgriff, S. C. Mantell, and M. Bhattacharya. Method for degrading polyethylene sheet samples in an oxidative environment. In *75th Annual Technical Conference and Exhibition of the Society of Plastics Engineers, SPE ANTEC Anaheim 2017*, pages 1228–1233. Society of Plastics Engineers, 2017.

[98] K. Majewski. Morphology and mechanical properties of high density polyethylene exposed to chlorinated water. 2018.

[99] ASTM D1708. Standard test method for tensile properties of plastics by use of microtensile specimens. *American Society for Testing and Materials*, 2011.

[100] J. Blaber, B. Adair, and A. Antoniou. Ncorr: open-source 2d digital image correlation matlab software. *Experimental Mechanics*, 55(6):1105–1122, 2015.

[101] ASTM D5397. Standard test method for evaluation of stress crack resistance of polyolefin geomembranes using notched constant tensile load test, 2012.

[102] Z. P. Bažant and B. H. Oh. Crack band theory for fracture of concrete. *Materials and Structures*, 16(3):155–177, 1983.

[103] Z. P. Bažant and M. Jirásek. Nonlocal integral formulations of plasticity and damage: survey of progress. *Journal of Engineering Mechanics*, 128(11):1119–1149, 2002.

[104] Z. P. Bažant and J.-L. Le. *Probabilistic Mechanics of Quasibrittle Structures: Strength, Lifetime, and Size Effect*. Cambridge University Press, Cambridge, U.K., 2017.

[105] H. H. Kausch-Blecken von Schmeling and J. G. Williams. *Polymer fracture*. Wiley Online Library, 2002.

[106] K. Majewski, S. C. Mantell, and M. Bhattacharya. Relationship between morphological changes and mechanical properties in hdpe films exposed to a chlorinated environment. *Polymer Degradation and Stability*, 171:109027, 2020.

[107] A. Tripathi, S. C. Mantell, and J.-L. Le. Modeling of cohesive fracture interacting with a stationary capillary fluid. *Engineering Fracture Mechanics*, 182:19–31, 2017.

[108] A. Oral, G. Anlas, and J. Lambros. Determination of Gurson-Tvergaard-Needleman model parameters for failure of a polymeric material. *International Journal of Damage Mechanics*, 21(1):3–25, 2012.

[109] N. Brown. Intrinsic lifetime of polyethylene pipelines. *Polymer Engineering and Science*, 47(4):477–480, 2007.

[110] A. Frank, W. Freimann, G. Pinter, and R. W. Lang. A fracture mechanics concept for the accelerated characterization of creep crack growth in pe-hd pipe grades. *Engineering Fracture Mechanics*, 76(18):2780–2787, 2009.

[111] A. G. Evans. A method for evaluating the time-dependent failure characteristics of brittle materials - and its application to polycrystalline alumina. *Journal of Materials Science*, 7:1173–1146, 1972.

[112] B. K. Atkinson. Subcritical crack growth in geological materials. *Journal of Geophysical Research*, 89(B6):4077–4114, 1984.

[113] D. Munz and T. Fett. *Ceramics: Mechanical Properties, Failure Behavior, Materials Selection*. Springer-Verlag, Berlin, 1999.

Appendix A

Nomenclature

Table A.1: Nomenclature

Symbol	Meaning
CZM	Cohesive Zone Model
DEN	Double Ede Notched
FE	Finite Element
FPZ	Fracture process zone
HDPE	High Density Polyethylene
HOCl	Hypochlorous acid
LEFM	Linear Elastic Fracture Mechanics
SCC	Stress Corrosion Cracking
Chapter 2	
f_t	Material tensile strength
σ	Stress
w_u	Ultimate opening at which the cohesive stress reduces to zero

Continued on next page

Table A.1 – continued from previous page

Symbol	Meaning
$g(x)$	Dimensionless function to describe the shape of the cohesive law
G_f	Fracture energy of the material
σ_∞	Far field loading
p	Fluid pressure
γ	Surface tension
R	Radius of curvature
θ	Contact angle
x	Distance from the traction free crack tip
$w(c)$	Crack opening displacement at $x = c$
$w'(x)$	Spatial gradient of the crack opening displacement
$C_{\sigma x}(a_c)$	Compliance function describing the crack opening displacement at x for a unit far-field external stress
$C_{x'x}$	Compliance function describing the crack opening displacement at location x when a pair of unit forces is applied at location x' of the crack surface
a_0	Length of the original traction-free crack
a_c	Total length of the cohesive crack including the traction-free crack
k_σ	Dimensionless stress intensity factor for the far-field external stress
$k_p(\xi, \alpha_c)$	Dimensionless stress intensity factor for the force applied at the crack surface
ξ	Dimensionless relative coordinates
E	Young's Modulus
E'	Plain strain Young's modulus
ν	Poisson ratio

Continued on next page

Table A.1 – continued from previous page

Symbol	Meaning
π_i	Dimensionless parameters
Δa_e	Equivalent crack extension
κ	Constant relation equivalent crack extension to FPZ
$K_1(a_0)$	Stress intensity factor for the original traction free crack
η	Brittleness number
η_{th}	A threshold value of η below which LEFM is valid
ϵ	Relative difference between the equivalent LEFM and LEFM solutions
β	A dimensionless brittleness parameter
α_e	Dimensionless equivalent crack length
φ	Factor of safety used for pipe design
Chapter 3	
$\mathbf{T}$	the Cauchy stress in the polymer
$\mathbf{T}_i$	the Cauchy stress in the amorphous and crystalline phases $i = c, a$
$\mathbf{F}_i$	Deformation gradient
$\mathbf{F}_i^e$	Elastic deformation gradient
$\mathbf{F}_i^p$	Plastic deformation gradient
$\mathbf{L}_i$	Velocity gradient
$\mathbf{L}_i^e$	Elastic velocity gradient
$\mathbf{L}_i^p$	Plastic velocity gradient
$\mathbf{D}_i^p$	Rate of deformation tensor
$\mathbf{W}_i^p$	Spin tensor
$\mathbf{C}_i^e$	the fourth order stiffness tensor with components
λ_i, μ_c	Lames constants

Continued on next page

Table A.1 – continued from previous page

Symbol	Meaning
ν_i	the Poisson's ratio
$\mathbf{V}_i^e$	left elastic stretch tensor
J_i	volume change
f_c	the void volume fraction
$\bar{\sigma}_m$	Macroscopic Cauchy stress used in GTN model
$\mathbf{T}_i'$	Deviatoric Cauchy stress
σ_{fi}	Tensile flow stress
f_i^*	Effective void ratio
q_1, q_2	GTN model constants
$\Phi_i 0$	Yield criterion
f_{iu}	Theoretical ultimate value of f_c^* at final failure
f_{if}	Actual void volume fraction at the failure
f_{ic}	Critical void volume fraction at which the accelerated void growth occurs due to void coalescence
τ_i	Viscoplastic shear strain rate
γ_{i0}	Constant
k_b	Boltzmann constant
T	absolute temperature
ΔG_i	Energy barrier governing the flow
α_i	Pressure coefficient
$\mathbf{T}_{aN}$	Network stress in the amorphous phase
$\mathbf{F}_{aN}$	Network deformation gradient
λ_N	Effective elastic network stretch
n	Chain density

Continued on next page

Table A.1 – continued from previous page

Symbol	Meaning
N	Number of chain units between the entanglements
$\mathcal{L}^{-1}(x)$	Inverse Langevin function
$\mathbf{I}$	Second-order identity tensor
$\dot{\gamma}^p_{aN}$	Relaxation rate
$\mathbf{T}'_{aN}$	Deviatoric network stress
λ_p	inelastic stretch
γ_{N0}	Temperature dependence prefactor
Q	Activation energy barrier
C	Constant
σ_A	Maximum principal stress in the amorphous phase
σ_{cr}	Threshold for crazing
$\mathbf{e}_1$	Unit vector denoting the direction of the maximum principal stress
γ_{cz0}	Craze flow constant
m_{cz}	Rate sensitivity constant
s_{cz}	Craze flow resistance
ϵ_{cz}	Inelastic strain accumulated after the onset of craze initiation
ϵ_f	Critical strain value
M_w	Molecular weight
M_{w0}	Initial molecular weight
m_w	Relative molecular weight
z	Crystallinity
z_0	Initial crystallinity
Chapter 4	
s	Chain scission density

Continued on next page

Table A.1 – continued from previous page

Symbol	Meaning
x	Cross-linking density
$\bar{s}$	Theoretical maximum possible number of scission events
M_{c0}	Molecular weight of the monomer
k_{HOCl}	Dissociation constant of HOCl
k_{HOCl}	Diffusion coefficient of HOCl in HDPE
κ, U_s	Constants governing surface concentration of HOCl
$[\text{HOCl}]_w$	HOCl concentration in the solution
$[\text{HOCl}]_s$	HOCl concentration on the HDPE surface
τ	A time scale
a, b, and c	Scission rate equation parameters dependent on [HOCl] and reaction rates
Chapter 5	
K_I	Stress intensity factor
$\dot{a}_c$	Crack growth rate